



The VLA-COSMOS 3 GHz Large Project: Evolution of Specific Star Formation Rates out to $z \sim 5$

Sarah K. Leslie^{1,2} , Eva Schinnerer¹ , Daizhong Liu¹ , Benjamin Magnelli³ , Hiddo Algera², Alexander Karim³ , Iary Davidzon^{4,5} , Ghassem Gozaliasl^{6,7}, Eric F. Jiménez-Andrade³, Philipp Lang¹ , Mark T. Sargent⁸ , Mladen Novak¹ , Brent Groves⁹ , Vernesa Smolčić¹⁰ , Giovanni Zamorani¹¹ , Mattia Vaccari^{12,13} , Andrew Battisti⁹ , Eleni Vardoulaki³, Yingjie Peng¹⁴, and Jeyhan Kartaltepe¹⁵

¹ Max-Planck-Institut für Astronomie, Königstuhl 17, D-69117, Heidelberg, Germany; leslie@mpia.de

² Leiden Observatory, Leiden University, P.O. Box 9513, NL-2300 RA Leiden, The Netherlands¹⁶

³ Argelander-Institut für Astronomie, Auf dem Hügel 71, D-53121 Bonn, Germany

⁴ Cosmic Dawn Center (DAWN), Denmark

⁵ Niels Bohr Institute, University of Copenhagen, Lyngbyvej 2, Copenhagen Ø DK-2100, Denmark

⁶ Department of Physics, University of Helsinki, P.O. Box 64, FI-00014, Helsinki, Finland

⁷ Helsinki Institute of Physics, University of Helsinki, P.O. Box 64, FI-00014, Helsinki, Finland

⁸ Astronomy Centre, Department of Physics and Astronomy, University of Sussex, Brighton BN1 9QH, UK

⁹ Research School of Astronomy and Astrophysics, Australian National University, Canberra, ACT 2611, Australia

¹⁰ Faculty of Science University of Zagreb Bijenička c. 32, 10002 Zagreb, Croatia

¹¹ INAF—Osservatorio di Astrofisica e Scienza dello Spazio di Bologna, via Gobetti 93/3, I-40129 Bologna, Italy

¹² Inter-University Institute for Data Intensive Astronomy University of the Western Cape, Robert Sobukwe Road, 7535 Bellville, Cape Town, South Africa

¹³ INAF—Istituto di Radioastronomia, via Gobetti 101, I-40129 Bologna, Italy

¹⁴ Kavli Institute for Astronomy and Astrophysics, Peking University, 5 Yiheyuan Road, Beijing 100871, People’s Republic of China

¹⁵ School of Physics and Astronomy, Rochester Institute of Technology, Rochester, NY 14623, USA

Received 2019 July 9; revised 2020 June 23; accepted 2020 June 24; published 2020 August 12

Abstract

We provide a coherent, uniform measurement of the evolution of the logarithmic star formation rate (SFR)–stellar mass (M_*) relation, called the main sequence (MS) of star-forming galaxies, for star-forming and all galaxies out to $z \sim 5$. We measure the MS using mean stacks of 3 GHz radio-continuum images to derive average SFRs for $\sim 200,000$ mass-selected galaxies at $z > 0.3$ in the COSMOS field. We describe the MS relation by adopting a new model that incorporates a linear relation at low stellar mass ($\log(M_*/M_\odot) < 10$) and a flattening at high stellar mass that becomes more prominent at low redshift ($z < 1.5$). We find that the SFR density peaks at $1.5 < z < 2$, and at each epoch there is a characteristic stellar mass ($M_* = 1\text{--}4 \times 10^{10} M_\odot$) that contributes the most to the overall SFR density. This characteristic mass increases with redshift, at least to $z \sim 2.5$. We find no significant evidence for variations in the MS relation for galaxies in different environments traced by the galaxy number density at $0.3 < z < 3$, nor for galaxies in X-ray groups at $z \sim 0.75$. We confirm that massive bulge-dominated galaxies have lower SFRs than disk-dominated galaxies at a fixed stellar mass at $z < 1.2$. As a consequence, the increase in bulge-dominated galaxies in the local star-forming population leads to a flattening of the MS at high stellar masses. This indicates that “mass quenching” is linked with changes in the morphological composition of galaxies at a fixed stellar mass.

Unified Astronomy Thesaurus concepts: Galaxy evolution (594); Galaxy quenching (2040); Galaxy bulges (578); Galaxy environments (2029); Radio continuum emission (1340); Extragalactic radio sources (508)

1. Introduction

Observations in the last century concluded that the global star formation rate (SFR) in a comoving volume, the SFR density (SFRD) of the universe, is a rapidly evolving quantity (e.g., Tinsley & Danly 1980; Gallego et al. 1995; Cowie et al. 1996, 1999; Lilly et al. 1996; Connolly et al. 1997; Madau et al. 1998; Pascarella et al. 1998; Tresse & Maddox 1998; Blain et al. 1999; Flores et al. 1999; Steidel et al. 1999). Reviewed by Madau & Dickinson (2014), the cosmic SFRD has undergone a rapid decline over the last ~ 8 billion years after having peaked at redshift ~ 2 . The SFRD at early cosmic times ($z > 4$), as inferred from ultraviolet (UV) luminosity functions, declines steeply to higher redshifts (out to $z \sim 10$; Oesch et al. 2013, 2018; Bouwens et al. 2014, 2015; Livermore et al. 2017). In the presence of interstellar dust, UV light is

heavily obscured, and attenuation corrections have to be applied. The amount of dust-obscured star formation at these redshifts is highly uncertain and could be between zero and ~ 10 times that currently observed (Casey et al. 2018). Uncertain dust correction factors required for early cosmic times highlight the critical need for dust-unbiased measurements at these high redshifts ($z > 4$, e.g., Bowler et al. 2018).

Measuring the SFRs of galaxies using the long-wavelength radio continuum can provide a dust-unbiased view of the cosmic SFR history of the universe. Radio-continuum SFRs have been successfully applied at low redshifts ($z \lesssim 0.1$; e.g., Condon et al. 2002; Hopkins et al. 2003; Tabatabaei et al. 2017) and at higher redshifts ($0 < z < 3$; e.g., Haarsma et al. 2000; Pannella et al. 2009a, 2015; Karim et al. 2011; Zwart et al. 2014; Novak et al. 2017; Upjohn et al. 2019). Radio-continuum observations of the high-redshift universe are not affected by source confusion that limits current deep, wide-area infrared (IR) data from, for example, Spitzer and Herschel, primarily due to the higher angular resolution observations that

¹⁶ Fellow of the International Max Planck Research School for Astronomy and Cosmic Physics at the University of Heidelberg.

can be achieved with radio interferometers (e.g., $\sim 1''$ at 3 GHz with the VLA compared to $> 10''$ at $> 160 \mu\text{m}$ with Herschel).

Most radio SFR calibrations rely on the tight correlation (scatter $\sim 0.2\text{--}0.3$ dex; Yun et al. 2001; Molnár et al. 2020) between galaxy IR and radio emission in the local universe. At frequencies < 20 GHz, the radio-continuum emission of star-forming galaxies is typically composed of a dominant synchrotron component ($\sim 90\%$ at $\nu = 1.4$ GHz, e.g., Condon 1992; Tabatabaei et al. 2017) from supernovae and their remnants, and a thermal flat-spectrum element from warm H II regions; these two physical processes render radio-continuum emission a robust SFR tracer on timescales of 0–100 Myr (Murphy et al. 2011; Kennicutt & Evans 2012). The radio–infrared correlation has recently been reported to evolve mildly with redshift, and thus it can be used to constrain an empirical radio–SFR calibration (e.g., Magnelli et al. 2015; Delhaize et al. 2017). A widespread concern about using the radio as a SFR tracer is the fact that an active galactic nucleus (AGN) can be hidden at all other wavelengths but contribute to, or dominate (in the case of radio AGNs), the radio-continuum emission (e.g., Wong et al. 2016).¹⁷ However, studies such as Novak et al. (2018) report that faint radio sources observed at 3 GHz are overwhelmingly star-forming sources (e.g., 90%–95% at fluxes between 0.1 and $10 \mu\text{Jy}$).

Despite our growing knowledge about the cosmic SFRD, details about the key factors driving its evolution remain unclear. In the SFR–stellar mass plane, observations indicate that galaxies reside in two populations. One population consists of star-forming galaxies whose SFR is positively correlated with stellar mass out to redshifts of at least 4 (e.g., Brinchmann et al. 2004; Daddi et al. 2007; Elbaz et al. 2007; Pannella et al. 2009a; Magdis et al. 2010; Karim et al. 2011; Rodighiero et al. 2011, 2014; Wuyts et al. 2011; Sargent et al. 2012; Whitaker et al. 2012, 2014; Speagle et al. 2014; Lee et al. 2015; Tomczak et al. 2016; Pearson et al. 2018). Since first reported, this tight relationship, referred to as the main sequence of star-forming galaxies (MS; Noeske et al. 2007), has been used widely by the astronomical community as a tool for understanding galaxy evolution, from sample selections to constraints or validation tests for simulations. The second population consists of quiescent galaxies that are not actively forming stars. Quiescent galaxies are those that fall ~ 1 dex below the MS (e.g., Renzini & Peng 2015) and typically reside at the high-mass end (i.e., they have lower specific star formation rates; $\text{sSFR} = \text{SFR}/M_*$). However, the sharp bimodality in sSFR seen in optical or UV-selected samples in the local universe disappears if far-infrared SFRs are used as revealed by Herschel Surveys (Eales et al. 2018a, 2018b), where a single galaxy sequence is found.

There is no established consensus in the literature on the proper form of the MS; whether it is linear across all redshifts (e.g., Wuyts et al. 2011; Speagle et al. 2014; Pearson et al. 2018) or has a flattening or turnover at stellar masses $\log(M_*/M_\odot) > 10.5$ (e.g., Whitaker et al. 2014; Lee et al. 2015; Schreiber et al. 2015; Tomczak et al. 2016) remains a matter of debate. This discrepancy seems to be driven by selection effects; for instance, studies sampling more active or bluer star-forming galaxies generally report a linear MS relation (e.g., Johnston et al. 2015), similar to studies that

include only the SFR and stellar mass residing in a disk component (Abramson et al. 2014) or if only disk galaxies are selected (Whitaker et al. 2015). Furthermore, the normalization of the MS relation depends on the SFR tracer and calibrations used (e.g., Speagle et al. 2014; Bisigello et al. 2018).

The position of galaxies on the SFR–stellar mass plane is intimately related to both galaxy color and structural morphology, with galaxies lying on the local MS being predominantly blue and disk-like and most galaxies below the MS red and bulge-dominated or spheroidal (Kauffmann et al. 2003a; Wuyts et al. 2011; McPartland et al. 2019). In the past, this was discussed in terms of galaxy bimodality (Strateva et al. 2001; Madgwick 2003; Baldry et al. 2004; Bell et al. 2004; Hogg et al. 2004). Various evolutionary channels from the blue cloud to the red sequence have been proposed; in this context, pathways that involve the rapid shutdown of star formation are referred to as quenching (Bundy et al. 2006; Cattaneo et al. 2006; Dekel & Birnboim 2006; Arnouts et al. 2007; Brown et al. 2007; Faber et al. 2007; Ilbert et al. 2010; Brammer et al. 2011). Peng et al. (2010) popularized the idea of a mass-dependent quenching process, “mass quenching,” which is dominant above stellar masses of $\sim 10^{10.2} M_\odot$. In contrast, at low stellar masses, $M_* < 10^{10} M_\odot$, environmental quenching effects like satellite quenching and merging are believed to be the dominant source of quenching (Hashimoto et al. 1998; Baldry et al. 2006; Peng et al. 2012).

In previous work, to push to lower radio luminosities, Karim et al. (2011) performed stacking on the 1.4 GHz data in the COSMOS field (VLA-COSMOS Large, Deep and Joint projects; Schinnerer et al. 2004, 2007, 2010), drawing on a deep $3.6 \mu\text{m}$ selected parent sample of $> 10^5$ galaxies. Karim et al. (2011) found that the sSFRs of star-forming and quiescent galaxies demonstrate a linear relationship with stellar mass and that both populations show a strong mass-independent increase in their sSFR with redshift out to $z \sim 3$.

The COSMOS field with a coverage of 2 deg^2 is the largest cosmological deep field to date with Hubble Space Telescope (HST) coverage (Scoville et al. 2007) and contains a rich set of panchromatic and ancillary data products, making it an ideal choice for a consistent study of galaxy properties over a sufficient range of stellar masses, redshifts, and environments. Now, with updated multiwavelength photometry (Laigle et al. 2016) and stellar mass functions (Davidzon et al. 2017) available in the COSMOS field, it is timely to revisit the analysis of Karim et al. (2011) and better constrain the MS, the evolution of sSFR, and the SFRD of the universe out to $z \sim 5$. With the latest COSMOS2015 catalog (Laigle et al. 2016) containing new K_s -band photometry 0.7 mag deeper than previously available (e.g., Ilbert et al. 2013), we are able to select a 90% mass-complete sample down to $10^{10} M_\odot$ at $z = 4$. Recent radio data at 3 GHz (Smolčić et al. 2017b) are also deeper (assuming a standard spectral index of $S_\nu \propto \nu^{-0.7}$) than the previous 1.4 GHz imaging maps available (Schinnerer et al. 2010), allowing for better constraints on the average radio flux. The higher angular resolution of the radio images also allows for better matching to multiwavelength counterparts.

We introduce the relevant data sets in Section 2 and determine the average SFRs of galaxies, employing a stacking analysis outlined in Section 3. We present our results for the MS relation for star-forming and all galaxies in Section 4.1. In Section 4.2 we combine our SFR measurements with the stellar mass functions of Davidzon et al. (2017) to explore the cosmic

¹⁷ We would like to caution that measuring the SFR of AGN-host galaxies remains a fundamental challenge for all tracers, including spectral energy distribution models.

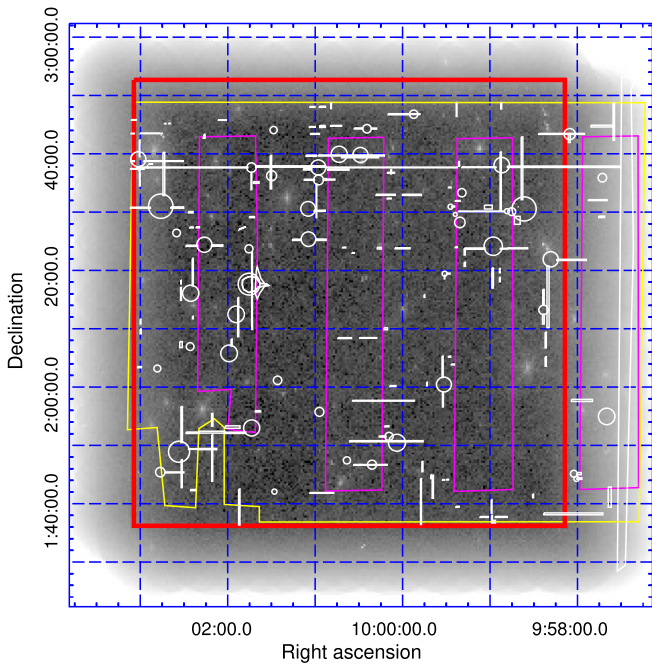


Figure 1. Schematic of the COSMOS field showing the regions of data used. The background image is the VLA-3 GHz LP rms image (Smolčić et al. 2017b). The region used for stacking (where the rms noise is $<3 \mu\text{Jy}/\text{beam}$) is drawn in red. The yellow area is the region covered by the UltraVISTA-DR2 observations (McCracken et al. 2012; Laigle et al. 2016). The ultradeep stripes in the UltraVISTA-DR2 observations are indicated in magenta. White regions indicate masked areas in the optical images, mostly due to bright stars.

SFR activity in the universe as a function of mass and redshift. In Section 4.3, we compare our cosmic SFRD measurements with the literature and discuss systematic uncertainties in these measurements. We report $\text{SFR}-M_*$ measurements for galaxies with different morphological classifications in Section 4.4 and for galaxies in different bins of local density, including a comparison between X-ray group members and field galaxies in Section 4.5. We discuss the implications of our most important results in Section 5 and provide a summary and outlook in Section 6. In the appendices we give further details on tests we have performed (e.g., with mock galaxy samples) to verify our results, and we compare different MS relations using different selections, functional forms, and literature studies. We use a Chabrier (2003) initial mass function (IMF), AB magnitudes, and the cosmological parameters $(\Omega_M, \Omega_\Lambda, h) = (0.30, 0.70, 0.70)$.

2. Data Sets and Sample Selection

2.1. Radio Data

The VLA-COSMOS 3 GHz Large Project (hereafter VLA-3 GHz LP), described in Smolčić et al. (2017b), observed the COSMOS field for 384 hr using the VLA S-band centered at 3 GHz with a 2048 MHz bandwidth. Imaging was performed with a multiscale, multifrequency synthesis algorithm for each pointing separately, tapering each with a Gaussian to achieve a circular beam before creating a final mosaic in the image plane. Across the entire 2.6 square degrees surveyed, 10,830 sources were detected above 5σ using the Blobcat software of Hales et al. (2012). After visual inspection, we identified 67 sources composed of two or more detached components (Smolčić et al. 2017b; Vardoulaki et al. 2019); these sources were removed

from our analysis. A total of 20% of the 3 GHz sources lie outside the UltraVISTA regions (see Figure 1). The astrometry is estimated to be accurate to $0''.01$ based on a comparison to the Very Long Baseline Array—COSMOS survey (Herrera Ruiz et al. 2018).

The observing layout was designed to achieve a uniform rms (median $2.3 \mu\text{Jy}$ at $0''.75$ resolution) over the inner two square degrees with 192 pointings. Because the outermost regions of the map do not contain overlapping pointings, the noise increases rapidly toward the edge. We define a region where the rms of the 3 GHz map is $<3 \mu\text{Jy}/\text{beam}$ to use for the stacking experiment (red box in Figure 1). This area can be defined by $149.53 < \text{R.A. (J2000)} < 150.76 \text{ deg}$ and $1.615 < \text{decl. (J2000)} < 2.88 \text{ deg}$.

2.2. COSMOS2015 Photometry for a Stellar-mass-selected Sample

The COSMOS2015 catalog published in Laigle et al. (2016) provides optical and NIR photometry (in 31 bands) for over 1 million sources detected in z^{++} (SuprimeCam) $YJHK_s$ (UltraVISTA-DR2; McCracken et al. 2012) stacked detection images. The catalog covers a square of 2 deg^2 and uses the UltraVISTA-DR2 “deep” and “ultradeep” stripes, resulting in a depth and completeness that is not uniform across the field. The increased exposure time in the “ultradeep” region, covering an area of 0.62 deg^2 , doubles the number of sources compared to the previous version of the catalog (Ilbert et al. 2013). Regions saturated by stars or bright sources are masked out in the optical to near-IR bands, resulting in a total coverage of 1.77 square degrees.

Photometric redshifts (z_p) were computed using LePhare (Arnouts et al. 1999; Ilbert et al. 2009) and have been calibrated using $\sim 20,000$ spectroscopic targets from the literature. The spectral energy distribution (SED) fitting library is the same as Ilbert et al. (2013).

Stellar masses are derived as described in Ilbert et al. (2015), using a grid of synthetic spectra created using the stellar population synthesis models of Bruzual & Charlot (2003) with a Chabrier (2003) IMF for two metallicities, τ (i.e., declining and delayed) star-formation histories (SFHs), two different dust attenuation curves, and emission-line prescriptions.

We not only require accurate photometric redshifts and stellar masses for selecting our parent samples and subsamples for stacking and SFR calculations, but accurate source positions are also required in order to stack the radio images at the locations of the galaxies of interest. A positional matching of the VLA-3 GHz LP sources with the COSMOS2015 catalog performed using a search radius of $0''.8$ by Smolčić et al. (2017a) found small systematic astrometric offsets that vary across the field.¹⁸ Therefore, before using the optical positions reported in COSMOS2015 as inputs in our stacking routine, we correct for the systematic offset using the best-fitting linear relations reported in Smolčić et al. (2017a):

$$\text{R.A.} = \text{R.A.}_{\text{L16}} + (-0.041\text{R.A.}_{\text{L16}} + 6.1)/3600 \quad (1)$$

$$\text{decl.} = \text{decl.}_{\text{L16}} + (0.058\text{decl.}_{\text{L16}} - 0.147)/3600. \quad (2)$$

¹⁸ These offsets arise from the astrometry of the COSMOS2015 being tied to Megacam i -band data (McCracken et al. 2010, 2012) and will not be an issue in future releases of UltraVISTA data, which are to be tied to Gaia astrometry.

2.2.1. High- z Optimized Parameters from Davidzon et al. (2017)

To optimize the SED fitting for high-redshift galaxies ($z > 2.5$), Davidzon et al. (2017) expanded the grid of allowed redshifts out to $z = 8$ and refit the COSMOS2015 photometry with LePhare using additional high- z templates of extremely active galaxies with a rising SFH, as well as allowing highly attenuated galaxies. The Davidzon et al. (2017) catalog also provides improved removal of stellar contaminants. Overall, there is good agreement between the Laigle et al. (2016) and Davidzon et al. (2017) redshifts, but there is a subsample of objects that moved from $z_{L16} < 1$ to $z_{D17} \sim 3$ because they are now classified as dusty galaxies at high redshift. Other groups of galaxies that changed redshift between the catalogs had no statistical impact on the analysis of Davidzon et al. (2017). In Sections 4.2 and 4.3, we use the stellar mass functions calculated from Davidzon et al. (2017).

Due to the range of templates used, the Davidzon et al. (2017) catalog is not as robust for low- z galaxy properties as the Laigle et al. (2016) catalog, increasing the photometric redshift errors. To combine the low- and high- z optimized catalogs of Laigle et al. (2016) and Davidzon et al. (2017), we adopt the Davidzon et al. (2017) values (such as stellar mass, photometric redshift, and rest-frame colors) for all galaxies with $z_{D17} > 2.5$, and the Laigle et al. (2016) values for all galaxies with $z_{D17} < 2.5$. In this way, we do not double count any galaxies in our sample, but we note that 18,902 galaxies with $z_{D17} < 2.5$ still have $z_{L16} > 2.5$. Therefore, we are biasing our results toward higher redshifts by adopting the z_{L16} in these cases.

2.3. Sample Selection: A Stellar-mass-complete Sample

The K_s band traces the stellar mass of galaxies out to $z \sim 4$. At $z > 4$, the K_s band lies blueward of the Balmer break, and therefore the $3.6 \mu\text{m}$ band must be used. The latter is also a better stellar-mass proxy than the K_s band in the range $2.5 < z < 4$ (see Davidzon et al. 2017). The limiting magnitude of both the K_s and $3.6 \mu\text{m}$ catalogs is $\mathcal{M}_{\text{lim}} = 24$ across the full field. For our highest redshift bin only, we exclusively select galaxies from the ultradeep UltraVISTA regions, where the limiting magnitude is fainter than in the deep regions ($\mathcal{M}_{\text{lim}} = 25$ at $3.6 \mu\text{m}$, for a 70% completeness; Davidzon et al. 2017). To maximize the number of galaxies in each stack, we use the deep UltraVISTA limits ($K_s < 24$) across the entire UltraVISTA COSMOS region out to $z < 2.5$.

To select a stellar-mass-based sample, we apply the following selection criteria:

1. $K_s < 24.0$ for $0.2 < z_p < 2.5$,
2. $3.6 \mu\text{m} < 23.9$ for $2.5 < z_p < 4$, and
3. $3.6 \mu\text{m} < 25.0$ and FLAG_DEEP = 1 for $z_p > 4$,

where the FLAG_DEEP = 1 requirement in the COSMOS2015 catalog means that the galaxies are in the ultradeep UltraVISTA regions. A total of 206,674 galaxies meet these criteria.

Stellar mass completeness is calculated empirically across our subsamples following Pozzetti et al. (2010; see also Moustakas et al. 2013; Laigle et al. 2016, and Pearson et al. 2018). For each galaxy with a redshift and K_s (or $3.6 \mu\text{m}$) band detection, we calculate an estimate of the stellar mass it would need in order to be observed at the magnitude limit (in the K_s band for galaxies $z < 2.5$ and at $3.6 \mu\text{m}$ for galaxies $z > 2.5$):

$\log(M_{*,\text{lim}}) = \log(M_*) - 0.4(\mathcal{M}_{*K_s,\text{lim}} - \mathcal{M}_{K_s})$. In each redshift bin, the faintest 20% of objects were selected, and the $M_{*,\text{lim}}$, above which 90% of these faint galaxies lie, is adopted as our stellar mass completeness limit (e.g., Pozzetti et al. 2010). Using the 3σ limiting magnitudes, we find limiting masses, shown in Figure 2, that are consistent with Laigle et al. (2016) and Davidzon et al. (2017). For Sections 4.4 and 4.5, where different selections and binning schemes are used, mass-completeness limits are calculated as stated above. We only show data above this mass-complete limit unless stated otherwise.

2.4. Galaxy Type and AGN Classifications

The galaxy population is often quoted as being bimodal, with star-forming galaxies and quiescent galaxies having different sSFR distributions.¹⁹ However, without a measure for SFR to begin with (obtaining SFRs is the aim of our radio stacking), we instead rely on galaxy colors to select star-forming (SF) galaxies. Another concern to be addressed in this section is the uncertain contribution of AGN emission to the radio fluxes used to measure star formation activity.

Speagle et al. (2014) showed that studies selecting bluer galaxies, such as those using a Lyman break or BzK selection, find steeper (linear) MS slopes of 0.75–1 than “mixed” studies, such as those using rest-frame color–color cuts, which tend to find slopes of ~ 0.6 , and that studies making no preselection for star-forming galaxies find slopes ≤ 0.4 . In this work, we adopt the color–color selection of Ilbert et al. (2013); quiescent galaxies are those with rest-frame $M_{NUV} - M_r > 3(M_r - M_j) + 1$ and $M_{NUV} - M_r > 3.1$. This method has the advantage of separating dusty star-forming galaxies and quiescent galaxies (e.g., Ilbert et al. 2009; Laigle et al. 2016; Davidzon et al. 2017). We want to emphasize that measuring the MS depends critically on the sample selection, so we discuss it in further detail in Appendix B.1, and we show our results for the commonly used UVJ selection as well as our $NUVrJ$ selection. Out of the 206,674 galaxies that meet our selection criteria, 183,987 are classified as star-forming according to our $NUVrJ$ selection.

Besides sample selection effects, one might expect AGN contamination to be a problem for radio emission because there are radio-loud AGNs that cannot be easily identified as AGNs at other wavelengths. However, these particular objects tend to live in systems with redder colors (e.g., Brown et al. 2001; Smolčić 2009; Morić et al. 2010) and should have been removed from our star-forming galaxy sample at low redshift. For our main analysis, we remove galaxies classified as multicomponent radio sources²⁰ in Vardoulaki et al. (2019) and galaxies classified as AGNs according to their X-ray luminosity (using [0.5–2] keV Chandra data, if the luminosity was $L_X > 10^{42} \text{ erg s}^{-1}$) or observed mid-IR colors (Donley et al. 2012). For sources in the 3 GHz multiwavelength counterpart catalog of Smolčić et al. (2017a), we have flagged and removed sources whose SED is best fit with an AGN + galaxy template and radio excess sources ($\log(L_{1.4}/W \text{ Hz}^{-1}) > \log(\text{SFR}_{\text{IR}}/M_{\odot} \text{ yr}^{-1}) + 21.984 \times (1 + z)^{0.013}$) from Delvecchio et al. (2017).

¹⁹ However, we note that measurements of SFR for quiescent galaxies tend to be highly uncertain, e.g., Salim et al. (2016).

²⁰ Multicomponent radio sources are sources whose radio emission breaks into multiple components (e.g., a radio jet composed of a core and two radio lobes). Including the 9/57 multicomponent galaxies of Vardoulaki et al. (2019) classified as star-forming in our stacks does not change our measurements of median SFRs.

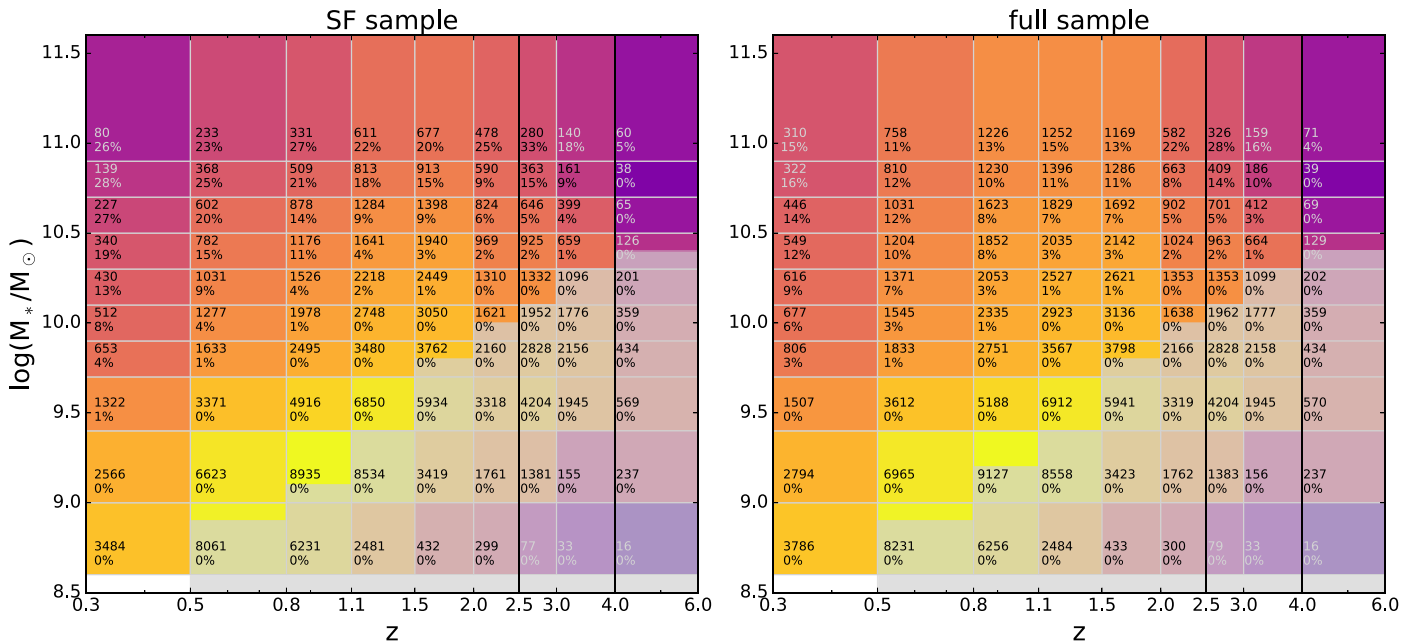


Figure 2. Binning scheme in stellar mass and redshift used for our primary stacking analysis for galaxies that meet our magnitude and area cuts. The color represents the number of galaxies in the bin (also indicated by the top number in the box). The left panel shows galaxies classified as star-forming according to their $NUVrJ$ colors, and the right panel shows our scheme for all galaxies. The vertical black lines at $z = 2.5$ and $z = 4$ show where we transition from using the Laigle et al. (2016) catalog to the Davidzon et al. (2017) catalog and from selecting galaxies across the full COSMOS field to selecting galaxies only from the UltraVISTA Ultra-Deep regions, respectively. The bottom number in each bin shows the percentage of galaxies detected in the 5σ VLA-3 GHz catalog, ranging from $\sim 30\%$ in the most massive bins to 0% at stellar masses $< 10^{9.6} M_{\odot}$. Regions below the stellar mass-completeness limits have gray shading overlaid.

In Appendix B.2, we show how the results would be affected by including AGNs in our SF galaxy sample: the median SFR is not significantly altered from before, but the mean SFR is, particularly for the most massive galaxies, where the mean SFR can be up to a factor of 3 higher with AGNs. When considering all galaxies, we include galaxies of red colors, which are more likely to host a radio AGN, especially at the massive end (e.g., Auriemma et al. 1977; Sadler 1982; Fabbiano et al. 1989; Smolčić 2009; Brown et al. 2011). In the local universe, all galaxies with stellar mass $M_{*} > 10^{11} M_{\odot}$ show radio-AGN activity with $L_{150 \text{ MHz}} > 10^{21} \text{ W Hz}^{-1}$ (Sabater et al. 2019). The most massive bins ($10.9 < \log_{10}(M/M_{\odot}) < 11.6$) are the most affected by our AGN removal. For these most massive galaxies, the 3 GHz flux overestimates the SFR when considering galaxies with red $NUVrJ$ colors, due to flux contribution from the AGN, and the difference is strongest at $z < 2$. We also note that this discrepancy at high mass is stronger ($>4\sigma$) when comparing mean rather than median SFRs for the two different AGN deselection methods. Our final sample after AGN removal consists of 204,903 galaxies, including 182,730 SF galaxies.

2.5. Morphological Parameters

Morphological measurements were carried out on HST/Advanced Camera for Surveys (ACS) F814W (I -band) images with a resolution of $\sim 0''.15$ (Koekemoer et al. 2007) to create the Zurich Structure and Morphology Catalog (ZSMC²¹). We have matched the ZSMC, complete down to $I \leq 24$ mag, with the COSMOS2015 photometric catalog of Laigle et al. (2016). Galaxies in ZSMC were classified as “early type,” “late type,” or “irregular/peculiar” according to the Zurich Estimator of

Structural Types algorithm (ZEST; Scarlata et al. 2007). The ZEST algorithm performs a principal component analysis on five nonparametric structural estimators: asymmetry, concentration, Gini coefficient, M_{20} , and ellipticity. The bulginess classification of late-type galaxies was additionally based on Sérsic indices derived from single-component GIM2D fits (Sargent et al. 2007), available for the brightest galaxies $I \leq 22.5$.

To study the sSFR of galaxies in different morphology classes, we separate galaxies into four classes: ZEST type = 1 (early type, ET), ZEST type = 2.0 or 2.1 (bulge-dominated late type), ZEST type = 2.2 or 2.3 (disk-dominated late type), and ZEST type = 3 (irregular). Because we only have HST imaging in one band, we are unable to account for morphological k -corrections (due to color gradients in galaxies), and, as such, we limit our analysis to $z < 1.5$, where the I -band traces the stellar light (see Scarlata et al. 2007).

2.6. Environmental Parameters

Scoville et al. (2013) probed the large-scale structure of the COSMOS field by measuring galaxy surface density in 127 redshift slices in the range $0.15 < z < 3.0$ using 155,954 K_s -band-selected galaxies from the photometric redshift catalog of Ilbert et al. (2013). We use the Voronoi tessellation results, which provide a density estimate for all galaxies because it yields a 2D surface density in each redshift slice. The local environment is described by δ , the density per comoving Mpc^2 at the location of each source with the mean density of the redshift slice subtracted.

We also investigate the average radio-based SFR properties of galaxies lying inside X-ray groups in the COSMOS field. The primary X-ray galaxy group catalogs were presented by Finoguenov et al. (2007) and George et al. (2011) and used available X-ray data of Chandra and XMM-Newton with

²¹ Available on IRSA <https://irsa.ipac.caltech.edu/data/COSMOS/tables/morphology/>.

photometric data sets and identified groups with secure redshift out to $z = 1.0$. The sample of X-ray galaxy groups used in this study is selected from two recent catalogs of 247 and 73 groups presented by Gozaliasl et al. (2019) and G. Gozaliasl et al. (2020, in preparation). The X-ray emission peak/center of groups is determined with an accuracy of $\sim 5''$ using the smaller-scale emission detected by high-resolution Chandra imaging. The new X-ray groups have a mass range of $M_{200c} = 8 \times 10^{12}$ to $3 \times 10^{14} M_{\odot}$ with a secure redshift range of $0.08 < z < 1.53$. Here, M_{200c} is the total mass of groups, which is determined using the scaling relation L_X - M_{200c} calibrated by weak lensing (Leauthaud et al. 2010). For the full details of group identification and their properties, we refer readers to Gozaliasl et al. (2019).

For our study of the MS relation in X-ray groups, we focus our analysis on one particular redshift bin, $0.64 < z < 0.88$, which includes 73 groups with $M_{200c} = 2 \times 10^{13}$ to $2.5 \times 10^{14} M_{\odot}$. The X-ray group members are selected within R_{200c} from the group X-ray centers using the COSMOS2015 photometric redshift catalog. We note that $\sim 31\%$ of the group galaxies have spectroscopic redshifts.

3. Methods: Radio Stacking, Flux Measurement, and SFR Calculation

We summarize our stacking workflow here and will justify the choices made in Appendix A. In principle, stacking is a straightforward process, but in practice, there are many subtleties that we discuss here and in Appendix A.

1. First, an input list of coordinates is created for the N_{objs} galaxies to be stacked, taking into consideration the selection criteria and positional offsets described in the previous section.
2. Using the stacking routine developed by Karim et al. (2011),²² we create $40'' \times 40''$ (200×200 pixels) cutouts of the 3 GHz image, centered on the input position of each galaxy. The cutouts are saved together as a data cube of size $N_{\text{objs}} \times 200 \times 200$. The stacking routine also calculates the median image of the cutouts and saves the central pixel value (which should be the peak flux) and the rms.
3. To calculate the total flux, we fit a 2D elliptical Gaussian function to the mean image,²³ restricted to the central $8'' \times 8''$ (40×40 pixels). We input initial conditions for the fit using the peak flux from the stacking routine and the beam size.
4. To estimate the uncertainty on the total flux, we perform a bootstrap analysis. This involves randomly drawing, with replacement, N_{objs} galaxy cutouts (from our initial list of galaxies) and creating a new mean stack. We then record the total flux for each resulting stack and repeat the process 100 times. We report the 5th, 16th, 50th, 84th, and 95th percentiles of the total fluxes. Tables F1 and F2 show the 5th and 95th percentiles as the lower and upper errors. In this way, our errors on the total flux are indicative of the sample variance.

²² We have verified the performance of the routine by inserting artificial Gaussian sources into the 3 GHz map and recovering the stacked images.

²³ We discuss the advantages and disadvantages of median and mean stacking in Appendix A.2.

A note on total fluxes: Point sources can be described entirely by their peak cleaned flux, which, if the optical and radio centers are aligned, should correspond to the central pixel in each cutout. Galaxies in the 3 GHz image are not just point sources, so we have to take into account the source extent. Indeed, Bondi et al. (2018) found that 77% of star-forming galaxies are resolved in the VLA-3 GHz LP. Jiménez-Andrade et al. (2019) show that the physical effective radius of the 3 GHz component is 1–2 kpc in star-forming galaxies and is relatively constant with stellar mass and evolves shallowly with redshift out to $z \sim 2.25$. Astrometric uncertainty also plays a role in the determination of total flux and is a second key reason why the peak flux from the stack cannot be used to represent the total flux. Jittering of sources due to astrometric offsets between the optical catalog and the true 3 GHz source position causes an effective blurring of the stacked image. For sources in the 5σ VLA catalog, the differences between the 3 GHz and COSMOS2015 positions have a spread of $\sigma = 0''.1$ (after correcting for the systematic offset; Smolčić et al. 2017a), which is half the size of a pixel. We discuss more details about the tests we have performed to verify our methods in Appendix A.

3.1. Radio–SFR Calibration

The most commonly used radio–SFR calibrations are bootstrapped from the empirical IR–radio correlation. For our results, we have adopted an SFR calibration based on the IR–radio correlation determined by Molnár et al. (2020) and a radio spectral index²⁴ of $\alpha = -0.7$ unless stated otherwise. The following explains how we convert observed flux at 3 GHz to an SFR.

Observed 3 GHz fluxes ($S_{3 \text{ GHz}}$; $\text{W Hz}^{-1} \text{ m}^{-2}$) are converted to rest-frame 1.4 GHz luminosities ($L_{1.4 \text{ GHz}}$; W Hz^{-1}) where the infrared–radio correlation is traditionally calibrated, via

$$L_{1.4 \text{ GHz}} = \frac{4\pi D_L^2}{(1+z)^{\alpha+1}} \left(\frac{1.4 \text{ GHz}}{3 \text{ GHz}} \right)^{\alpha} S_{3 \text{ GHz}}, \quad (3)$$

where D_L is the luminosity distance to the galaxy and α is the spectral index. It is standard in the literature to assume a single spectral index for the radio spectral energy distribution (usually taken to be $\alpha = -0.7$ or $\alpha = -0.8$). The spread in spectral indices is observed to be $\sigma = 0.35$ (e.g., Smolčić et al. 2017b), and the uncertainty of the spectral index can induce significant errors in the derived radio luminosity for a single object. However, on a statistical basis, the symmetry of the spread is expected to cancel out the variations, typically yielding a valid average luminosity for the given population (see Delhaize et al. 2017; Novak et al. 2017; and Smolčić et al. 2017a for more specific discussions on this topic).

The relation between the radio and far-IR luminosities of star-forming galaxies is assumed to arise because both emissions depend on the recent massive star formation (e.g., Condon 1992; Yun et al. 2001; Bell 2003; Lacki et al. 2010). Helou et al. (1985) first introduced the commonly used parameter q_{TIR} , the ratio of infrared-to-radio luminosity:

$$q_{\text{TIR}} = \log \left(\frac{L_{\text{TIR}}}{3.75 \times 10^{12} \text{ Hz}} \right) - \log \left(\frac{L_{1.4 \text{ GHz}}}{\text{W Hz}^{-1}} \right). \quad (4)$$

²⁴ $S_{\nu} \propto \nu^{\alpha}$.

The infrared-to-radio ratio q_{TIR} has been observed to decrease with redshift (e.g., Seymour et al. 2009; Ivison et al. 2010a, 2010b; Basu et al. 2015; Magnelli et al. 2015; Calistro Rivera et al. 2017; Delhaize et al. 2017; Ocran et al. 2020), but we note some studies have found no significant evolution (e.g., Garrett 2002; Appleton et al. 2004; Sargent et al. 2010). The reason for this observed evolution is currently unclear; however, evolution in the SFR surface density, selection effects, and the presence of radio AGNs have been suggested as possible explanations (Magnelli et al. 2015; Molnár et al. 2018, 2020).

Molnár et al. (2020) found, for a flux-matched sample of star-forming galaxies at $z < 0.2$, that q_{TIR} depends on radio luminosity:

$$q_{\text{TIR,SF}} = (-0.153 \pm 0.008) \cdot \log(L_{1.4\text{ GHz}}) + (5.9 \pm 0.2). \quad (5)$$

We combine Equations (3)–(5) to compute L_{TIR} for a given 3 GHz flux and redshift. Finally, we derive SFRs using the total infrared calibration in Kennicutt & Evans (2012) for a Chabrier IMF.

In Figure 3 we compare some literature SFR relations. We compare recipes that directly calibrate $L_{1.4\text{ GHz}}$ to SFR, where the SFR comes from another tracer, namely multiband UV+IR (Davies et al. 2017), $H\alpha$ (Brown et al. 2017; Boselli et al. 2015), and FUV+IR (Bell 2003). We also include two calibrations for q_{TIR} as a function of redshift determined by Delhaize et al. (2017) and Magnelli et al. (2015). Magnelli et al. (2015) also performed stacking with a mass-selected sample and confirmed that q_{TIR} does not depend significantly on the offset from the MS, nor does the radio-spectral index, at $M_* > 10^{10} M_\odot$ and to $z < 2.3$.

The relevant radio powers used to derive the calibrations are highlighted as horizontal bars in Figure A1. For the local results (shown as solid lines), the calibrations are more consistent with each other at lower luminosities (with the exception of Bell 2003). However, even in the range of radio luminosities covered by all samples, $21 < \log(L_{1.4\text{ GHz}}) < 23$, there are significant discrepancies of up to 0.4 dex. The largest discrepancy between calibrations occurs for radio luminosities above those probed in the local universe and used as calibration samples ($L_{1.4\text{ GHz}} > 10^{24} \text{ W Hz}^{-1}$). At $z = 0.3$, switching from a Delhaize et al. (2017) to a Bell (2003) SFR calibration at the lowest radio luminosities would decrease the SFR by 0.2 dex, whereas at $z = 2.5$ the difference would be 0.6 dex. At the highest luminosities, the Bell (2003) SFRs are 0.4 dex higher than the Delhaize et al. (2017) SFRs at $z = 0.3$ and ~ 0.1 dex lower at $z = 2.5$. We also note the above SFR calibrations have not been tested on quiescent galaxies, so our SFR measurements for “all” galaxies must be taken with caution.

4. Results

4.1. Galaxy SFR– M_* Relation

In this section, we present our measurement of the MS relation and discuss its functional form. Measurements for median redshift, peak 3 GHz flux, total flux, and SFR are given at the end of the paper for mean stacks of star-forming and all galaxies. The MS derived from these data is shown in Figure 4.

Star-forming galaxies show a positive correlation between SFR and stellar mass at all redshifts. As expected, the SFRs of

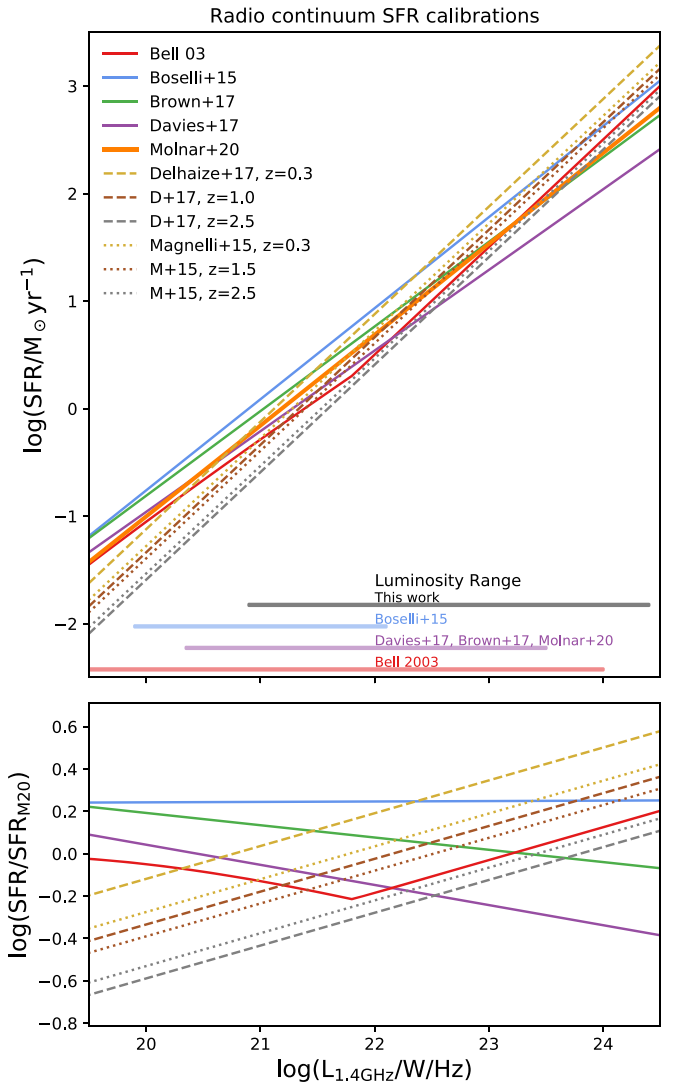


Figure 3. Comparison of 1.4 GHz radio-continuum luminosity SFR calibrations from the literature. For the redshift-dependent “ q_{TIR} ” from Delhaize et al. (2017) and Magnelli et al. (2015), we show the calibration at $z = 0.3$ (gold), $z = 1.5$ (plum), and $z = 2.5$ (gray), as solid, dashed, and dotted lines, respectively. Horizontal bars at the bottom of the top panel illustrate the radio luminosity range over which different SFR calibrations were derived. Red shows the range from Bell (2003), and purple shows the range from Davies et al. (2017), which is comparable to other studies that also rely on the FIRST survey (e.g., Brown et al. 2007; Molnár et al. 2020). The rest-frame 1.4 GHz luminosity range probed by our 3 GHz COSMOS stacks is shown in black and extends to higher luminosities than probed by the local studies. The bottom panel shows the difference between calibrations normalized to the Molnár et al. (2020) calibration adopted in this work.

“all” galaxies agree well with “SF galaxies” at lower masses where most galaxies are classified as SF but disagree at higher masses, showing a “turnover.” Including quiescent galaxies in the sample of all galaxies results in a flatter MS relation at $z < 2$ for $\log(M_*/M_\odot) > 9.5$. A less-extreme flattening is also present in the star-forming galaxy sample at low z for high masses.

How should we define the MS? Is there a definition that gives a natural insight into the physical processes involved, or one that makes it the most straightforward to conduct intersample studies? Renzini & Peng (2015) suggested the MS should be defined as the ridgeline of the star-forming peak in a 3D logarithmic SFR– M_* –number plane, and similar

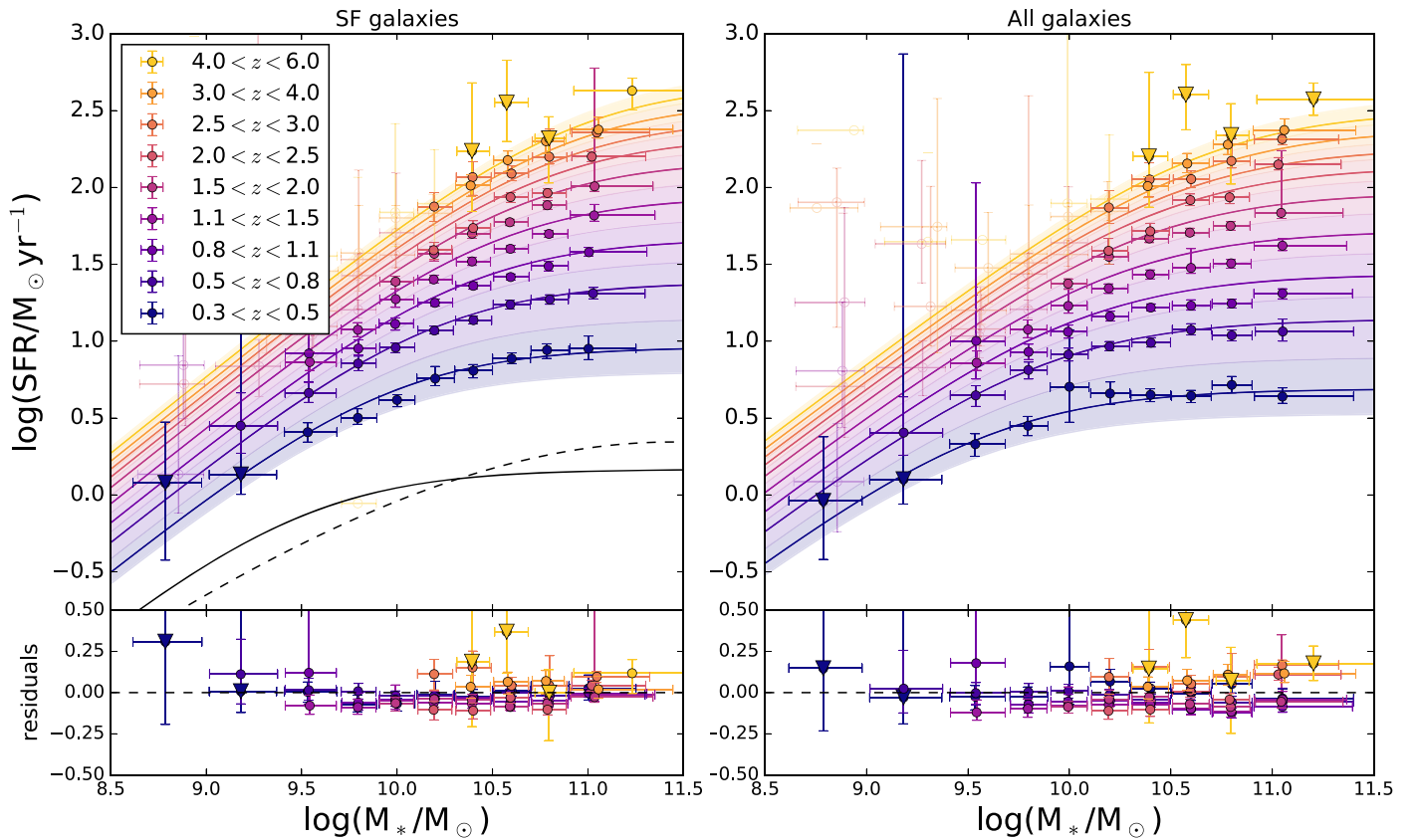


Figure 4. Galaxy radio SFR–stellar mass relation for SF galaxies (left panels) and all galaxies (right panels). We show errors (2σ) on the median SFR from our bootstrapping analysis of the stacked fluxes. The error bars in the x -direction show the 2σ variation of stellar masses within each redshift bin. Only stellar-mass-complete bins (shown as opaque circles) with peak signal-to-noise ratio (S/N) > 10 are used for the fitting. Bins suffering from mass incompleteness are shown as transparent symbols, and radio stacks with S/N < 10 are shown as down-facing triangles. We parameterize the relation according to Equation (6), allowing for a flattening at high stellar masses. The solid line shows the relation at the median galaxy redshift across each redshift bin, and the shaded areas show the evolution of the MS over the redshift bin. The dashed line in the left panel is the MS for Sloan Digital Sky Survey (SDSS) galaxies from Saintonge et al. (2016). The solid black line shows an extrapolation of our MS to $z = 0.035$. Bottom panels show residuals measured as $\log(\text{SFR})$ –best-fit model $\log(\text{SFR})$.

definitions have been adopted by, for example, Hahn et al. (2019) and Magnelli et al. (2014). Naturally, this method requires robust SFR and M_* measurements for large numbers of galaxies. Many studies find that star-forming galaxies follow a log-normal SFR distribution at a fixed stellar mass (Popesso et al. 2019a). For a log-normal distribution, the mode and the median of the (linear) SFR are related to each other by the width of the distribution, and we note that the mean SFR will be higher than the median.

In our analysis, we do not distinguish starburst galaxies lying above the log-normal MS for SF galaxies; they are all included in the stack. Results do not yet agree about how the fraction of starburst galaxies varies with stellar mass and redshift (e.g., Sargent et al. 2012; Schreiber et al. 2015, and Bisigello et al. 2018). However, the number of starburst galaxies that lie above the MS is small (5%–20% of SF galaxies) and should not drastically affect our results.

The appropriate form of the MS depends on the stellar mass range under consideration. Using the deep GOODS fields in addition to the COSMOS field allowed Whitaker et al. (2014) to constrain the steeper, lower-mass end ($\log(M_*/M_\odot) < 10.0$) of the MS. To combine the steep low and shallow high mass relations, a turnover is required (see also Bisigello et al. 2018). At the high-mass end in the local universe, $M_* > 10^{11} M_\odot$, there are very few star-forming galaxies, and their SFRs are highly uncertain and depend sensitively on the SFR calibration

used (Popesso et al. 2019a); these galaxies are critical for determining the flattening of the MS.

Figure 4 shows that below $z < 1$, a flattening in the MS is observed in our sample, so we would like to fit a functional form that allows this.²⁵ We cannot constrain the low-mass slope at high redshifts because of the mass-completeness limitations imposed by the current COSMOS data, nor at low redshifts, due to insufficient S/N in our stacks (see, e.g., Appendix A.3). Recent simulations predict a constant $\log(\text{sSFR})$ at low stellar masses ($M_* < 10^{9.5} M_\odot$), out to $z \sim 5$ (e.g., Torrey et al. 2018; Matthee & Schaye 2019; see also Iyer et al. 2018 for low-mass slope constraints based on SFHs reconstructed from observations), supporting our decision to fix the low-mass power-law slope to unity (see also, e.g., Schreiber et al. 2015). In Appendix C, we have tested the performance of the linear form of Speagle et al. (2014) and the nonlinear MS forms of Schreiber et al. (2015) and Tomczak et al. (2016) at describing our data. Here, we introduce a new form in Equation (6), inspired by Lee et al. (2015):

$$\log(\langle \text{SFR} \rangle) = S_0 - a_1 t - \log \left(1 + \left(\frac{10^{M'_t}}{10^M} \right) \right),$$

$$M'_t = M_0 - a_2 t, \quad (6)$$

²⁵ We show in Appendix C that a flattening of the form proposed by Lee et al. (2015) is strongly preferred over a linear model at $z < 1.5$.

Table 1

Best-fit Parameters (and $1 - \sigma$ Errors) of the MS (Equation (6)) Fit to SFRs Determined from Mean 3 GHz Fluxes for Galaxies as a Function of Stellar Mass and Redshift

Sample	S_0	M_0	a_1	a_2
SF	$2.97^{+0.08}_{-0.09}$	$11.06^{+0.15}_{-0.16}$	$0.22^{+0.01}_{-0.01}$	$0.12^{+0.03}_{-0.02}$
All	$2.80^{+0.08}_{-0.09}$	$10.8^{+0.15}_{-0.17}$	$0.23^{+0.01}_{-0.01}$	$0.13^{+0.03}_{-0.02}$

Note. These fits are demonstrated in Figure 4.

where M is $\langle \log(M_*/M_\odot) \rangle$ and t is the age of the universe in Gyr. We found that the choice of redshift or time evolution, for example, z , $\log(1+z)$, or t , plays an important role in the number of parameters required for a good fit. Our new parameterization takes into account the evolution of the normalization ($S_0 + a_1 r$) and turnover mass (M'_t) and assumes a low-mass slope of unity.

We fit our model to the data using SCIPY’s OPTIMIZE.CURVE_FIT, which uses the Levenberg–Marquardt least-squares algorithm, only considering mass-complete data (opaque points in Figure 4). Based on our simulations (see Appendix A.3), we find that stacks with $S_p/\text{rms} < 10$ can bias the recovered mean fluxes by more than 10%–20%, so we only use $S_p/\text{rms} < 10$ data for our fitting. To estimate the parameter uncertainties, we resample the data and vary the stellar mass, SFR, and redshift values of each stack by a random amount that follows a Gaussian distribution with σ given by our upper and lower errors. The SFR error comes from the flux error (of our bootstrapping analysis), and for this, we have assumed that the errors follow a normal distribution in flux. The σ for stellar mass and redshift values come from the standard deviations of stellar masses and redshifts of galaxies within the bin. We have resampled the data with replacement 50,000 times²⁶ and recorded the best fit for each new sample. The median and 16th and 84th percentiles from all our converged runs are reported for the model parameters in Table 1. The best-fit parameter distributions are also shown in Figure 5. For the remainder of this work, we use our MS results from Equation (6) unless stated otherwise. In the left panel of Figure 4, we show the extrapolation of our MS model to low redshift, $z = 0.035$, in comparison to the MS found by Saintonge et al. (2016) for SDSS galaxies in the stellar mass range $8.5 < \log(M_*/M_\odot) < 11.5$. We find a turnover mass that increases with redshift. Studies such as Tomczak et al. (2016) and Lee et al. (2018) have also found that the turnover mass increases with redshift. The model of Peng et al. (2010) expects mass-quenching processes to be the dominant cause of quiescent galaxies at high stellar mass, $M_* > 10^{10.2} M_\odot$. The high-mass MS flattening may be a result of including galaxies that are in the process of “mass quenching” in our sample.

Figure 6 shows the sSFR of SF galaxies as a function of redshift. At all epochs, the most massive galaxies have the lowest sSFR. For galaxies following the functional form proposed in this work, the sSFRs span a smaller range at high redshift and become more divergent toward the present time, with massive galaxies evolving faster, decreasing their sSFR at earlier epochs. Figure 6 shows how our form compares with the canonical Speagle et al. (2014) MS at four different mass bins. The Speagle et al. (2014) model shows a smaller range of sSFR values, underpredicting our measured sSFRs at low mass and overpredicting them at high stellar mass.

Davidzon et al. (2018) used the differential evolution of the galaxy stellar mass function to infer the sSFR evolution of galaxies. Using the stellar mass functions from Davidzon et al. (2017) and Grazian et al. (2015, for $z > 4$), they report a shallow evolution of the sSFR $\sim (1+z)^{1.1}$ at $z > 2$, consistent with, for example, Tasca et al. (2015). We also show the results from Davidzon et al. (2018) in Figure 6 for their lowest and highest stellar mass bins, $\log(M_*/M_\odot) = 10.3$ and 11, respectively. The evolution with redshift matches well the evolution seen in our data, and our results are consistent within the large error bars. However, our mean-stacked sSFRs are systematically higher than those inferred by Davidzon et al. (2018).

4.2. Characteristic Stellar Mass

Karim et al. (2011) found that the majority of new stars formed since $z \sim 3$ were formed in galaxies with a mass of $M_* = 10^{10.6 \pm 0.4} M_\odot$. Stellar mass functions reported in Davidzon et al. (2017) provide information on the number of galaxies that exist per comoving cubic megaparsec as a function of stellar mass and at each redshift. In this section, we combine our 3 GHz MS results with the stellar mass functions reported for star-forming galaxies (“active galaxies”) in Davidzon et al. (2017) to determine the cosmic SFRD. At $0.2 < z < 3.0$, a double Schechter (1976) stellar mass function was fit to the data:

$$\Phi(M)dM = e^{-\frac{M}{M^*}} \left[\Phi_1^* \left(\frac{M_*}{M^*} \right)^{\alpha_1} + \Phi_2^* \left(\frac{M_*}{M^*} \right)^{\alpha_2} \right] \frac{dM_*}{M^*}, \quad (7)$$

whereas at higher redshift, a single Schechter function was used (Davidzon et al. 2017). The low-mass slope shows a progressive steepening moving toward higher redshifts, decreasing from -1.29 ± 0.03 at $z \sim 0.35$ to -2.12 ± 0.05 at $z \sim 5$ for star-forming galaxies (Davidzon et al. 2017).

First, the SFR density as a function of stellar mass is estimated by multiplying the stellar mass function with the mean SFR derived for each mass and redshift bin from our mean stacking. The results are shown in Figure 7. Vertical lines in the figure show the stellar mass above which the COSMOS sample is 90% complete. The top left panel, showing all redshifts together, reveals that the SFR density peaks at $1.5 < z < 2$. The SFR density per stellar mass bin is peaked, showing a characteristic stellar mass that contributes most to the SFR density at a given redshift out to $z = 2.5$. We find that the SFR density becomes more and more tightly peaked out to $z = 2.5$ and that most new stars are formed in galaxies with a characteristic stellar mass that increases with redshift (see upper right panel of Figure 7). Contrary to the finding of Karim et al. (2011, whose MS was well fit with a power-law relation), with our deeper parent catalogs, we find an evolving characteristic mass that shows signs of cosmic downsizing, in which the most massive galaxies formed first (Rodighiero et al. 2010; Thomas et al. 2010; Davé et al. 2016; Siudek et al. 2017).

The evolving characteristic mass is closely connected to the turnover mass of the MS. In Figure 7 (top right panel), we show the evolution in the characteristic mass corresponding to the peak SFR density and the evolution of the turnover mass of the MS from both this work and from Gavazzi et al. (2015), Tomczak et al. (2016), and Lee et al. (2018). Our MS turnover mass (shown in blue) matches well with Tomczak et al. (2016) at $z < 2$ and matches with Lee et al. (2018) for $z > 2$. At $z > 3$

²⁶ However, generally, less than half of these runs converge.

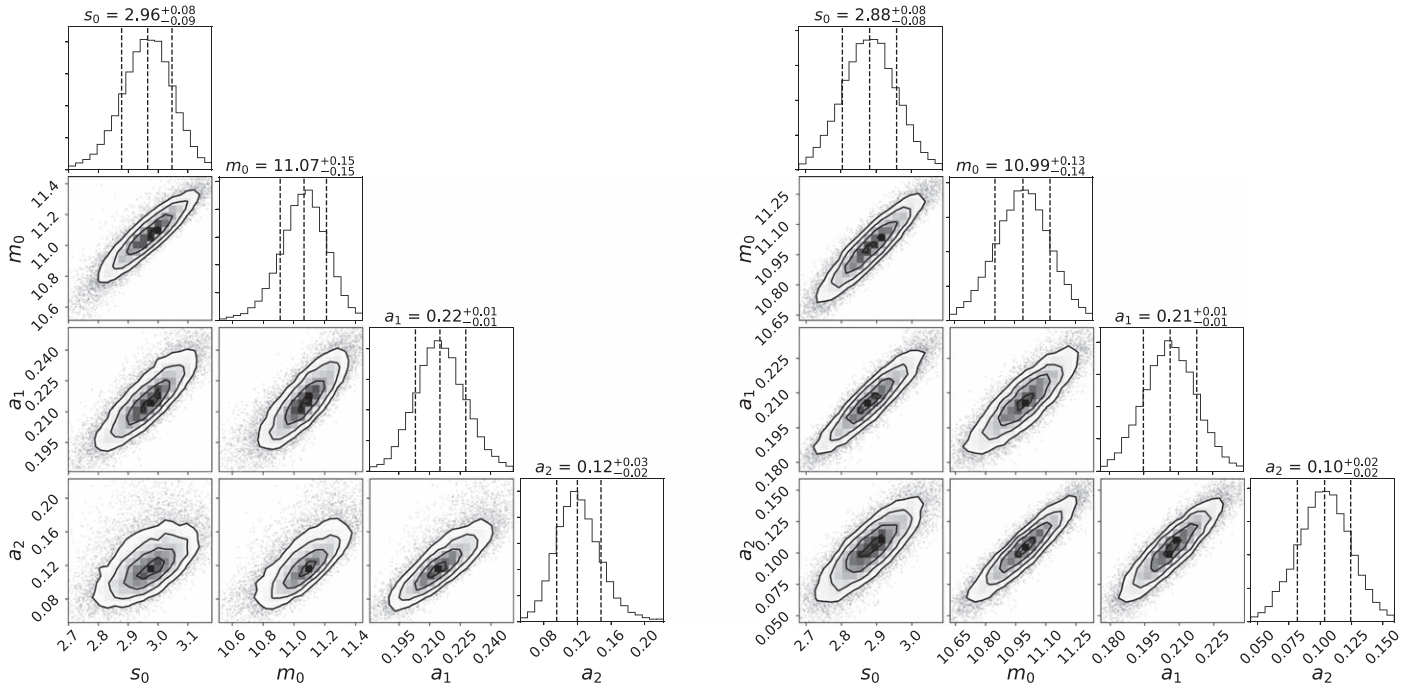


Figure 5. One- and two-dimensional projections of the marginalized posterior probability distributions of parameters in our model. The left panels show results from fitting the model from Equation (6) to star-forming galaxies. Right-hand panels show results for fitting our model to all galaxies. Medians and widths of the marginalized distribution for each parameter are given above the histograms of each parameter and are also reported in Table 1.

our COSMOS data is no longer complete past the characteristic mass, so it is unconstrained in the highest z -bin shown ($3.5 < z < 4$).

4.3. Cosmic SFR Density of the Universe

By integrating the curves shown in Figure 7 over the stellar mass range $M = 10^8 - 5 \times 10^{12} M_\odot$, we report the contribution of star-forming galaxies to the SFR density of the universe as a function of redshift in Figure 8. The MS is parameterized in terms of $\log(\text{SFR})$. However, when we multiply with galaxy stellar mass functions, we need to convert to a linear SFR scale: $\log(\text{mean}(\text{SFR}))$. Assuming a log-normal SFR distribution leads to an offset of $\text{mean}(\log(\text{SFR})) - \log(\text{mean}(\text{SFR})) = -0.5 \ln(10) (\sigma/\text{dex})^2$ (Padoan & Nordlund 2002). Assuming a scatter of 0.29 dex (Popesso et al. 2019b), we have therefore scaled our SFRD down by 0.1 dex.

In addition to our results, we show the Madau & Dickinson (2014) literature compilation curve and recent radio (purple symbols) or IR (red symbols) studies. Our SFRs (blue squares) lie above the classic Madau & Dickinson (2014) results at $z < 2$.

We also calculate lower limits on the cosmic SFRD, free from assumptions about the MS form and stellar mass function, by multiplying the average radio flux in each stack by the number of galaxies in the stack and normalizing by the comoving volume probed by the redshift range considered. The area used for our stacking experiment is 1.55 deg^2 (Section 2), and the cosmological volume was calculated for each redshift slice using the CELESTIAL package by A. Robotham. The resulting (lower limit) SFRD values are shown as stars in Figure 9. We only sum over mass-complete bins and do not apply a completeness correction because that would require assumptions about the stellar mass function or luminosity function (e.g., Liu et al. 2018). This is why our cosmic SFRD limits calculated in this way drop to low values at high redshift in Figure 9, where we are no longer probing past the knee of the stellar mass function.

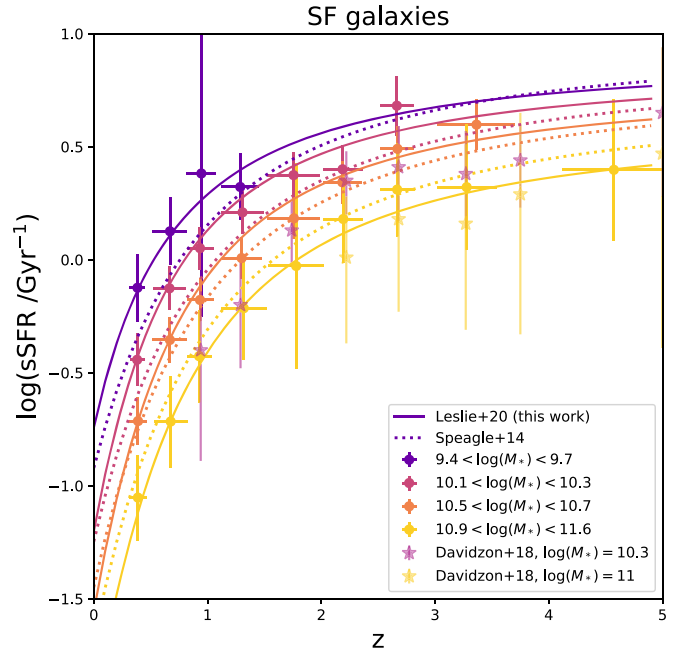


Figure 6. Evolution of sSFR for galaxies at four representative stellar masses. Solid lines show the best fit of Equation (6). The Speagle et al. (2014) MS, converted to our Chabrier (2003) IMF, is shown in dotted lines for comparison. Only four stellar mass bins are shown for clarity, and data points indicate redshifts where the COSMOS sample is complete. Our data and fitted MS is particularly different from the Speagle et al. (2014) MS at the low- and high-mass ends. Stars show sSFRs in two stellar mass bins inferred from the differential evolution of the stellar mass function in COSMOS (Davidzon et al. 2018).

4.3.1. Systematic Uncertainties

In Figure 9, we show the systematic variations that different choices of SFR calibration can have on the cosmic SFRD. The purple triangles in Figure 9 show the cosmic SFRD inferred

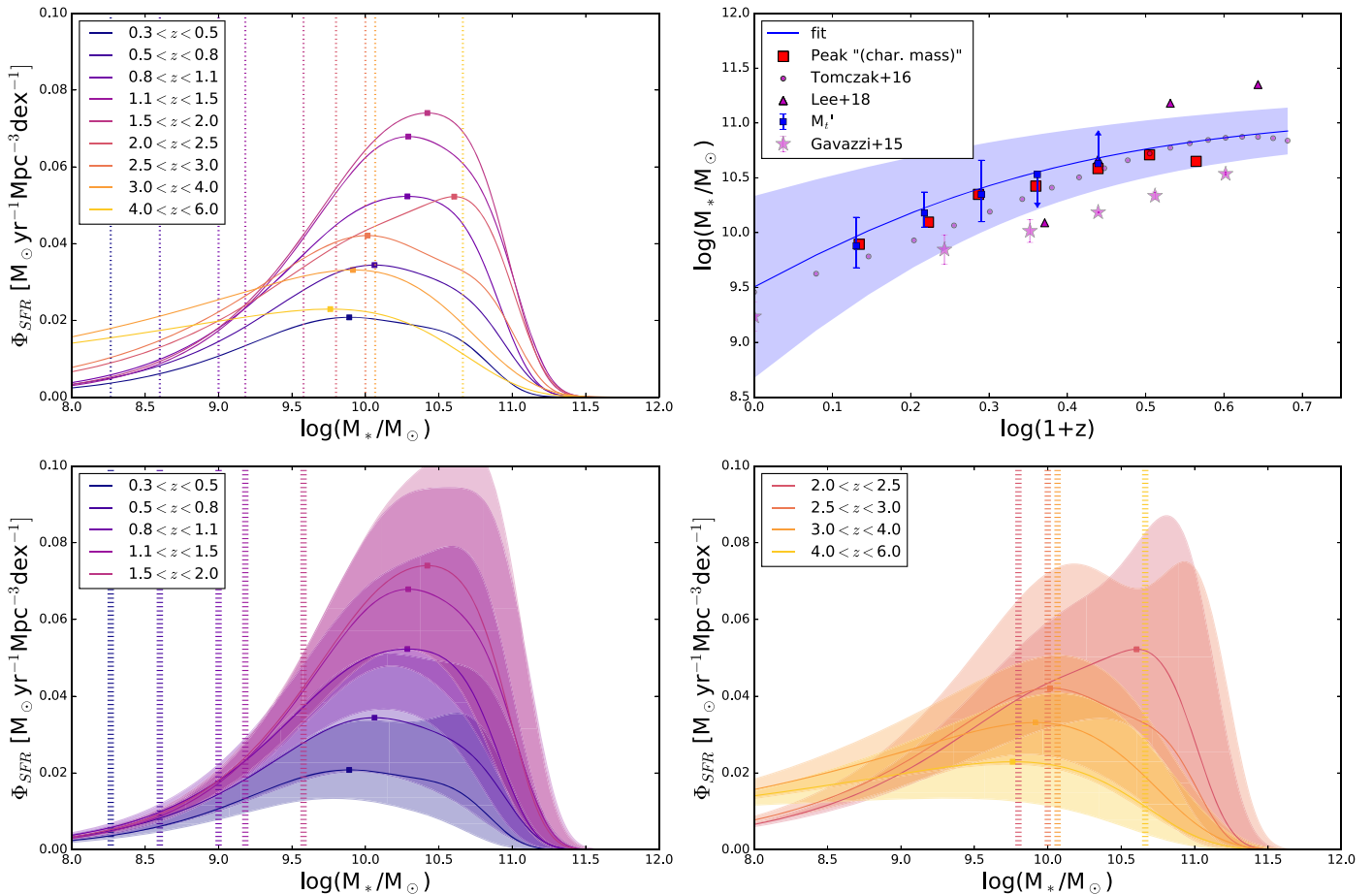


Figure 7. Distribution of the SFR density as a function of stellar mass at different epochs out to $z \sim 4$. We plot the function that results from multiplying the best-fit radio-derived SFR sequence at a given epoch with the corresponding stellar mass function for star-forming galaxies from Davidzon et al. (2017). The top left panel shows a summary of all redshift bins together. The bottom left panel shows data at $z < 2$, and the bottom right panel shows $z > 2$. The uncertainty range was obtained by combining the uncertainties on the stellar mass function’s Schechter parameters with the MS at the minimum and maximum redshift of our bins. At each epoch, our COSMOS data is not mass-complete below the stellar mass limits indicated by vertical dotted lines. The stellar mass corresponding to the peak SFR density is indicated as a square. The top right panel shows how this “characteristic” mass evolves with redshift (out to $z = 3$; red squares). The evolution in characteristic mass is driven by the evolving turnover mass in our MS. We fit the Lee et al. (2015) MS form for each z bin individually in Appendix C, which gives M_0 (blue squares; see Table C1). Our best-fit functional form $M_t = M_0 + a_2 t$ in Equation (6) is shown as a blue line (with 1σ confidence level shaded).

from integrating the Novak et al. (2017) luminosity functions over the luminosity range actually covered by the 5σ detections. Large extrapolations are required to account for the unobserved population of galaxies.

SFR calibrations: To illustrate the differences in SFR calibrations, we show in Figure 9 lower limits of the cosmic SFRD from summing our average SFR multiplied by the number of galaxies in the stack divided by the volume probed in the stack (series labeled “sum”).

When we rerun our MS analysis using the Delhaize et al. (2017) SFR calibration adopted by Novak et al. (2017), we find a worse agreement (SFRD values too high) at low redshifts compared to Madau & Dickinson (2014). We report the best-fitting MS parameters found for this calibration, and the others mentioned below, in Table 2.

We have also tested the power-law 1.4 GHz SFR calibration from Davies et al. (2017). Although this nonlinear SFR calibration works well with our 3 GHz data (light pink stars in Figure 9) for reproducing the local literature cosmic SFRD values at $z < 0.7$, the SFRDs implied at $z > 2$ are much lower than canonical values (even with completeness corrections applied). Karim et al. (2011) adopted the Bell (2003) 1.4 GHz radio SFR calibration (purple circles in Figure 8). This SFR calibration applied to our 3 GHz

stacks gives lower SFRs (purple) than our Molnár et al. (2020) prescription (blue) at $z < 2$, more consistent with the Madau & Dickinson (2014) relation (once completeness corrections are applied), but slightly higher SFRs at $z > 3$. Nevertheless, there is relatively good agreement between the cosmic SFRDs derived from the Bell (2003), Magnelli et al. (2015), and Molnár et al. (2020) calibrations. One particular avenue that we will explore in the future is whether the evolving q_{TIR} prescriptions give an accurate conversion from radio luminosity to SFR. For example, whether or not the total infrared luminosity of a galaxy gives a reliable SFR should depend on stellar mass according to studies of the IR/UV ratios in galaxies out to $z < 5$ (e.g., Bouwens et al. 2016; Fudamoto et al. 2017; Whitaker et al. 2017).

The radio spectral index plays a role in k -corrections, correcting observed 3 GHz to rest-frame 1.4 GHz. Studies such as Tisanić et al. (2018) found that starburst galaxies have spectral steepening at high frequencies ($\nu > 1.4$ GHz). The evolution of the radio–IR relation has been calibrated on bright detected galaxies in our field, but it has not yet been tested for low-mass galaxies. Local studies show that dwarf galaxies are often fainter than expected in radio-continuum emission (e.g., Bell 2003; Leroy et al. 2005; Paladino et al. 2006; Filho et al. 2019), with studies such as Hindson et al. (2018) suggesting

Table 2
Fitted Parameters of Our MS Model (Equation (6)) to All Mass-complete Data for SF Galaxies under Different Assumptions

SFR Calibration	Best-fit Values (s_0, m_0, a_1, a_2)	χ_r^2
Molnár et al. (2020)	$(2.965_{-0.088}^{+0.081}, 11.07_{-0.16}^{+0.15}, 0.215_{-0.012}^{+0.012}, 0.120_{-0.024}^{+0.027})$	6.5
Magnelli et al. (2015)	$(3.20_{-0.10}^{+0.10}, 11.28_{-0.17}^{+0.17}, 0.228_{-0.014}^{+0.015}, 0.125_{-0.025}^{+0.029})$	4.4
Delhaize et al. (2017)	$(2.96_{-0.11}^{+0.10}, 11.29_{-0.17}^{+0.16}, 0.205_{-0.014}^{+0.015}, 0.127_{-0.026}^{+0.030})$	3.6
Davies et al. (2017)	$(2.54_{-0.07}^{+0.07}, 10.94_{-0.15}^{+0.14}, 0.190_{-0.010}^{+0.011}, 0.120_{-0.024}^{+0.028})$	7.2
Bell (2003)	$(3.33_{-0.12}^{+0.11}, 11.28_{-0.18}^{+0.17}, 0.264_{-0.016}^{+0.015}, 0.123_{-0.025}^{+0.027})$	6.4

Note. See Section 3.1 for more information about the different SFR calibrations.

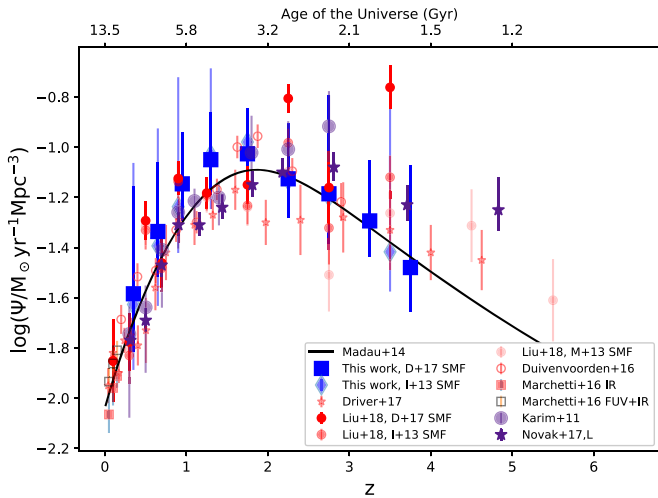


Figure 8. SFR density resulting from integrating the SFR density as a function of stellar mass shown in Figure 7 between $M_* = 10^8$ and $5 \times 10^{12} M_\odot$. Results from this work are shown in blue, results from radio-based observations are shown in purple, and results from IR-based observations are indicated in red.

that the nonthermal synchrotron emission is suppressed. Measuring the radio SED for a range of representative galaxies will be essential to resolving these issues.

Uncertainties involved with fitting functions: calculating the cosmic SFRD involves extrapolation beyond the data, so the shape of the low-mass MS makes a significant difference. For example, repeating our main analysis assuming a fixed low-mass slope of 0.6 and 1.2 (minimal and maximal values reported in the literature) results in a 0.001 dex difference in the cosmic SFRD at $z = 0.35$, but a >0.2 dex difference at $z > 2$, where our sample is not complete below the turnover mass.

Choice of stellar mass function: the size of this effect depends on the low-mass slope of the stellar mass function. To investigate the effect of the stellar mass functions used, we have repeated our main analysis using the Ilbert et al. (2013) stellar mass function, which generally results in slightly lower SFR densities (transparent blue diamonds in Figure 8). The difference in cosmic SFRD is at most 0.09 dex at $z \sim 0.95$.

We also show the cosmic SFRD results from Liu et al. (2018), who constrained the contribution from optically undetected, dusty star-forming galaxies at $z < 6$ in the GOODS-North field. They reported the SFRD obtained using either the Davidzon et al. (2017), Ilbert et al. (2013), or Muzzin et al. (2013; dark red circles to transparent red circles respectively in Figure 8) stellar mass function to correct for incompleteness. The choice of stellar mass function has a large effect on the measured SFRD at $z > 2$, where current IR and radio data are incomplete.

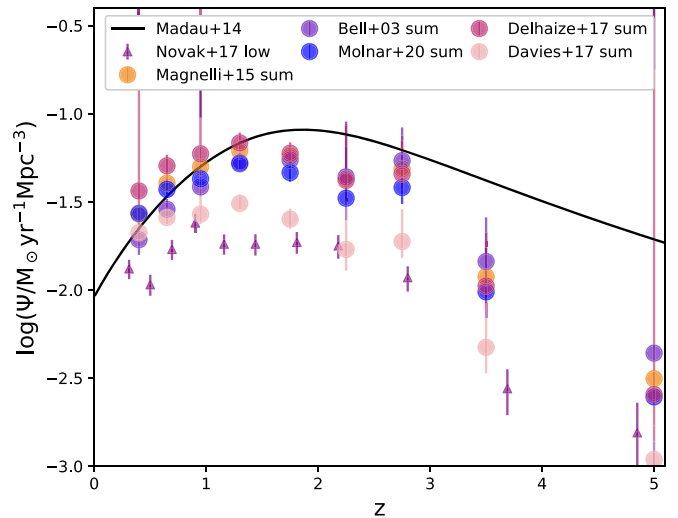


Figure 9. Effect on the cosmic star formation rate density for our galaxy sample caused by assuming a different SFR calibration. Circles represent the total cosmic SFRD inferred by summing the fluxes measured in the mass-complete stacks directly and are not extrapolated to lower mass bins. Purple triangles show the cosmic SFRD inferred from integrating the Novak et al. (2017) luminosity functions over the range covered by the detected sources.

Integration ranges: typically, studies integrate luminosity functions to obtain the cosmic SFR. In our case, we integrate over the cosmic SFRD as a function of mass. Our study is more sensitive to the choice of the low-mass limit of integration rather than the high-mass limit. However, the effect is small: <0.1 dex at both high and low redshifts when changing the low-mass limit of integration from 10^7 to $10^9 M_\odot$.

Scatter of the MS: we correct our cosmic SFRD when calculated by combining the SMF and MS, by a factor that depends on the log-normal dispersion of the MS. Some studies report this scatter to evolve with redshift, finding σ to decrease at high z . Pearson et al. (2018) reported a scatter of only ~ 0.15 dex at $z \sim 4.3$. This would have an impact on our correction (e.g., move $z \sim 4$ SFRD values 0.07 dex relative to the $z \sim 0.4$ value). Observationally, the measured scatter should depend on the SFR indicator chosen. Instantaneous SFR tracers such as nebular emission lines return higher σ than tracers that are sensitive to longer timescales because they are sensitive to rapid variations in the SFHs (Davies et al. 2016, 2019; Caplar & Tacchella 2019). There is also some evidence for a stellar-mass-dependent scatter; for example, see Guo et al. (2013), Ilbert et al. (2015), Popesso et al. (2019a), and Donnari et al. (2019; however, see also Whitaker et al. 2012; Speagle et al. 2014; Tomczak et al. 2016; Pearson et al. 2018).

Other systematic differences: when comparing results with other studies, systematic differences also come from cosmic variance. Some regions in the COSMOS field contain over- or under-densities (e.g., Darvish et al. 2015) that will affect the cosmic

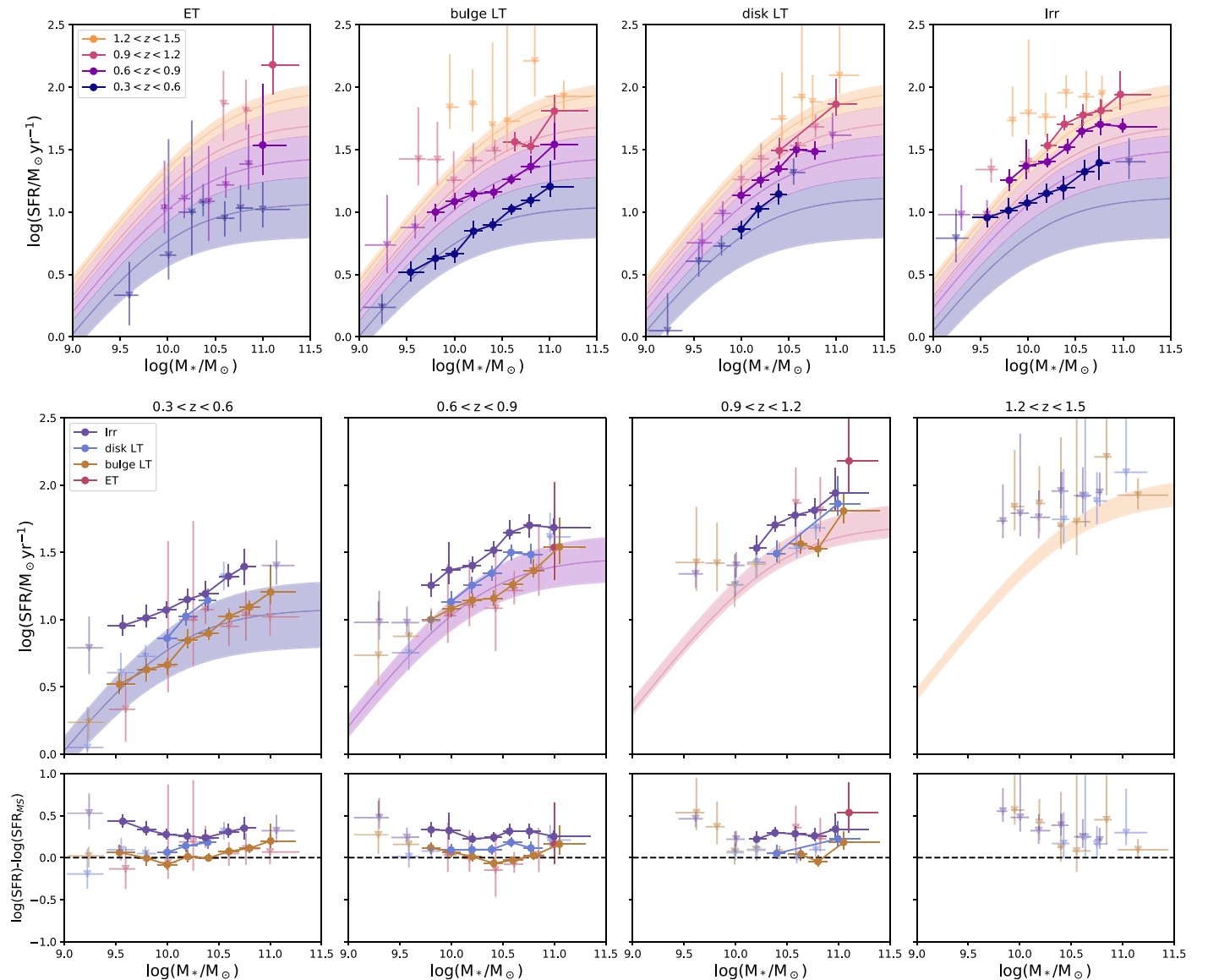


Figure 10. Star-forming galaxy MSs for different morphological types. The top panels show, from left to right, the MSs from a stacking analysis for star-forming galaxies classified as ZEST types 1 (early type), 2.0–2.1 (late type with bulges), 2.2–2.3 (disk-dominated late type), and 3 (irregular). The MS relation determined in Section 4.1 for all star-forming galaxies is shown in the background for comparison. Stacks with $S/N < 10$ are shown as downward-facing triangles because their fluxes are likely overestimated. The middle panels show the four redshift bins separately, allowing for an easy comparison of the SFRs at a fixed stellar mass for the different morphological classes (in particular, see the bottom “residuals” panels, where the average MS from Equation (6) has been subtracted). Disk galaxies (type disk LT) follow a steeper SFR–stellar mass relation than other types, showing no clear evidence for a flattening at high stellar masses. Irregular galaxies have systematically higher SFRs than the other morphological classes.

SFRD because of the decreased or increased number of galaxies compared to the cosmic average (e.g., Madau & Dickinson 2014; Driver et al. 2018). For a survey the size of COSMOS, Moster et al. (2011) finds the relative cosmic variance is $\sim 6\%$ for galaxies with stellar masses $\sim 10^{10} M_{\odot}$ in a redshift slice of $\Delta z = 0.5$. This increases to $\sim 21\%$ for galaxies more massive than $10^{11} M_{\odot}$.

In this section, we have discussed some of the assumptions and systematic uncertainties that go into calculating a cosmic SFRD. These issues need to be resolved in order to use upcoming radio-continuum (and other wavelength) surveys to study both dust-obscured and unobscured star formation across cosmic time.

4.4. Morphology Trends

In this section, we study the MS as a function of galaxy morphology out to $z \sim 1.5$ using HST morphological

measurements in the ZEST catalog (Scarlata et al. 2007) probing rest-frame optical wavelengths (ACS *I* band). It has long been known that the sSFR of a galaxy is anticorrelated with the central mass concentration or the presence of a bulge (e.g., Kauffmann et al. 2003b; Franx et al. 2008; Wuyts et al. 2011; Bell et al. 2012; Bluck et al. 2014; Lang et al. 2014; Whitaker et al. 2015; Parkash et al. 2018; McPartland et al. 2019), but here we show the trends still hold using dust-unbiased radio-continuum sSFRs.

Taken separately, the SFR– M_{*} relations for the different morphological classes appear to follow linear relations but have different slopes and normalizations (Figure 10). We find that massive galaxies dominated by a bulge tend to have lower SFRs at fixed stellar mass and redshift. The lower panels of Figure 10 show that the difference between SFRs of different morphology types becomes prominent at low z ; the sSFR of

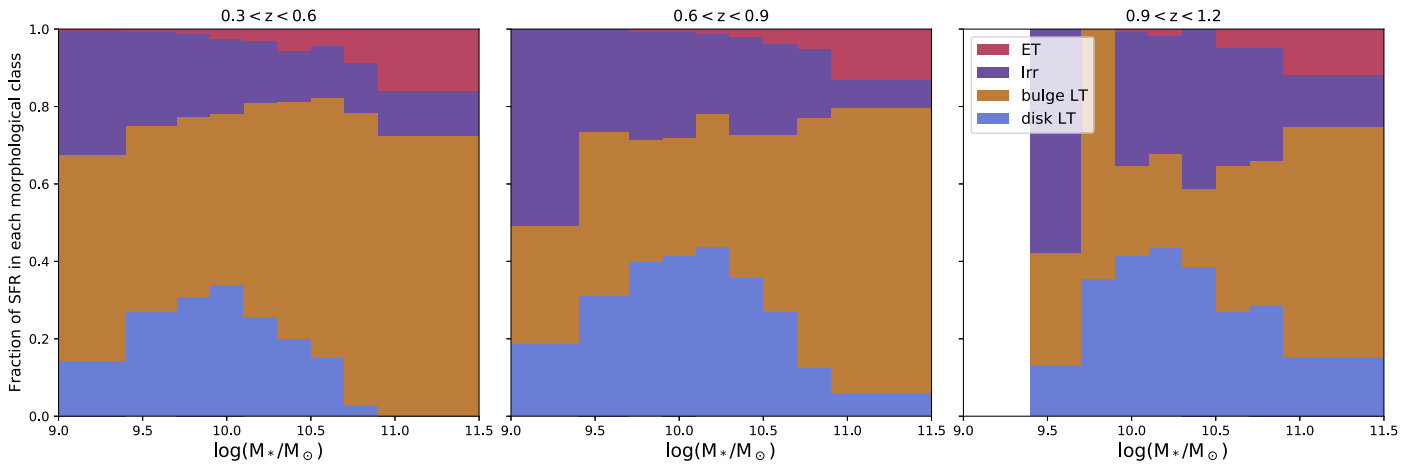


Figure 11. Contributions from different morphological types to the total SFR as a function of mass in three redshift bins. The total SFR is given by multiplying the average from the stack with the number of galaxies in said stack. Only bins mass-complete in all four ZEST types are shown. Results for $1.2 < z < 1.5$ are not shown because all of the fluxes were measured with $S/N < 10$ (see Figure 10). The fractional contribution from disk-dominated galaxies declines as the contribution from bulge-dominated galaxies increases toward lower redshifts.

high-mass, bulge-dominated, and spheroidal galaxies drops faster than the sSFR of disk-dominated galaxies. Disk-dominated star-forming galaxies follow a steeper SFR– M_* relation than other types, particularly at $M_* > 10^{10} M_\odot$ (with slopes of ~ 0.75 compared to ~ 0.5). When the disk-dominated galaxies are combined with the ET and bulge-dominated galaxies, a flattening in the average MS becomes apparent at higher stellar masses, where the ET and bulge-dominated galaxies dominate. Irregular galaxies have SFRs above the MS at all redshifts and are more star-forming than pure disks, at least at $z < 1.2$ and $M_* < 10^{11} M_\odot$.

Figure 11 shows the fraction of the total SFR occurring in galaxies in each morphological class as a function of stellar mass. The fraction of SFR occurring in disk galaxies decreases with redshift as the number of pure-disk galaxies decreases. By $z < 0.6$, there are no pure disks in the most massive bin of star-forming galaxies.²⁷ The fraction of star formation in irregular galaxies is roughly constant at around 20% in the three redshift bins shown but is slightly decreased in favor of galaxies classified as spheroidal for masses $> 10^{11} M_\odot$. Grossi et al. (2018) found that, integrated over all luminosities, pure-disk galaxies contribute significantly more to the cosmic SFRD at $z < 1$ and that the decline in sSFR with redshift is faster for bulge-dominated systems than for pure disks.

Interestingly, the SFR contribution from disk-dominated galaxies in Figure 11 is peaked around $\log(M_*/M_\odot) = 10$ at each redshift. To explain this constant stellar mass, as disk-dominated galaxies have a single power-law MS relation, disk-dominated galaxies should, therefore, have an approximately redshift-independent stellar mass function shape to $z < 1$. Indeed, Pannella et al. (2009b) also found that the stellar mass function of disk-dominated galaxies in the COSMOS field is consistent with being constant with redshift out to $z \approx 1.2$. However, we note that only the shape needs to be constant for the SFR contribution from disk galaxies to be peaked at the same stellar mass, not the normalization.

²⁷ Based on the volume probed in this redshift bin and the way pure-disk galaxies have been defined, this is not inconsistent with SDSS studies that do find massive $M_* > 10^{11} M_\odot$ pure-disk galaxies at $z \sim 0.1$ (Ogle et al. 2016; Thanjavur et al. 2016).

In this section, we have used the q_{IR} from Molnár et al. (2020) to calculate SFR from radio luminosity. More tests (e.g., including UV emission) need to be done to ensure we can recover the correct SFR in galaxies of different morphological types given that the infrared–radio correlation (Molnár et al. 2018) and perhaps radio spectral index (Gürkan et al. 2018) vary between them.

To summarize, we find the flattening of the high-mass slope can be, in part, explained by the inclusion of massive bulge-dominated galaxies, which follow a shallower SFR– M_* relation than disk-dominated galaxies. As bulges grow more prominent in the low-redshift galaxy population (especially at large stellar masses), the flattening of the main sequence becomes more significant. We discuss these results further in Section 5.3.

4.5. Environmental Trends

Scoville et al. (2013) found that the median SFR of galaxies in the COSMOS field is not dependent on their environment at $z > 0.8$, while at lower redshift the median SFR in the highest densities is almost 1 dex lower than the SFR in low-density environments. Figures 12 and 13 show the MS for SF galaxies in different environments. Using the local density as probed by the number of galaxies per Mpc^3 normalized by the mean number in each redshift slice (Scoville et al. 2013), we look for variations in sSFR within four local density bins: $-1.5 < \delta < -0.15$, $-0.15 < \delta < 0.15$, $0.15 < \delta < 4$, and $4 < \delta < 80$ (where -1.5 Mpc^{-2} and 80 Mpc^{-2} are the minimum and maximum values in the catalog). These very roughly trace void, field, filament and group, and cluster environments (Paulino-Afonso et al. 2019). Figure 12 shows no statistically significant difference between the MS relations for galaxies in different local densities. The same is true when considering “all” galaxies, shown in the appendix. In the bottom panel of Figure 12, the difference between the SFRs (normalized to the MS for all star-forming galaxies) is shown in each redshift bin. Duivenvoorden et al. (2016) found that the (IR) SFR decreases (by < 0.2 dex) with local density out to $z < 2$ in the COSMOS field. However, both of our results have large uncertainties, and the decreasing trend reported by Duivenvoorden et al. (2016) was only significant at

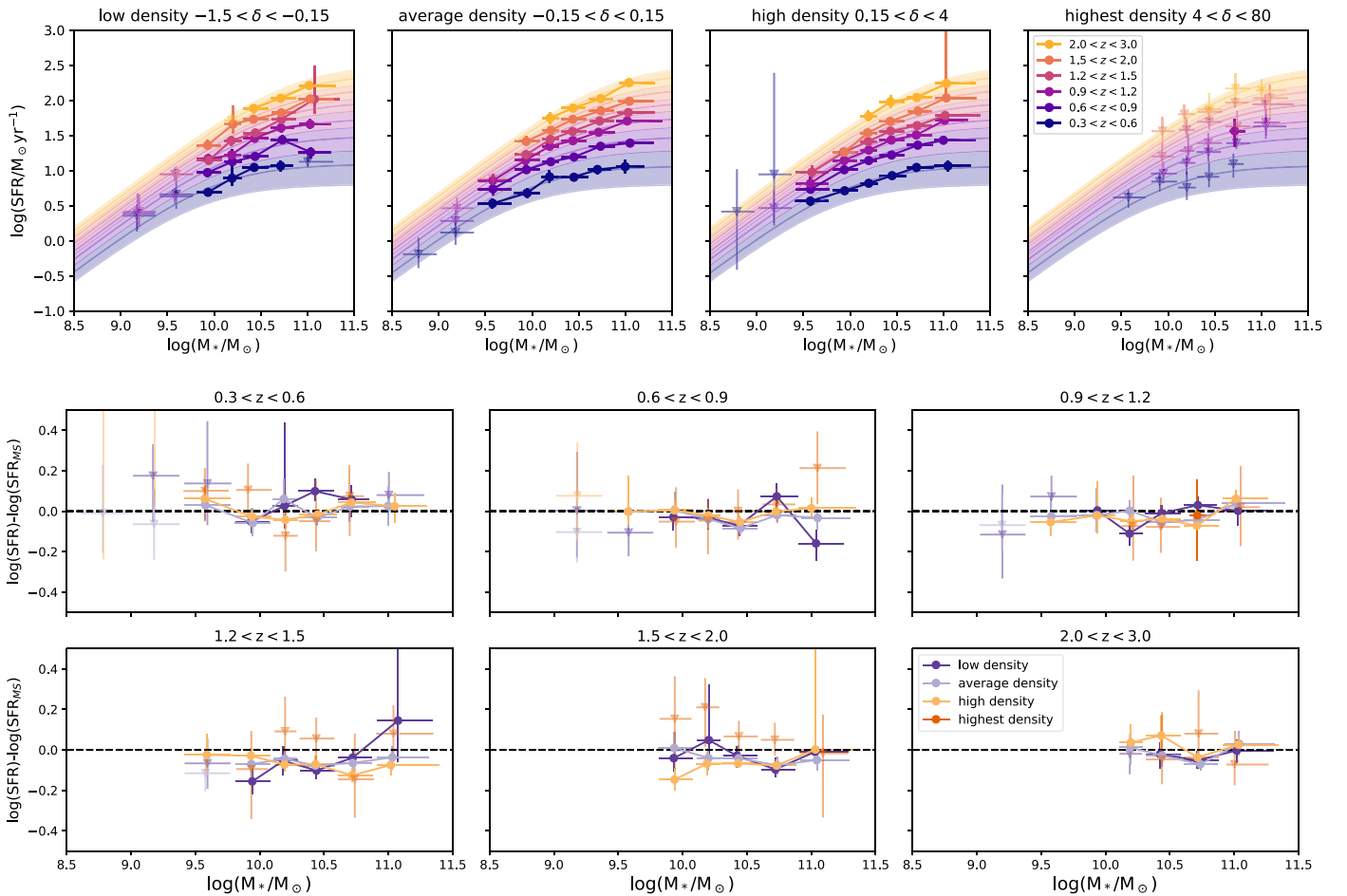


Figure 12. Effect of local number density on the MS. The top panels show SFR as a function of stellar mass for star-forming galaxies in different local densities (as defined by Scoville et al. 2013) out to $z \sim 3$. The relationship between sSFR and M_* remains constant over these different local densities (explained in Section 4.5), from galaxies in underdense regions (left) to galaxies in overdense regions (right). Our best-fit relation for all SF galaxies is shown in the background, and no panel shows significant deviations from this relation. Data with $S/N < 10$ are shown as downward-facing triangles as their fluxes are likely overestimated. The last two rows show the difference between the SFRs of star-forming galaxies compared to the average MS in different local environments for different redshifts.

$1.5 < z < 2$. The completeness-corrected total cosmic SFRD from Duivenvoorden et al. (2016) is shown in Figure 8 and is consistent with our SFRD at $z \sim 2$.

Figure 13 shows the MS for SF galaxies in X-ray groups at $0.64 < z < 0.88$ where the statistics are robust. The best-fitting MS determined in Section 4.1 is shaded in the background. We only show SFRs derived for stellar-mass-complete bins. When the stacked 3 GHz image has $S_p/\text{rms} > 10$, the SFR is shown as a solid square; the SFR is shown as a downward-facing triangle otherwise.

We find no significant difference in the SFRs of star-forming galaxies in X-ray groups (halo mass $12.5 < \log(M_{200c}/M_\odot) < 14.5$) compared to star-forming galaxies in the field, consistent with our findings above that used local galaxy number density as a probe for the environment. However, the scatter is very large, and larger samples will be required to confirm this result. When we focus on the three most massive X-ray groups (which we refer to as clusters, with halo masses $14 < \log(M_{200c}/M_\odot) < 14.5$), there is an enhancement of the SFR of intermediate-mass $10.0 < \log(M_*/M_\odot) < 10.5$ members compared to the field. However, there are only four to seven galaxies per bin when considering only the clusters at $0.64 < z < 0.78$, so this result is not reliable. That being said, at higher redshifts, starburst galaxies could preferentially lie in

denser regions, consistent with the observed clustering of bright Herschel sources (Cooray et al. 2010; Amblard et al. 2011; Viero et al. 2013) and luminous blue galaxies at $z \sim 1$ (Cooper et al. 2006).

Using ancillary data from the COSMOS field, we find that the galaxy environment probed by X-ray groups, clusters, and local galaxy number density has little effect on the shape of the radio-derived MS at $z > 0.3$. This could indicate that environmental quenching (e.g., gas strangulation or stripping) is not effective at these redshifts, or that the colors redden before the SFR is suppressed, resulting in the affected galaxy being classified as quiescent and not being included in the MS analysis. However, we also find no significant trends when including all galaxies, which points to the former scenario being most likely.

5. Discussion

5.1. Comparisons with Literature

In Figure 14, we show the difference between a selection of literature determinations of the MS for star-forming galaxies and the 3 GHz-determined MS we found in Section 4.1. Variations of up to ± 0.4 dex occur, and results are particularly divergent at low and high stellar masses, where the effects of

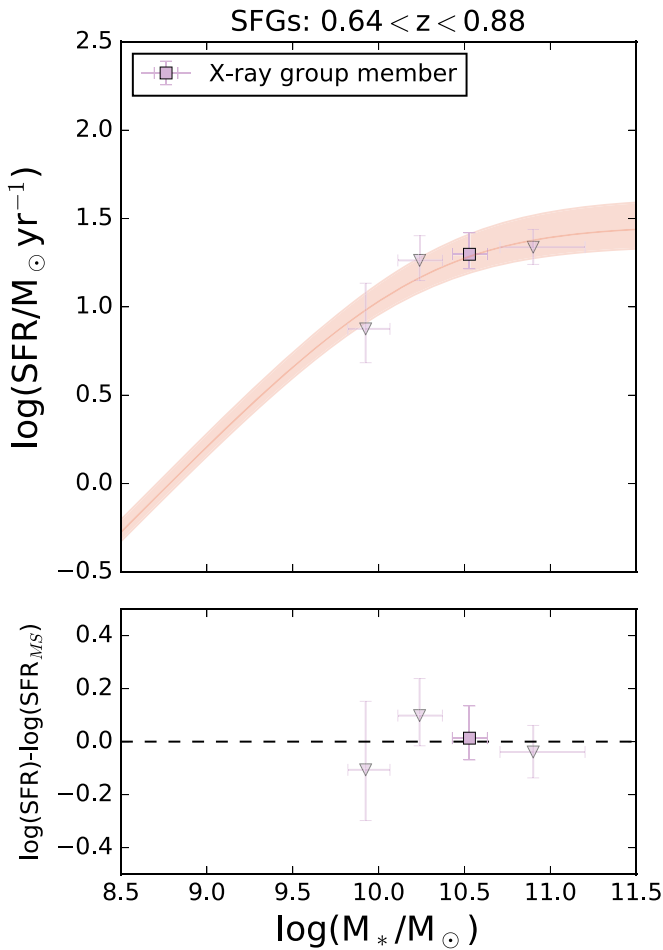


Figure 13. SFR–stellar mass relation for galaxies residing in X-ray groups and clusters at $z \sim 0.76$ (top panel). The background curve shows the corresponding SFR– M_* relation (Equation (6)). The bottom panel shows the difference in the SFRs of galaxies in X-ray groups and the model MS. Stacks with $S/N < 10$ are shown as downward-facing triangles because their fluxes are likely overestimated.

completeness and star-forming sample selection become most important, respectively. We give more information about the studies included and show the differences in literature studies at six redshift bins, out to $z = 4.5$, in Appendix D. Our stacking analysis probes stellar masses up to 0.5 dex below that of Schreiber et al. (2015). In general, our SFRs tend to be higher than measured by other studies, but given the large sample-to-sample variation present and the fact that different SFRs are sensitive to different stellar populations, we do not consider this to be an important shortcoming of our analysis.²⁸ But, as shown by simulations in Appendix A.3, we are not able to well reproduce sample averages using median stacking. In addition to observations showing large discrepancies in the MS, when compared at $z = 0$, different simulations also have an MS whose amplitude varies by up to 0.7 dex between studies, and the power-law slopes range from 0.7 to 1.2 (Hahn et al. 2019). Observationally, the different indicators used either to define the MS location or to estimate the SFR, combined with galaxy sample selection effects, can cause the large variations between

²⁸ We note that our MS derived from median SFRs is in slightly better agreement with the literature at $z \sim 1$ because the median SFR can be ~ 0.04 dex below the mean. However, our MS derived from median fluxes still lies at the extrema of the literature.

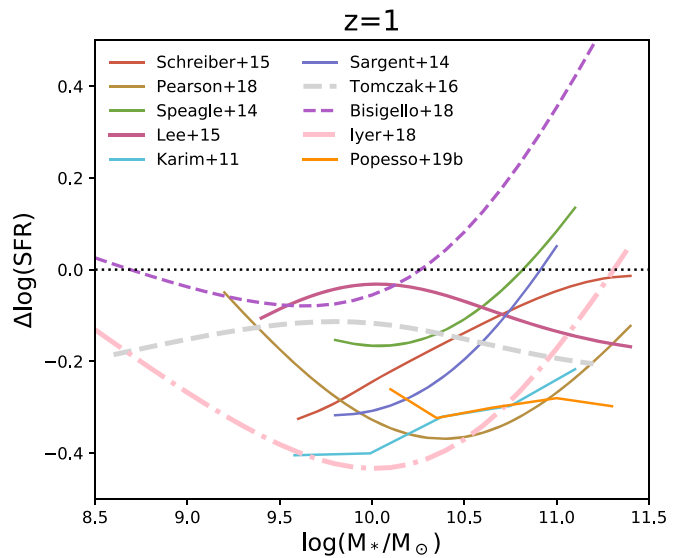


Figure 14. Comparison with literature MS relations at $z = 1$. $\Delta \log(\text{sSFR})$ is the ratio of the MS SFR from the literature relative to the MS SFR from this work (Equation (6)). The dotted line at $\Delta \log(\text{SFR}) = 0$ indicates where the relations agree. For more redshift bins, see Figure D1.

studies (Popesso et al. 2019a) and will be discussed in this section.

The scatter of the MS increases toward higher masses (Guo et al. 2013; Davies et al. 2019; Popesso et al. 2019a, 2019b; although see, e.g., Rodighiero et al. 2010; Schreiber et al. 2015), which can complicate the MS determination at the massive end ($\log(M_*/M_\odot) \sim 11$). Studies such as Whitaker et al. (2014) find strong evolution in the slope for more massive galaxies, evolving from 0.6 at $z = 2$ to 0.3 at $z = 1$. But other studies such as Popesso et al. (2019b) and Karim et al. (2011) indicate no slope evolution. Discrepancies between SFR tracers also tend to be largest at $\log(M_*/M_\odot) > 10.5$ (e.g., Katsianis et al. 2020). Here, where the scatter is large and not normally distributed, defining the location of the MS as the mean, median, or mode of the SFR distribution can have an important impact. Also, the decision to model the whole galaxy population or only SF galaxies and whether SF galaxies are selected by color or an sSFR threshold have an important impact on the determined MS at high masses. To summarize, the MS is not well defined at $\log(M_*/M_\odot) \sim 11$.

Most discrepancies in the MS can be explained by the different SFR tracers used by different studies (Katsianis et al. 2020). Studies that use IR SFRs often find a turnover in the MS at $z < 2$, whereas studies using optical and SED tracers tend to find a linear MS (see Appendix D). Recently, Pearson et al. (2018) used SED (UV to $160 \mu\text{m}$) priors to deblend the Herschel SPIRE maps and overcome the limitations of confusion in measuring SFRs in the COSMOS field. Pearson et al. (2018) report no evidence for a high-mass MS flattening. The SED SFRs obtained with CIGALE (Code Investigating GALaxy Emission; Burgarella et al. 2005) are ~ 0.4 dex lower than the SFRs obtained by combining UV and IR SFRs, the latter of which has been a standard method since introduced in the MS study by Wuyts et al. (2011). Schreiber et al. (2015) used UV + IR SFRs in a stacking analysis in the COSMOS and GOODS fields to push to deeper IR luminosities, and they reported a high-mass turnover that vanishes by $z \sim 2$ (confirmed by Schreiber et al. 2017, who found a simple

linear MS relation at $z \sim 4$ from ALMA-derived SFRs). Both Pearson et al. (2018) and Schreiber et al. (2015; as well as Lee et al. 2015) used the same Herschel data in the same fields, and yet these studies resulted in different interpretations. In general, for more robust results, uncertainties specific to each data set and from the sample selection could be better understood using simulated observations, and systematic uncertainties from stellar mass and SFR derivations should be analyzed. Such analysis has begun; for example, see Davies et al. (2019; observations) and Katsianis et al. (2020; simulations). Using the SKIRT full 3D radiative transfer postprocessing of the EAGLE simulations by Camps et al. (2018), Katsianis et al. (2020) found that methods relying on IR wavelengths have SFRs that systematically exceed the intrinsic relation by 0.2–0.5 dex. They suggest this may be due to contamination of the IR luminosity from dust that is heated by an evolved stellar population rather than by newly born stars, particularly in the outskirts of EAGLE+SKIRT galaxies. This effect is also found in observations of local galaxies (e.g., Helou et al. 2000; Bendo et al. 2015). Because the 3 GHz SFR calibration used in our work was anchored to local infrared data, this could explain why our SFRs are higher than some of the literature, and by extension, why our cosmic SFRD lies above the Madau & Dickinson (2014) curve.

5.2. Cosmic SFRD Evolution and Characteristic Stellar Mass

The overall normalization of our SFR density, seen in Figure 8, lies $\lesssim 0.15$ dex above what is expected from the literature (e.g., Madau & Dickinson 2014) at $z < 3$.

Our SFR density–stellar mass relationship (Figure 7) shows a peak at a characteristic stellar mass of $M_* \sim 10^{9.9} M_\odot$ at $z \sim 0.35$ and a characteristic mass that increases with redshift out to $z \sim 2.5$ ($M_* \sim 10^{10.6} M_\odot$). This trend was also predicted by Béthermin et al. (2013), who showed that the majority (90%) of the star formation activity is hosted in halo masses of $11.5 < \log(M_h/M_\odot) < 13$ regardless of redshift.²⁹ However, halos that have a mass of $10^{11.5} < M_h < 10^{13.5} M_\odot$ at $z > 4.7$ will become massive clusters with halo masses $M_h > 10^{14.5}$ by $z = 0$. Similarly, halos in the characteristic halo mass range at $0.5 < z < 3.7$ will become small clusters or groups by $z = 0$, while at $z < 0.5$, the SFR density peaks in Milky Way–like halos (Béthermin et al. 2013). In the empirical model of Béthermin et al. (2013), the bulk of cosmic star formation initially occurs in the progenitors of the most massive halos before becoming less efficient and propagating to less massive halos, a trend referred to as “downsizing” (Cowie et al. 1996; see also, e.g., Tinsley 1968).

Similarly, Legrand et al. (2018) studied the stellar-to-halo mass relationship in the COSMOS field using a parametric abundance matching technique and find that the ratio peaks at a characteristic halo mass of $\sim 10^{12} M_\odot$ at $z = 0.2$, and that this characteristic mass increases with redshift to $z \sim 2.3$ and then remains flat until $z = 4$ (see also, e.g., Leauthaud et al. 2012; Moster et al. 2010). They argue that this is consistent with the picture that star formation is quenched in more massive halos first. Below the characteristic halo mass, the stellar mass build-up (i.e., SFR) “keeps up” with the dark matter accretion rate, whereas above the characteristic mass the galaxy is more likely

to be quenched. Interestingly, Mowla et al. (2019) found that the galaxy size–stellar mass relation has a broken power-law shape, whose slope changes at a pivot mass that also increases with redshift in the same manner as the peak of the stellar-to-halo mass relation from Leauthaud et al. (2012). We interpret the evolution in turnover mass or characteristic mass toward $z = 0$ to support the idea that quenching starts in the most massive galaxies at high redshift, and then proceeds to lower-mass galaxies with time.

5.3. Morphology Trends

We found in Section 4.4 that for massive galaxies ($\log(M_*/M_\odot) > 10.0$), galaxy morphology is correlated to the position on the MS: at a fixed stellar mass, early-type and bulge-dominated galaxies have lower SFRs than disk-dominated galaxies, which in turn have lower SFRs than irregular galaxies.

Galaxy interactions could account for irregular morphologies and also cause a burst of star formation, resulting in irregular-type galaxies lying above the MS of disk-dominated galaxies. Cibinel et al. (2019) reported that the starburst population across redshifts $0.2 < z < 2$ predominantly consists of late-stage mergers. We note that the slope of the SFR–stellar mass relation for these irregular galaxies is slightly shallower than for the disks, inconsistent with results from Bisigello et al. (2018) for starburst galaxies. To further investigate the composition of our ZEST-classified irregular (type 3) galaxies, we cross-matched our parent sample using the Capak et al. (2007) position coordinates with the $70 \mu\text{m}$ selected catalog of 1503 sources from Kartaltepe et al. (2010a, 2010b), finding 1142 overlapping sources. Out of the ~ 2300 irregular ZEST sources, we found 216 with visual morphological classifications in Kartaltepe et al. (2010b). The authors classified source morphology (e.g., spiral, elliptical) and noted whether each source was undergoing a minor or major merger. We found that for galaxies in both the ZEST and $70 \mu\text{m}$ catalogs, 23.6% are minor mergers and 28.8% are major mergers (total 52.5% mergers). For irregular ZEST galaxies, the fraction of mergers is much higher, at 80% (30.1% minor mergers and 50% major mergers). This supports the idea that our ZEST type 3 irregular galaxies have higher star formation rates (and more irregular morphologies) than the disk-dominated subsample because they are undergoing mergers that trigger gas inflows, resulting in an enhanced SFR (Barnes & Hernquist 1996).

One key result from our work is that bulge-dominated galaxies follow a shallower MS relation than disk-dominated galaxies. Trends between sSFR and morphology have also been found in spiral galaxies, which are presumably not merger driven. For example, Parkash et al. (2018) found that earlier-type spiral galaxies (Sa) have lower sSFRs than later-type spirals (Sc). Schreiber et al. (2016) performed bulge–disk decompositions of galaxies with $\log(M_*/M_\odot) > 10.2$ in CANDELS and found that the disk component of galaxies at $z = 1$ follows a flattening of the MS that is similar to the total (stacked) population, even for disk-dominated galaxies, in disagreement with our results. They also reported that the lower sSFRs of massive galaxies correspond to lower star formation efficiencies (not present at $z = 2$) rather than lower gas fractions. However, the study used Herschel data to also infer the gas content, which should be confirmed with independent observations. Although Schreiber et al. (2016) found that disk-dominated galaxies exhibit the same flattening as

²⁹ Indeed, many studies have found that halos more massive than $\sim 10^{12} M_\odot$ can be quenched by the shock heating of the cold inflowing gas, e.g., Dekel & Birnboim (2006, 2008), Birnboim et al. (2007), Faucher-Giguère et al. (2011).

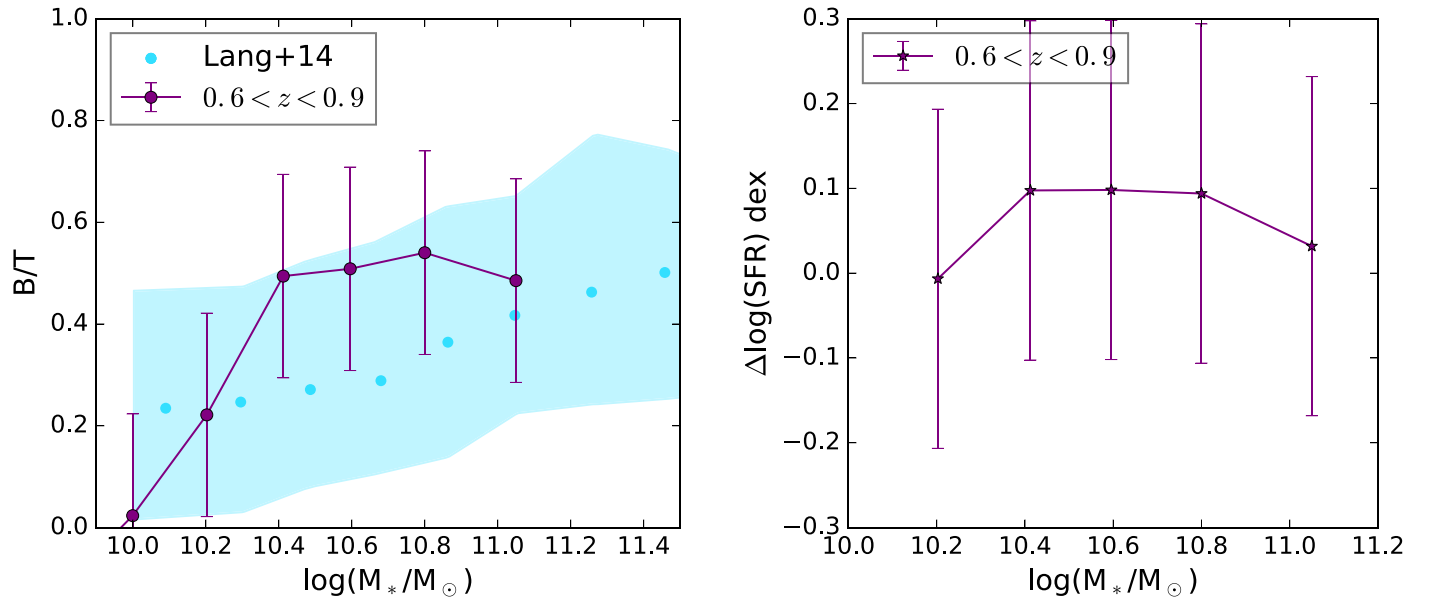


Figure 15. Do bulges suppress SFR? The left panel shows the typical bulge-to-total ratio of our bulge-dominated late-type galaxies required to explain their measured sSFR, assuming they consist of a disk component that follows the same SFR– M_* relation as the disk-dominated galaxies, and a bulge that has no star formation (providing a lower limit to the B/T). We fix the error on our B/T ratio to 0.2, which comes from the range of the B/T ratios obtained by repeating this method for disk-dominated galaxies (which should have returned zeros). The B/T ratios inferred in this way are consistent with those measured by decompositions of the stellar mass by Lang et al. (2014) at $0.5 < z < 2.5$ (cyan dots indicate median measured B/T , and the shaded region shows the range of values). The right panel shows the amount of star formation activity that needs to be suppressed in the disk in order to recover the SFR– M_* relation for the bulge-dominated galaxies if the bulge-dominated galaxies have B/T ratios observed by Lang et al. (2014) and bulges that have no star formation. Our results set an upper limit for the morphological SFR suppression in bulge-dominated galaxies, if any, to be less than 0.2–0.3 dex.

bulge-dominated galaxies, other studies such as Erfanianfar et al. (2016) found that the disk galaxies have a more linear MS relation than the bulge-dominated galaxies, consistent with our findings. The number of pure disks at high stellar mass is very low in the low-redshift universe (Ogle et al. 2016); our lowest redshift bin $0.3 < z < 0.6$ contains only four disk-dominated galaxies above $10^{10.7} M_\odot$. Larger samples at low redshifts, such as those provided by SDSS, have shown that the disk component of galaxies follows a linear MS (Abramson et al. 2014).

We explore how the steeper MS of disk-dominated galaxies can be related to the shallower MS for bulge-dominated galaxies at a fixed redshift in Figure 15. We infer how much stellar mass (assumed to be in a quiescent bulge) must be added to the disk-dominated galaxies to shift the SFR– M_* relation to be consistent with that of the bulge-dominated late-type galaxies. First, we fit a linear relation to the disk-dominated galaxies and compute the disk mass required to provide the SFR observed for the bulge-dominated galaxies. We then infer the bulge-to-disk ratio assuming that the bulge-dominated galaxies consist of a disk (following the MS of disk-dominated galaxies) plus a bulge with zero star formation activity. This assumption will give a lower limit to the B/T ratio, as bulges can conceivably contribute a small amount of star formation activity. These resulting B/T ratios are shown in Figure 15 for $0.6 < z < 0.9$, where we have the most robust results. The resulting SFR-derived B/T (bulge mass to total mass) ratios show a clear increase with stellar mass and values consistent with the result from Lang et al. (2014) for star-forming (sSFR selected) galaxies in the CANDELS/3D-HST fields.

If we adopt the B/T ratios given by the Lang et al. (2014) measurements, then the amount of SFR that needs to be suppressed in the disk is shown in the right-hand panel of Figure 15 as a function of total galaxy mass. In other words, we

calculate the difference between the expected SFR of the disk components based on the linear fits to the disk-galaxy MS and the measured average SFR of the bulge-dominated galaxies. The amount of inferred SFR suppression is consistent with zero, implying that the disks of bulge-dominated systems with a non-star-forming bulge have sSFRs similar to pure disks. The same result was also recovered when we compared stacks of ZEST type 2.3 (pure disks) and ZEST type 2.1 (2.0 is more likely contaminated by early-type galaxies).

We note that if the bulge component also contains any star formation activity, then a trend toward SFR suppression in the disk component could be stronger and that the $\Delta \log(\text{SFR})$ values in Figure 15 are lower limits. There is also the possibility that our SFR calibrations based on the infrared–radio correlation should be different for different galaxy types (Molnár et al. 2018). If we use a 3 GHz–SFR calibration for our disk-dominated galaxies based on the $q_{\text{TIR}}(z)$ relation reported by Molnár et al. (2018) for disk-dominated galaxies and use their spheroidal-galaxy $q_{\text{TIR}}(z)$ values for the bulge-dominated galaxy SFR, then our inferred suppression $\Delta \log(\text{SFR})$ would increase by ~ 0.1 dex. Again, our result (calculated using the same Molnár et al. 2020 calibration for all galaxies) can be considered as a lower limit for the effect of bulges.

Studies such as Poppo et al. (2019a) and Schreiber et al. (2016) have reported that the presence of bulges alone is not sufficient to explain the flattening of the MS at very high masses; in addition to the increased mass given by a bulge component, there is also an indication for a decrease in star formation activity of the disks along the MS. Theoretical arguments suggested by Meidt et al. (2018) explain that the gravitational potential of a centrally concentrated bulge can help stabilize the gas against fragmenting (see also simulations from Su et al. 2018 and Gensior et al. 2020). Bulges can also decrease the strength of bars, thereby decreasing the efficiency

at which gas is funneled into the galaxy center (Barazza et al. 2008; Fragkoudi et al. 2016). Popesso et al. (2019a) speculated that while the quiescence of the bulge component could be explained by supermassive black hole feedback, the lower SFR of the disk at high masses could be due to gas starvation induced by gravitational heating in massive halos. However, we find that a quiescent bulge is sufficient to explain the decrease in SFR along the MS for SF galaxies. Nevertheless, larger sample sizes and a better understanding of SFR calibrations will be required to get the uncertainties on B/T ratios and sSFR suppression to within ~ 0.2 dex, the amount of influence that morphological suppression due to the presence of a bulge is expected to have on the sSFR.

5.4. Environmental Trends

The literature tends to agree that higher density environments increase the fraction of quiescent (red) galaxies, and we do see this in the COSMOS field (see top right panel of Figure E4; Peng et al. 2010; McGee et al. 2011; Scoville et al. 2013; Darvish et al. 2014, 2016). Whether or not the normalization of the MS (defined for star-forming galaxies) depends on galaxy environment is still under debate, but many studies identify no variations of MS with environments such as clusters and voids; for example, see Tyler et al. (2013, 2014), Koyama et al. (2014), Ricciardelli et al. (2014), Grossi et al. (2018), Paulino-Afonso et al. (2019), and Pharo et al. (2020; although see Duivenvoorden et al. 2016, who found a difference at $1.5 < z < 2$ in COSMOS). However, at low redshift ($z < 0.3$), studies have reported a clear dependence of the MS on the galaxy environment (e.g., von der Linden et al. 2010; Haines et al. 2013; Paccagnella et al. 2016; Gu et al. 2018). Studies such as Balogh et al. (1998, 2002), Couch et al. (2001), and Gómez et al. (2003) have found that SFRs of cluster galaxies were lower relative to field galaxies of similar bulge-to-disk ratio and luminosity, which suggests the decrease in star formation may not be fully explained by the density–morphology relation (Dressler 1980) alone. Environmental effects appear important at low redshift, where spatially resolved studies show that environmental quenching works on galaxies outside-in (e.g., Schaefer et al. 2019).

Recently, Old et al. (2020) showed that environmental suppression of SFR, relative to the MS, indeed becomes more important toward low redshift ($z < 1$) and lower stellar masses. However, the amount of suppression was only a factor of 1.4 (3.3σ significance). It is not surprising that our COSMOS sample does not show clear evidence for an environmental dependence of the sSFR when probing local galaxy number density at $z > 0.3$, or in X-ray groups at $0.64 < z < 0.88$. In simulations, Matthee & Schaye (2019) found that star-forming satellite galaxies only account for ≈ 0.04 dex of the scatter in the MS, indicating that satellite-specific processes are either weak or strong and rapid (such that the satellites quickly drop out of the sample of star-forming galaxies), consistent with our results. In the local universe, $z < 0.3$, there is evidence for both slow ($\sim 2\text{--}4$ Gyr; e.g., strangulation) and rapid (e.g., stripping of cold gas) quenching processes associated with the galaxy environment (Paccagnella et al. 2016; Maier et al. 2019).

Unlike our results, recent work by Rodríguez-Muñoz et al. (2019) found that not only is the fraction of star-forming galaxies lower³⁰ in X-ray group environments by a factor of

~ 2 , but also the star-forming galaxies in groups have an average sSFR ~ 0.3 dex lower than the field across all redshift ranges probed ($0.1 < z < 0.9$; they have a redshift bin $0.60 < z < 0.89$, similar to ours, which consists of two clusters). One might also expect the resolution of the photometry and SFR tracer to have a significant impact on environmental studies because source blending can be an issue if not properly taken into account. Larger cosmological volumes should be probed to understand the importance of the environment on the average sSFR of galaxies.

Erfanianfar et al. (2016) separated group and field environments for two redshift bins ($0.15 < z < 0.5$, $0.5 < z < 1.1$) and found at $z < 0.5$ that group and cluster galaxies have a reduction in SFR compared to their counterparts in the field (with a larger fraction of disks being redder). They also report that the flattening of the MS for field galaxies is due to an increased fraction of bulge-dominated galaxies at high masses and that the associated quenching process must already be in place before $z \sim 1$. Tomczak et al. (2019) and Koyama et al. (2013) found that SF galaxies show a difference of, at most, 0.2 dex in sSFR in dense environments as compared to the field from $z = 0.4$ to $z = 2$.

Once a group or cluster is in gravitational equilibrium, the increased local density should decrease the timescales involved in evolution compared to the relevant timescales in the field because of the larger gravitational potential. Indeed, Popesso et al. (2015) shows that the cosmic SFR activity declines faster (toward $z = 0$) in group size halos than in the field. This faster evolution increases the scatter around the MS and could decrease the average SFR when including all galaxies. To summarize, the local density affects the speed of the star formation evolution more than the mode (altering the MS) of evolution (at least for $0.3 < z < 3$).

6. Conclusion

Radio-continuum emission is a useful dust-unbiased star formation tracer, and stacking is an effective way to push current stellar mass limits achievable through direct detections. We have mean-stacked 3 GHz images for galaxies in the latest COSMOS photometric catalogs (Laigle et al. 2016; Davidzon et al. 2017) to measure the average dust-unbiased SFR for galaxies as a function of stellar mass, redshift, environment, and morphology. Our findings can be summarized as follows:

1. We find that star-forming galaxies follow an SFR– M_* relation that is steeper at low masses than at high masses (i.e., a flattening is present). We model the MS relation for star-forming galaxies (and all galaxies) with a new function that allows (if needed) for the flattening to occur at increasing stellar mass and for the increase in overall normalization with redshift.
2. The cosmic star formation rate density peaked at $1.5 < z < 2$, but the measurements still contain large systematics such as SFR calibrations and the necessity of assuming a stellar mass function to account for incompleteness.
3. Our results support the downsizing scenario, that massive galaxies are formed and quenched first. At higher redshift, more massive galaxies contributed more to the cosmic SFR density than at lower redshift, consistent with literature findings. This result is driven by the increasing turnover mass with redshift in our MS.

³⁰ We find that the fraction of SF galaxies is lower in X-ray environments by a factor that depends on stellar mass, but is generally < 2 ; see Figure E4.

4. We find no significant difference in the MS for star-forming galaxies located in different environments probed by the local number density, or by X-ray group membership.
5. Early-type galaxies have the lowest SFRs at a fixed stellar mass, followed by bulge-dominated galaxies, disk-dominated galaxies, and irregulars. We find this to be the case at $z < 1.5$.
6. Massive bulge-dominated galaxies follow a shallower $\text{SFR}-M_*$ relation than disk-dominated galaxies. As the number of bulge-dominated galaxies increases toward low redshift, the contribution of disk-dominated galaxies to the total SFR occurring declines, particularly at high stellar mass. This increase in bulge-dominated galaxies could be related to the mechanisms responsible for downsizing or mass quenching.
7. Combining samples of bulge-dominated galaxies and disk-dominated galaxies can explain, in part, the flattening of the MS observed to occur at low redshifts and high stellar masses.

The decrease in the cosmic SFRD from $z \sim 2$ to $z \sim 0$ is caused by a combination of the decrease in the sSFR of star-forming galaxies and the quenching of star-forming galaxies (e.g., Renzini 2016). The decrease in the sSFR of star-forming galaxies since $z \sim 2$ is likely due to the decrease in cold gas accretion. Quenching transforms star-forming galaxies into quiescent galaxies and is likely driven by feedback (stellar and AGN), environmental effects, or morphological quenching. With the latest COSMOS data, we see a mass dependence in this decrease of the MS (a flattening at high stellar mass that shifts to lower masses at low z). We also found that the stellar mass in which most new stars are formed (a characteristic mass) increases with redshift. The increasing characteristic mass with redshift and the evolving flattening in the MS correspond to bulge formation and a decline in SFR in massive galaxies. The mechanism that reduces the SFR proceeds to be effective at lower stellar masses toward the present epoch. Our results on the sSFR of galaxies with different morphological types could imply that the presence of a bulge affects the star formation process. However, future observations are required to confirm these conclusions and to determine whether the gas in bulge-dominated galaxies is stabilized against fragmentation or is not present to form stars (either it has been removed by feedback, or cold gas is no longer able to be accreted onto the galaxy disk).

We would like to thank the anonymous referee for their careful comments that lead to a highly improved paper. We would like to thank D. Molnar and K. Cooke for helpful discussions and feedback. S.L. acknowledges funding from Deutsche Forschungsgemeinschaft (DFG) Grant BE 1837/13-1 r. E.S., D.L., and P.L. acknowledge funding from the European Research Council (ERC) under the European Union’s Horizon 2020 research and innovation program (grant agreement No. 694343). V.S. and M.N. acknowledge the European Union’s Seventh Framework program under grant agreement 337595 (CoSMass). B.G. acknowledges the support of the Australian Research Council as the recipient of a Future Fellowship (FT140101202). Y.P. acknowledges the National Key R&D Program of China, Grant 2016YFA0400702 and NSFC grant Nos. 11773001, 11721303, 11991052. This publication has received funding from the European Union’s Horizon 2020

research and innovation program under grant agreement No. 730562 [RadioNet]. S.L. would like to thank L. Kewley and ASTRO3D for providing the excellent conditions at Bateman’s Bay writing retreat, during which part of this manuscript was prepared.

Facilities: this work is based on data products from observations made with ESO Telescopes at the La Silla Paranal Observatory under ESO program ID 179.A-2005 and on data products produced by TERAPIX and the Cambridge Astronomy Survey Unit on behalf of the UltraVISTA consortium. This work is based on observations obtained with XMM-Newton, an ESA science mission with instruments and contributions directly funded by ESA Member States and NASA. The National Radio Astronomy Observatory is a facility of the National Science Foundation operated under cooperative agreement by Associated Universities, Inc.

Software: Figure 5 made use of the CORNER Python package (Foreman-Mackey 2016). This research has made use of NASA’s Astrophysics Data System. This research has made use of the NASA/IPAC Infrared Science Archive, which is operated by the Jet Propulsion Laboratory, California Institute of Technology, under contract with the National Aeronautics and Space Administration. This research made use of NumPy (Van Der Walt et al. 2011). This research made use of matplotlib, a Python library for publication-quality graphics (Hunter 2007). This research made use of ds9, a tool for data visualization supported by the Chandra X-ray Science Center (CXC) and the High Energy Astrophysics Science Archive Center (HEASARC) with support from the JWST Mission office at the Space Telescope Science Institute for 3D visualization. This research made use of Astropy, a community-developed core Python package for Astronomy (Astropy Collaboration et al. 2013). This research made use of TOPCAT, an interactive graphical viewer and editor for tabular data (Taylor 2005).

Appendix A Stacking Analysis: Details and Tests

In this section, we discuss some of the issues concerning the stacking of radio images, in particular, the choice of method to measure total flux, and the choice of whether to represent the average as the mean or the median.

Radio images with bright sources must be cleaned to have any hope of detecting sources among the side lobes of the bright source. For this reason, most stacking analysis to date has been performed on cleaned radio images. Components of sources that lie above the clean threshold will have a point-spread function (PSF) corresponding to the Gaussian-shaped clean beam, whereas fainter sources with no cleaned components will have a PSF corresponding to the dirty beam. Stacking a population that includes sources with different PSFs is not an intuitive situation. For the VLA 3 GHz LP, the entire map was cleaned down to 5σ and further down to 1.5σ using tight masks around 5σ sources (Smolčić et al. 2017b). The noise level in each pointing was around $4\text{--}5 \mu\text{Jy beam}^{-1}$. In addition, each pointing was tapered with a Gaussian to achieve a circular clean beam with $0''.75$ FWHM. However, the sizes vary across the COSMOS field because of different uv coverage (with a difference between the major and minor axis being at most 3%), so even for “clean sources” there is no “single PSF.” We have tested further cleaning of our stacks (after averaging in the image plane) with the mean beam shape,

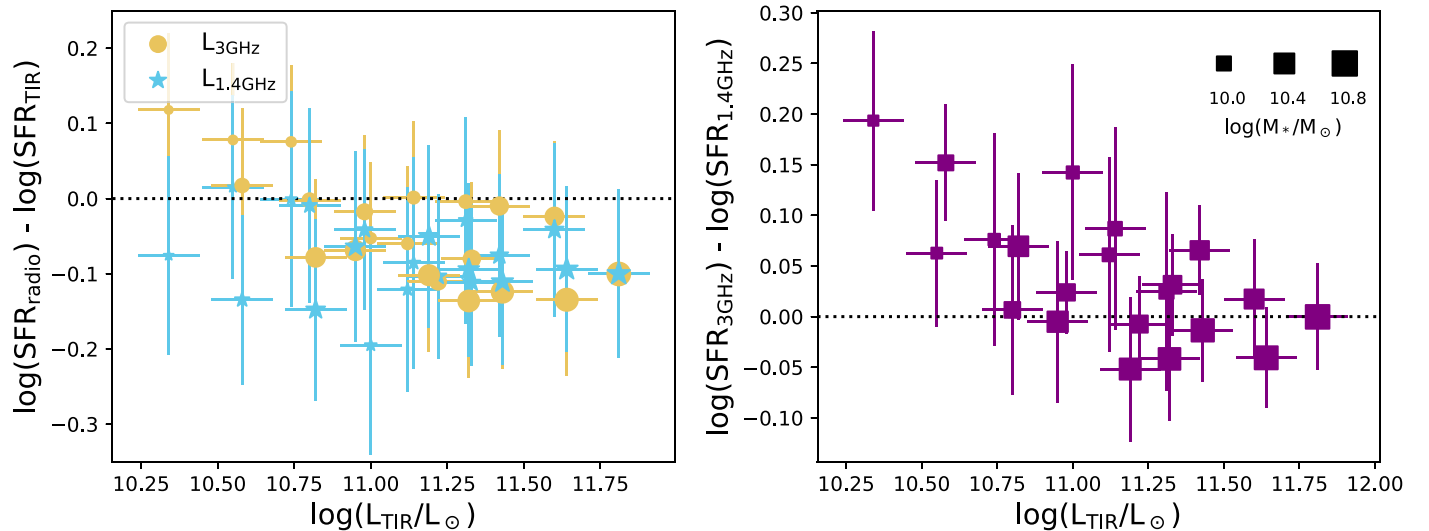


Figure A1. Comparison of 1.4 GHz, 3 GHz, and TIR-derived SFRs from median-stacked images of star-forming galaxies at $z < 2$. The left panel shows radio SFRs compared to IR SFR. The 1.4 GHz fluxes are from Karim et al. (2011). The right panel shows the difference between 1.4 and 3 GHz SFRs as a function of IR luminosity. In both panels, the symbol size represents the average mass of stacked galaxies.

but this tended to remove flux from the already cleaned sources, rather than adding back flux from the side lobes. One way to minimize this could be to stack sources below 1.5σ and then clean the resulting stack, but this would have to be done separately for the 192 different VLA pointings, due to variations in the dirty beam across the field, resulting in a loss of S/N. We note that every source will have some residual dirty flux; for example, a source detected at 5σ , if it was included in the clean masks, will have 30% of its flux “dirty” (below 1.5σ). This percentage will go down for higher S/N sources but be 100% for noncataloged sources.

Studies such as Mao et al. (2011) with similar numbers of detections and nondetections in each bin combine detected and nondetected sources separately, weighing the flux from each detected source by $1/N$ and the stack of undetected sources as n/N , where N is the total number of sources in the bin and n is the number of sources in the stack. There is a significant variation in the fraction of sources detected at $>5\sigma$ between stellar mass and redshift bins, ranging from 0% to 30% from low to high stellar masses. We decided to treat all sources homogeneously by stacking detected and nondetected sources together, thereby not introducing an arbitrary flux limit above which we consider a source detected. This uniform treatment also has the advantage of allowing errors to be readily calculated by bootstrapping methods.

In the region selected for this analysis, the rms variation is minimal (e.g., rms variations on scales of $\sim 1'$ are less than 2%, Smolčić et al. 2017b), and we found no difference in our mean or median stacked image fluxes by weighting each cutout by its inverse variance.

A.1. Flux Measurement: Comparison with 1.4 GHz and IR Stacks

In Section 3, we mentioned that astrometric uncertainties and intrinsic source extent require us to measure a total flux rather than the flux contained within one beam around the central object. For our source fluxes, we adopt a simple elliptical 2D Gaussian fitting. We input initial conditions for the fit using the

peak flux from the stacking routine and the beam size and find best-fit parameters using `OPTIMIZE.CURVE_FIT`. The fitting procedure was tested allowing for nonzero background values on cataloged and simulated sources. We found background fluxes were always $< 1 \mu\text{Jy}/\text{beam}$, so we have adopted the fits with no background subtraction for our analysis.

We have measured total fluxes of 3 GHz stacks that were created using the input SF galaxy sample of Karim et al. (2011), allowing us to compare our results with their published median-stacked 1.4 GHz fluxes. To be consistent with Karim et al. (2011), we show results from median stacking in our comparison (Figure A1). We have also stacked these sources at infrared wavelengths following Magnelli et al. (2015) and derived a (median) FIR luminosity for the stacks. We chose to focus on $z < 2$, where all samples are reliable, and stellar masses $> 10^{10.0} M_\odot$ for completeness. For our comparison, we have converted radio fluxes to infrared luminosities assuming a spectral index of -0.7 and the radio–infrared correlation of Molnár et al. (2020). Figure A1 shows the difference between the 3 GHz, 1.4 GHz, and IR SFRs. All stacks shown have $S_p/\text{rms} > 10$ at 3 GHz. The 1.4 and 3 GHz SFRs measured from Gaussian fits to determine the total fluxes agree within 0.2 dex, as illustrated in Figure A1. For the low-mass galaxies ($\log(M_*/M_\odot) \approx 10.0$), the scatter is larger, in part due to the lower S/N in the 1.4 GHz stack. However, we also cannot rule out a stellar mass-dependent radio spectral index from causing the 3 GHz derived SFRs to be higher than the 1.4 GHz SFRs at low IR luminosities.

A.2. Mean or Median

While the mean of a flux distribution is natural to interpret mathematically, it can be sensitive to outliers. Because the median is robust to the presence of outliers, it has the advantage that all data can be used. However, the median value recovered from a stacked image depends not only on the underlying distribution but also on the noise level. White et al. (2007) showed that in the limit where the individual sources are well below the rms level, the median values trace the population

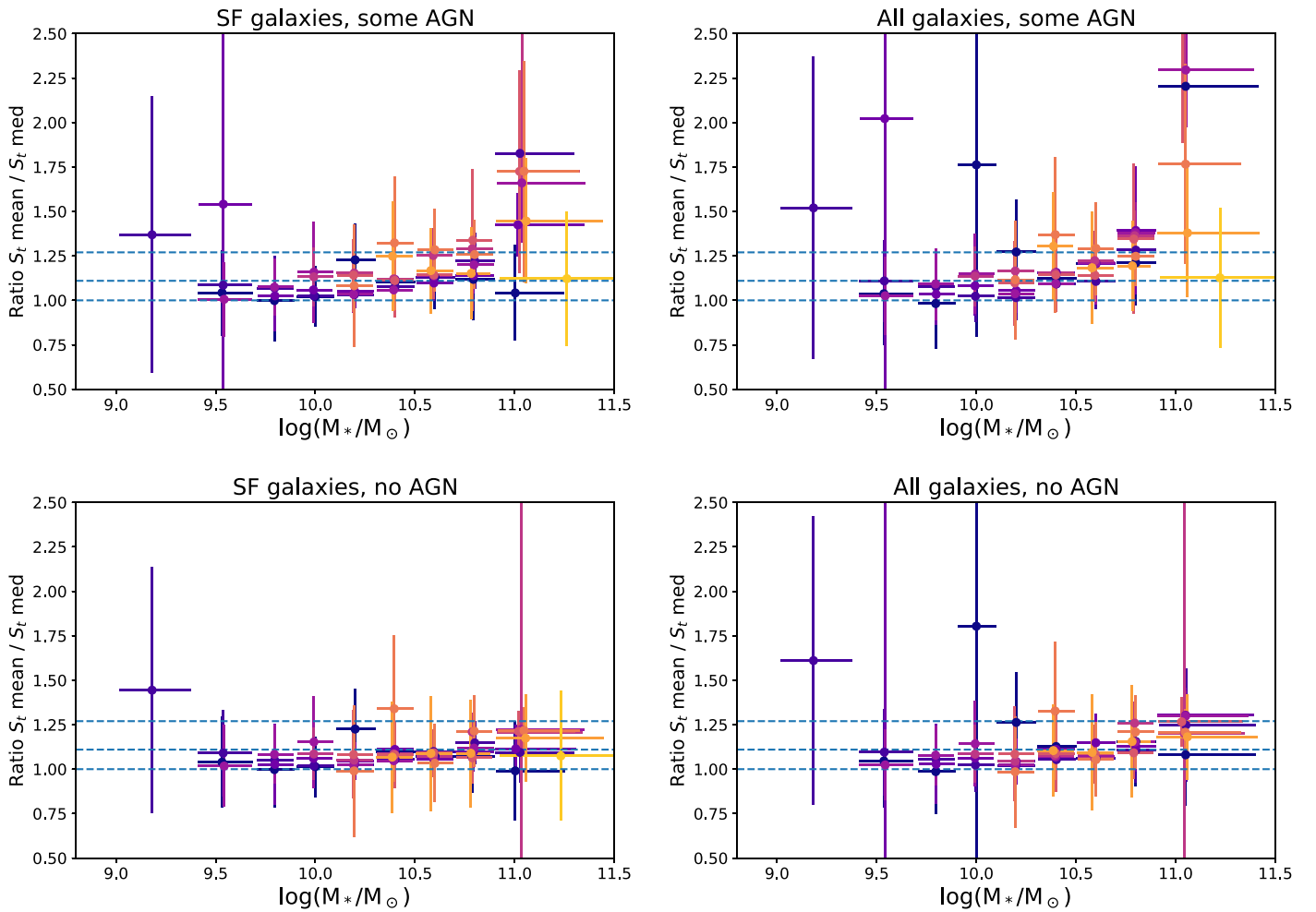


Figure A2. Ratio of total fluxes derived from mean and median stacked images as a function of the median stellar mass. Left panels show SF galaxies selected by $NUVrJ$ colors. Right panels show all galaxies. Top panels show results with only multicomponent radio AGNs removed. Bottom panels show the results using our sample with multiwavelength AGN removal applied. Color represents redshift (purple to yellow is low to high redshift using the same scale as, e.g., Figures 4 and B1). Error bars represent the 5%–95% range. Horizontal lines are drawn at $S_{t,\text{mean}}/S_{t,\text{median}} = 1.0, 1.11, 1.27$, which correspond to the values expected if SFR is symmetrically distributed, or if $\log(\text{SFR})$ is normally distributed with $\sigma = 0.2$ or $\sigma = 0.3$ dex, respectively (and if flux is linearly related to SFR). Only stacks with $S_p/\text{rms} > 10$ are shown. Radio emission of AGN-host galaxies is dominated by the AGN emission, making them outliers affecting the mean-to-median ratio. The MS dispersion is consistent with 0.2 dex.

means. These arguments only strictly apply to point sources. The underlying distribution of source fluxes is also not likely a simple Gaussian,³¹ thus leaving us with a difficult problem that deserves more attention.

Figure A2 shows the ratio of total fluxes derived from the mean and median stacking analysis. In all cases, the mean reported is larger than the median, which is expected for most SFR distributions. In particular, for a Gaussian distribution in $\log(\text{SFR})$, with a given σ , the ratio between the mean SFR and the SFR corresponding to the median $\log(\text{SFR})$ (i.e., the peak of the Gaussian) is $e^{2.652\sigma^2}$. We find that the ratio of $S_{\text{mean}}/S_{\text{med}}$ increases with stellar mass; this is mostly due to the presence of AGN outliers affecting the mean fluxes. The bottom panels show the results when AGNs are excluded, as done for our main analysis. Here, when considering all galaxies, there seems to be a residual trend of increasing ratio (scatter) with stellar mass even once AGNs are removed. On one hand, radio-AGN

removal in passive galaxies is complicated, but on the other hand, there are likely more quenched galaxies with low SFRs at high masses included in the full sample, which would increase the measured scatter.

The uncertainties of the median fluxes from our bootstrapping analysis are smaller than the uncertainties on the mean because the median is more robust to the presence of outliers or interloping sources. In Figure A3, we show five example images resulting from our stacking analysis, with mean stacks on the top panels and median stacks shown at the bottom.

Mean SFRs follow a less-smooth MS relation than the median SFRs, with higher SFRs at low masses ($\log(M_*/M_\odot) < 9.5$) and high masses ($\log(M_*/M_\odot) > 11$). However, our simulations indicate that our fluxes are more robust for mean stacks than median stacks (see next section).

A.3. Realistic Galaxy Simulations

We adopted a realistic mock galaxy Monte Carlo simulation to test the reliability of our stacking method. Following the

³¹ The distribution of galaxies in SFR at a fixed M_* and z is thought to consist of two or three components (Bisigello et al. 2018; Hahn et al. 2019) that could be log-normal (or not; Eales et al. 2018b).

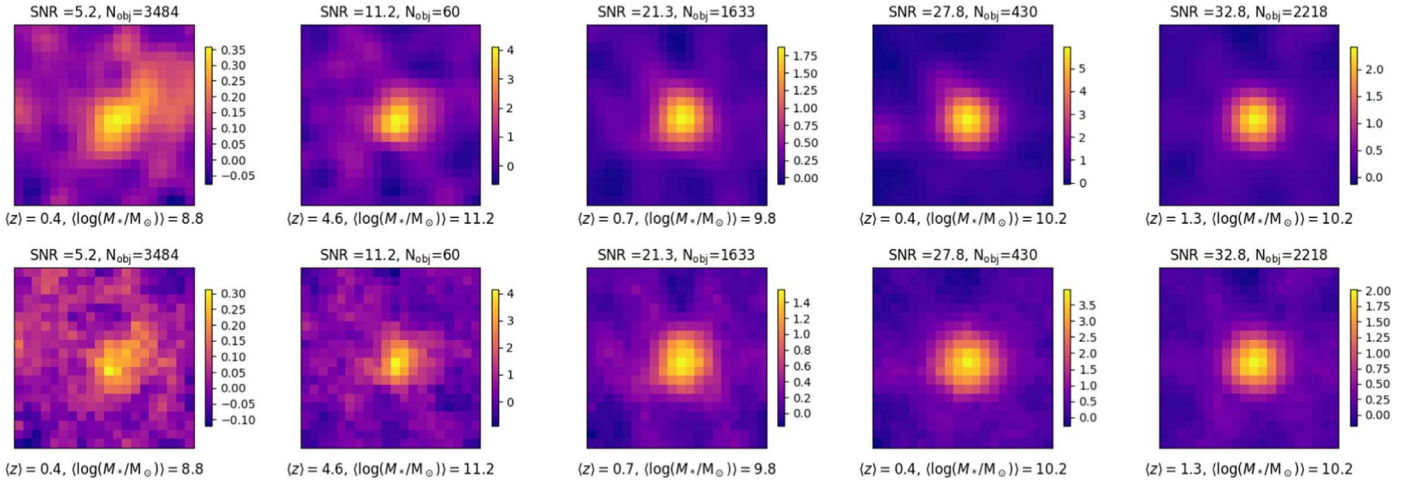


Figure A3. Some example 3 GHz stacks. The top row shows the mean stack, and the bottom row shows the median stack for the same image. The peak flux/rms ratio for the median stacks is given as the S/N and increases from left to right. For our analysis, the left-most stack (low mass) would be excluded because the fluxes tend to be overestimated for low-S/N sources (see Figure A4).

method of Liu et al. (2019a), we generate mock galaxies within the VLA-COSMOS survey area ($\sim 1.55 \text{ deg}^2$) that obey the observed galaxy stellar mass functions (down to $10^8 M_\odot$) and an MS correlation at each redshift from 0 to 10 (31 redshift bins). The simulation has three steps: (1) generating a mock galaxy catalog with redshift, stellar mass, SFR, and coordinate properties; (2) assigning galaxy sizes and radio 3 GHz fluxes; and (3) making a simulated radio 3 GHz image. We then repeated our analysis procedure using the generated mock galaxy catalog and simulated 3 GHz image; here we focus on our results from stacking and measuring fluxes.

In the first step, we loop over redshift bins and construct a star-forming galaxy stellar mass function (as shown in Figure 23 of Liu et al. 2019b) to compute the number of star-forming galaxies in each stellar mass bin. Then we do a Monte Carlo procedure to generate the redshifts and stellar masses of the corresponding number of galaxies in each stellar mass and redshift bin. By adopting an MS, we then generate log-normal distributions of SFRs for galaxies in each stellar mass bin.³² The spatial coordinates of the mock galaxies are assigned in the same way as in Liu et al. (2019a), that is, inserting into the simulation area but avoiding being too close ($0''.7$) to real galaxies (Laigle et al. 2016).

In the second step, the assigned SFR for each galaxy was converted to an IR luminosity and then to a radio luminosity following Molnár et al. (2020): $q_{\text{TIR}} = -0.155 \times \log L_{1.4 \text{ GHz}} + 5.96$. Rest-frame 1.4 GHz luminosities were converted to observed 3 GHz luminosities using a spectral index of -0.7 .

The galaxies were modeled as Gaussian sources with sizes depending on their redshifts and stellar masses following (extrapolating from) van der Wel et al. (2014). We also took into account that dust sizes and radio sizes are observed to be a factor of about 2 smaller than the optical size (e.g., Fudamoto et al. 2017; Bondi et al. 2018; Jiménez-Andrade et al. 2019). A random minor/major axis ratio from 0.2 to 1 was assigned to each source.

These model galaxies are then convolved with a Gaussian with an FWHM of $0''.75$ to emulate the observations with the VLA LP beam. Our mock catalog tests have been restricted to using Gaussian sources, and thus effects related to differences between the CLEAN and dirty beam are neglected. This effect is described at the beginning of this section, but quantifying this effect is beyond the scope of this paper. In the last step, we first create a noise image by taking the rms values from Smolčić et al. (2017b) and generating normal distribution pixel values across the field. Then we insert galaxies as Gaussian shapes into the noise image.

We tested our flux measurement method on individual galaxies and the stacks of simulated galaxies. According to our simulations, the fluxes for stacks with a low $S_p/\text{rms} > 10$ (S/N) are overestimated, as shown in Figure A4. For our analysis, we use a cut of $S_p/\text{rms} > 10$, where we can recover mean fluxes to within $\sim 10\%$. In the bottom panels of Figure A4, we compare the median stacked fluxes with the median and mean fluxes from the input catalog. The resulting fractional errors are higher than for the mean fluxes, with the median flux from the stack being biased high. Because the bias in the median fluxes is a complicated function of both S/N and source size, there was no simple cut we could make to be confident in the fluxes from the median stacks (Figure A4). Therefore, we have adopted the mean fluxes for our main analysis. We do, however, include MS fitting results using SFRs derived from median fluxes (which are systematically lower than our mean SFRs) in Table C2.

A.4. Comparison with Novak et al. (2017)

As a consistency check, we test whether our model of the MS given in Equation (6), with best-fit parameters for star-forming galaxies, can reproduce the luminosity functions of Novak et al. (2017). This test involves generating a mock galaxy catalog using the stellar mass functions of SF galaxies from Peng et al. (2010) and Davidzon et al. (2017). We assign SFRs following a log-normal distribution with the mean from our MS model and scatter = 0.29 dex (Popesso et al. 2019a) to mock sources in bins of redshift and stellar mass as described in Appendix A.3.

³² For our test, no starburst or quiescent galaxies were included. The input MS prescription and scatter of the log-normal were kept hidden until after the analysis was complete, to minimize researcher bias.

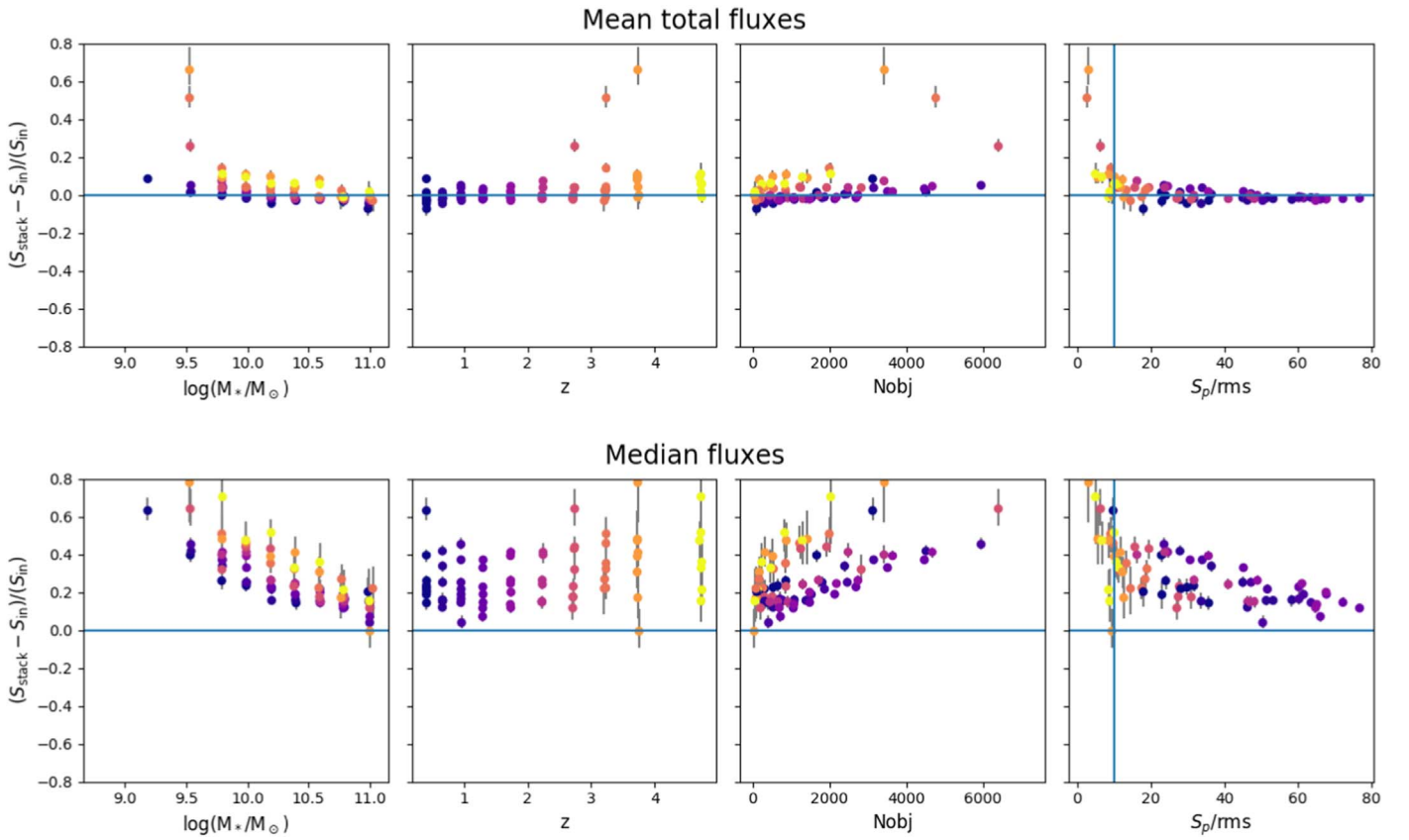


Figure A4. Results from stacking simulated galaxies. From left to right, fractional error on the total flux recovered from mean stacking as a function of stellar mass, redshift, number of sources, and S/N (S_p/rms). In bins of stellar mass and redshift, we compare in the top panels the mean of the input galaxy 3 GHz total fluxes with the total flux measured from the stacked cutout of those sources. Bottom panels show the comparison of the median fluxes. The y-axis represents the fractional error on the fluxes. A blue vertical line in the last panel is drawn at $S/N = 10$. Data are colored by redshift (see the second panel).

We calculate radio luminosity functions from our mock sources and, in Figure A5, compare them to the 1.4 GHz luminosity functions of Novak et al. (2017) derived using the ~ 6000 radio sources without radio excess (SF galaxies) in the 3 GHz LP. Novak et al. (2017) fixed the faint and bright end shape of the radio luminosity function to the local values. The redshift bins used by Novak et al. (2017) are displayed in Figure A5.

The luminosity functions generated by our mock sources agree well with the Novak et al. (2017) luminosity functions,

where both our MS and the Novak et al. (2017) luminosity functions are constrained (i.e., the orange squares match the blue histograms at $0.3 < z < 4.7$).

In Figure A6 we show the SFR– M_* relation for SF galaxies listed in the Smolčić et al. (2017b) catalog. The horizontal dashed lines show the 5σ flux limit converted to an SFR at the limits of the redshift range shown. From this, it is clear that to constrain the MS from the 3 GHz LP, we must include sources below the detection threshold, for example, via a stacking analysis.

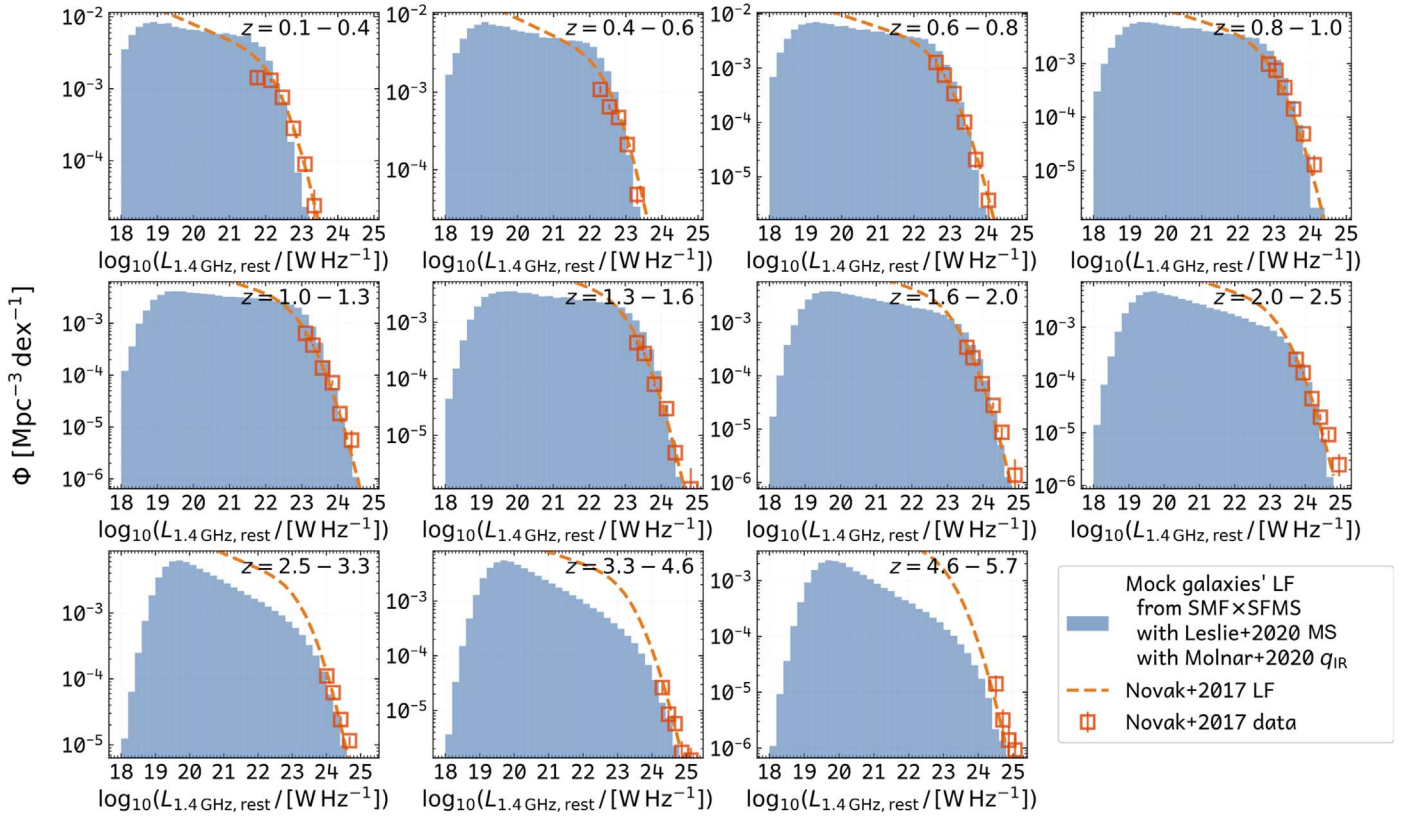


Figure A5. Luminosity functions generated from our MS model, compared with radio luminosity functions measured using the 3 GHz LP detections by Novak et al. (2017). Our mock sources, derived by combining the MS from Equation (6) and the SMF in the COSMOS field, agree well with the luminosity functions from Novak et al. (2017), where they are constrained by detected sources (orange squares).

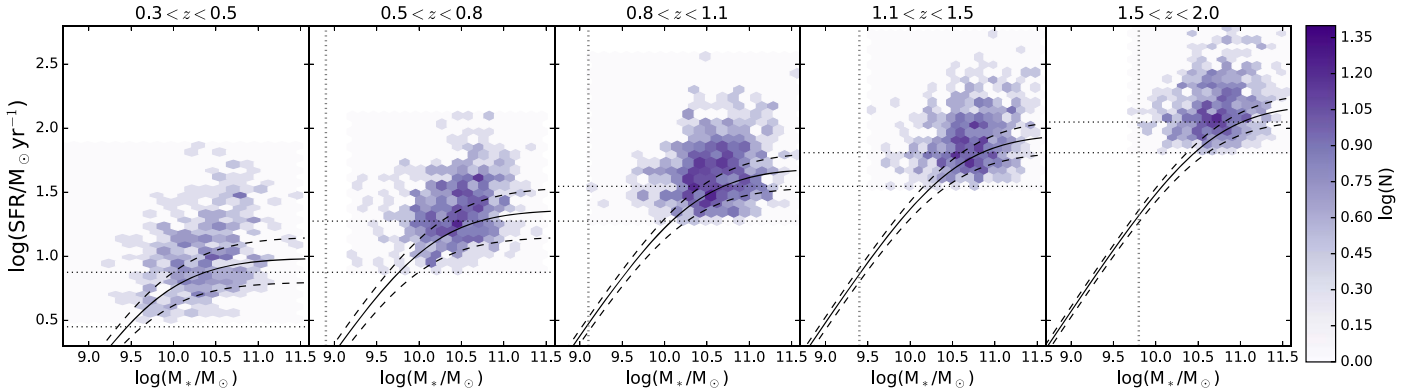


Figure A6. MS for COSMOS2015 galaxies detected in the 5σ VLA 3 GHz catalog and classified as pure SF galaxies. The solid line shows the best-fit MS at the midpoint of the redshift bin displayed, with the dashed lines showing the MS evolution between the bounds of the redshift bin. The color shows the number of galaxies in each hex bin. Vertical dotted lines show the mass-completeness limit for this redshift. Horizontal dotted lines show the 5σ 3 GHz flux limit converted to an SFR at the lowest and highest redshift in the bin. This flux cut limits the direct detections to galaxies that lie above the MS.

Appendix B Selection Effects

B.1. Selecting Star-forming Galaxies

The selections used in constructing the parent sample affect the resulting MS. Studies without a cut to separate star-forming and quiescent galaxies (e.g., Sobral et al. 2014) show reduced MS slopes because the quiescent galaxies “contaminate” the highest mass bins across a wide range of redshift. Using stricter SF selections results in a straighter or steeper MS (e.g., Karim et al. 2011; Johnston et al. 2015). In Figure B1, we compare the

difference between two commonly used color-color cuts from the literature, the *UVJ* and *NUVrJ* selections. Color-color cuts are empirical criteria based on the number density of galaxies in these 2D planes. The *UVJ* selection uses the redshift-dependent rest-frame *U-V*, *V-J* color-color cuts described in Whitaker et al. (2011). The number density of galaxies in the COSMOS field on the *NUVrJ* diagrams can be seen in Laigle et al. (2016).

The resulting SFR- M_* relations are consistent between the two selections within the uncertainties except for our lowest redshift bin ($0.3 < z < 0.5$) and at the highest masses, where the *UVJ* color cut selects galaxies with a higher mean SFR as

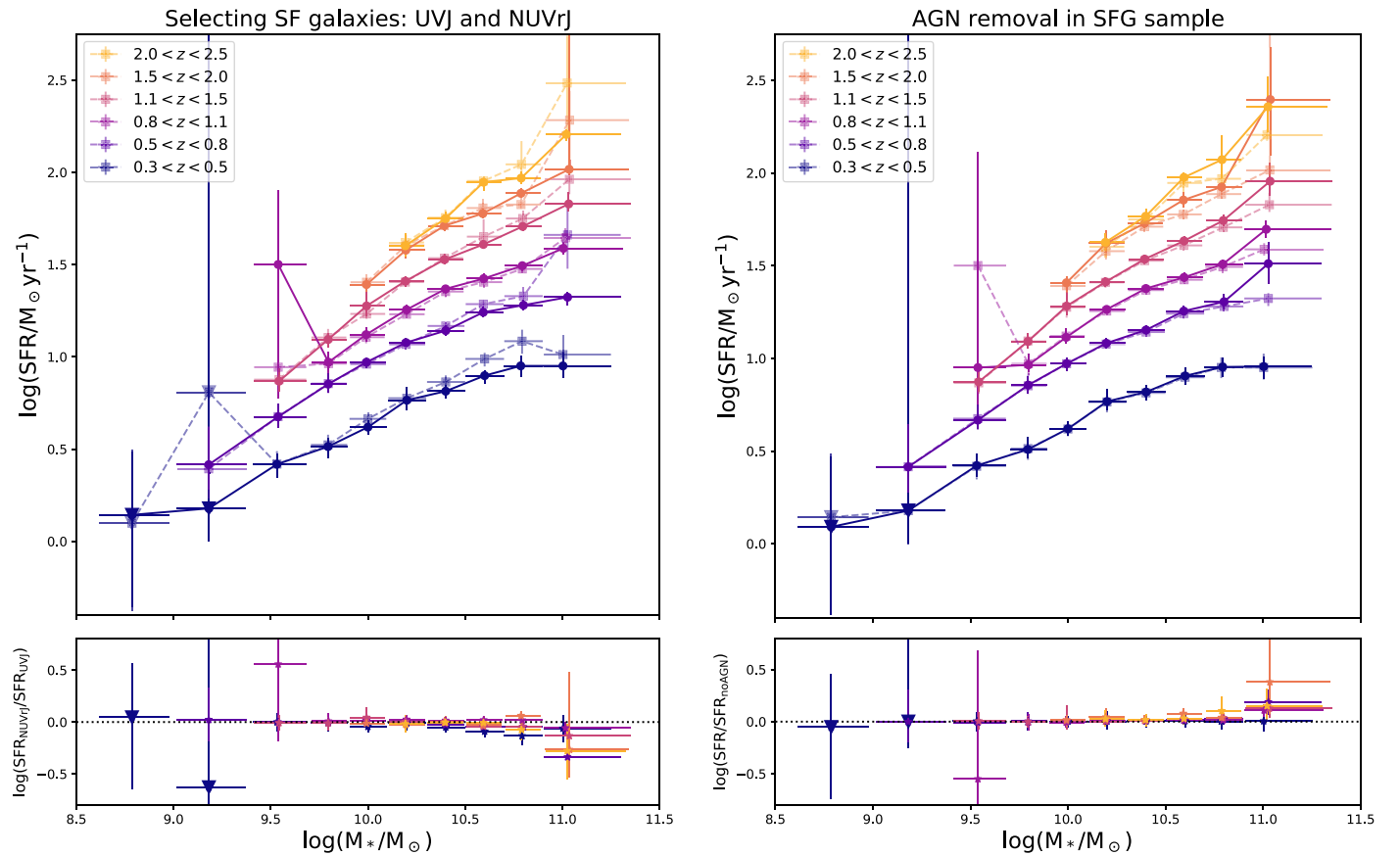


Figure B1. Different methods for selecting star-forming galaxies result in different SFR–stellar mass relations. Left: we show results using the Laigle et al. (2016) catalog photo- z and stellar mass determinations and from rest-frame UVJ or $NUVrJ$ colors for selecting star-forming galaxies. The $NUVrJ$ selection used for this work is shown as solid circles with a solid line. We show UVJ selected data as transparent squares with dashed lines between data points. The bottom panel shows the difference between $\log(\text{SFR})$ of galaxies selected using the two criteria. Right: AGN removal. Circles are no AGN (as used for this work), and transparent squares are with AGN.

compared to the $NUVrJ$ color cut. We note that for the COSMOS sample, at $z < 0.3$, the results are even more discrepant because our $NUV-r$ color requirement misses the most star-forming sources at $z < 0.3$ that are included in the $U-V$ criteria because of the different sensitivities of the NUV and U -band observations at this low redshift and the small volume probed. Thus, we have limited our analysis to $z > 0.3$.

B.2. More on AGN Removal

AGN activity and the SFR activity of their hosts are likely connected, possibly driven by a common fueling mechanism (Vito et al. 2014). The cosmic SFH and black hole accretion history follow a similar volume-averaged evolution (Madau & Dickinson 2014). Identifying AGNs is a challenging task because the SED of an AGN and host galaxy can vary widely depending on the geometry and accretion properties, in addition to the AGN energy output varying on timescales that are dependent on the wavelength (see, e.g., Elitzur et al. 2014; Schawinski et al. 2015; Buisson et al. 2017; Noda & Done 2018). Disentangling the radio emission from the AGN from that related to star formation is beyond the scope of this paper. We combine multiwavelength AGN diagnostics to reach an inclusive AGN sample as described in Section 2.4.

Figure B2 shows the fraction of galaxies hosting an AGN identified by at least one of our criteria. At all redshifts, a higher fraction of massive galaxies host detectable AGNs than do lower mass galaxies. At higher redshift, a larger fraction of massive

galaxies with blue colors host AGNs compared to at low redshift, with the fraction of massive ($\log(M_*/M_\odot) > 10.7$) SF galaxies hosting an AGN peaking at 10% at $z \sim 3$. On the other hand, when all galaxies including passive galaxies are considered, the full sample shows a peak of AGN at low redshift (12%). We note that AGN fractions are highly dependent on selection criteria, for example, the threshold fraction of the host galaxy luminosity coming from AGN emission required for a system to be classified as an AGN at a given wavelength. Our AGN fractions of $< 12\%$ for massive galaxies are broadly consistent with the literature, for example, Assef et al. (2013; 2%–8%; $z < 3$) Haggard et al. (2010; 0.15%–4%; $z < 0.7$), and Mishra & Dai (2020; 0.3%–8%; $z < 0.7$). It is not surprising that our fractions are, in some cases, higher than these literature values, due to our inclusive multi-wavelength AGN criteria.

Figure B1 shows the difference in average SFR inferred between no AGN deselection and our strict AGN deselection. The mean fluxes are more affected than the median fluxes by the presence of AGNs because the mean is more sensitive to outliers (shown in Figure A2). Radio-loud AGNs are often found in host galaxies with red colors and so are excluded using our passive criteria (e.g., jet-mode AGNs; Heckman & Best 2014). In radiative-mode AGNs (e.g., Seyfert galaxies), the radio emission comes from a combination of star formation and AGN activity (see, e.g., Heckman & Best 2014 for a review). Mid-IR criteria are often able to select these, often quite powerful, AGNs (e.g., Jarrett et al. 2011; Mateos et al. 2012; Williams et al. 2018).

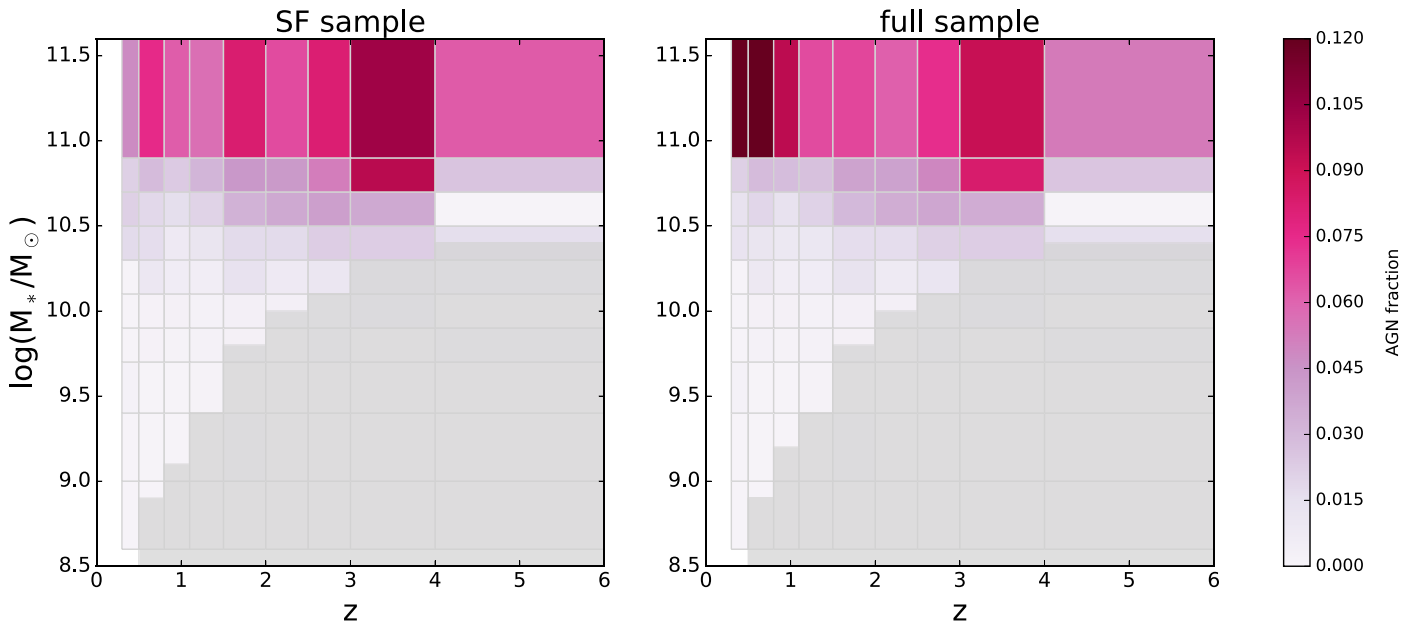


Figure B2. Fraction of galaxies hosting an AGN selected by multiwavelength criteria (see Appendix B.1) in bins of stellar mass and redshift. Gray shading indicates where the COSMOS2015 catalog is not mass complete.

Appendix C Functional Form of the MS across Redshift

In this section, we are concerned with how to best represent the SFR– M_* relation given by our data. First, we fit the MS relation at each redshift bin by comparing a power-law and broken power-law model, and then we discuss different functional forms that take both stellar mass and redshift as independent variables. For readability, we will omit units in the equations of this section, but all SFRs have units of $M_\odot \text{ yr}^{-1}$, and stellar mass is denoted M_* with units of M_\odot .

As described in Section 4.1, we fit models to our mass-complete data using a simple least-squares minimization. To estimate the parameter uncertainties, we resample the data 50,000 times (or 10,000 times in our first experiment, where we fit a function at each redshift), varying the stellar mass, SFR, and redshift (if included as an independent variable) of each stack by a random amount that follows a Gaussian distribution with σ given by our upper and lower errors. We then report the median, 16th, and 84th percentiles from all our runs for the best-fitted parameter distributions.

For the best fits, we report reduced χ^2 , which is the weighted sum of the squared deviations in $\log(\text{SFR})$ per degree of freedom (number of observations minus the number of fitted parameters). A $\chi_r^2 > 1$ indicates that the fit has not fully captured the data or that the error variance has been underestimated, and a $\chi_r^2 < 1$ indicates the model is overfitting the data or the error variance has been overestimated.

To compare the relative quality of different models, we have also computed the Akaike information criterion (AIC):

$$\text{AIC} = 2k - 2 \ln \left(\sum_n \frac{(\log(\text{SFR}) - \widehat{\log(\text{SFR})})^2}{n} \right), \quad (\text{C1})$$

where $\widehat{\log(\text{SFR})}$ is the predicted value, n is the number of observations, and k is the number of parameters estimated by the model plus the constant variance of the errors. The preferred model is the one with the minimum AIC. We also report a second definition of the AIC, with a correction for small sample sizes that addresses the tendency for overfitting (selecting a model with too

many parameters) that often occurs for small sample sizes (e.g., Hurvich & Tsai 1989; Cavanaugh & Shumway 1997):

$$\text{AICc} = 2k - 2 \ln \left(\sum_n \frac{(\log(\text{SFR}) - \widehat{\log(\text{SFR})})^2}{n} \right) + \frac{2k^2 + 2k}{n - k - 1}. \quad (\text{C2})$$

The AIC does not give information on the absolute quality of the model, but rather only the quality of a model relative to other models. Only differences in AIC are meaningful; we interpret $\Delta\text{AIC} > 2$ to be evidence against the model with the higher AIC, and >6 to be strong evidence and >10 to be very strong evidence against the model with the higher AIC (or strong evidence for preferring the model with the lower AIC).

Table C1 gives the results of fitting the $\log(\text{SFR})$ – $\log(M_*)$ relation for individual redshift slices (out to $z = 2$, where we have enough data in each bin to constrain a three-parameter model) using a linear form,

$$\log(\text{SFR}) = a_1 \log(M_*/10^9) + a_2, \quad (\text{C3})$$

and the Lee et al. (2015) form,

$$\log(\text{SFR}) = S_0 - \log \left(1 + \left(\frac{10^M}{10^{M_0}} \right)^{-\gamma} \right), \quad (\text{C4})$$

where $M = \log(M_*/M_\odot)$, γ is the power-law slope at lower stellar masses, and S_0 is the maximum value of $\log(\text{SFR})$ approached at higher stellar masses.

In general, the bent MS produces more favorable reduced χ^2 (closest to 1), and there is very strong evidence that a bent MS relation is preferred to a linear relation at $z < 1.1$, and strong evidence at $1.1 < z < 1.5$ as well. However, using the AIC based on Equation (C1) (rather than Equation (C2)) implies that the linear form is preferred at $z > 1.1$. This is likely due to the smaller number of mass-complete measurements available for low-mass constraints at higher redshift. These results are consistent with Lee et al. (2018), who found that the MS can be

Table C1
Linear (Equation (C3)) and Nonlinear (Equation (C4) Lee et al. 2015) MS Model Fits to Mass-complete Data at $z < 2$ with $S/N > 10$

Redshift	Linear Form (a_1, a_2)	χ_r^2	Lee Form (S_0, M_0, γ)	χ_r^2	ΔAIC	ΔAICc
$0.2 < z < 0.5$	$(0.40^{+0.05}_{-0.05}, 0.22^{+0.06}_{-0.06})$	1.5	$(1.09^{+0.28}_{-0.10}, 10.33^{+0.86}_{-0.27}, -0.77^{+0.22}_{-0.31})$	0.7	7.2	0.2
$0.5 < z < 0.8$	$(0.46^{+0.07}_{-0.06}, 0.45^{+0.09}_{-0.08})$	8.0	$(1.42^{+0.13}_{-0.06}, 10.3^{+0.39}_{-0.17}, -0.83^{+0.18}_{-0.17})$	0.57	22.8	16.9
$0.8 < z < 1.1$	$(0.46^{+0.08}_{-0.3}, 0.68^{+0.45}_{-0.13})$	4.1	$(1.83^{+7.1}_{-0.20}, 10.7^{+33}_{-0.44}, -0.69^{+0.54}_{-0.35})$	25.0	14.9	21.9
$1.1 < z < 1.5$	$(0.63^{+0.05}_{-0.06}, 0.59^{+0.09}_{-0.06})$	5.8	$(1.93^{+0.18}_{-0.19}, 10.62^{+0.56}_{-0.3}, -0.93^{+0.23}_{-0.16})$	1.3	9.1	2.1
$1.5 < z < 2.0$	$(0.58^{+0.05}_{-0.06}, 0.86^{+0.11}_{-0.07})$	2.8	$(2.22^{+6.3}_{-0.27}, 10.95^{+13.7}_{-0.5}, -0.82^{+0.30}_{-0.35})$	10.77	-8.4	-36.3

Note. $\Delta\text{AIC(c)}$ is $\text{AIC}_{\text{linear}} - \text{AIC}_{\text{Lee}}$ calculated using Equation (C1) (Equation (C2)). The more positive the $\Delta\text{AIC(c)}$, the more the Lee et al. form is preferred. The more negative the ΔAIC , the more the linear form is preferred. Note the large uncertainties for the $0.8 < z < 1.1$ results.

Table C2
MS Model Fits to All Mass-complete Data with $S/N > 10$, Adopting the Molnár et al. (2020) SFR Calibration

MS Form (\mathcal{M})	Parameters (Θ)	Best-fit Values	χ_r^2
SF, Speagle et al. (2014), Equation (C5)	(a_1, a_2, a_3, a_4)	$(0.76^{+0.08}_{-0.10}, 0.041^{+0.012}_{-0.013}, 5.6^{+0.9}_{-1.0}, 0.26^{+0.13}_{-0.13})$	4.7
SF, Schreiber et al. (2015), Equation (C6)	$(m_0, a_0, a_1, m_1, a_2)$	$(-0.60^{+0.49}_{-0.15}, 0.11^{+0.81}_{-0.11}, 0.10^{+0.06}_{-0.01}, -2.8^{+1.5}_{-1.5}, 4.7^{+0.6}_{-1.5})$	30
SF, Tomczak et al. (2016), Equation (C7)	$(s_0, m_0, a_1, a_2, a_3, a_4)$	$(0.52^{+0.12}_{-0.14}, 9.39^{+0.30}_{-0.44}, 1.22^{+0.22}_{-0.18}, 0.16^{+0.07}_{-0.04}, 0.96^{+0.48}_{-0.36}, 0.15^{+0.13}_{-0.08})$	7.3
SF, This work, Equation (6)	(s_0, m_0, a_1, a_2)	$(2.965^{+0.081}_{-0.088}, 11.07^{+0.15}_{-0.16}, 0.215^{+0.012}_{-0.012}, 0.120^{+0.027}_{-0.024})$	6.5
All, Speagle et al. (2014) Equation (C5)	(a_1, a_2, a_3, a_4)	$(0.75^{+0.11}_{-0.13}, 0.063^{+0.019}_{-0.018}, 5.5^{+1.2}_{-1.4}, 0.48^{+0.20}_{-0.18})$	6.9
All, Schreiber et al. (2015), Equation (C6)	$(m_0, a_0, a_1, m_1, a_2)$	$(-0.233^{+0.32}_{-0.60}, 0.76^{+0.50}_{-0.76}, 0.19^{+0.09}_{-0.07}, -1.40^{+0.78}_{-1.41}, 3.43^{+0.92}_{-0.87})$	2.4
All, Tomczak et al. (2016), Equation (C7)	$(s_0, m_0, a_1, a_2, a_3, a_4)$	$(0.23^{+0.11}_{-0.11}, 8.9^{+0.35}_{-0.64}, 1.33^{+0.16}_{-0.17}, 0.199^{+0.049}_{-0.050}, 1.26^{+0.67}_{-0.44}, 0.226^{+0.186}_{-0.116})$	2.9
All, This work, Equation (6)	(s_0, m_0, a_1, a_2)	$(2.80^{+0.080}_{-0.085}, 10.82^{+0.15}_{-0.16}, 0.226^{+0.011}_{-0.011}, 0.131^{+0.028}_{-0.024})$	9.0

described by a simple linear relation in $\log(M_*)$ and $\log(\text{SFR})$ at $z > 2$, whereas below $z \sim 1.5$, there is a statistically significant flattening at high stellar masses.

Looking at the fitted parameters of the Lee et al. (2015) form in Table C1, we find clearly that S_0 and M_0 increase with redshift (M_0 evolution is illustrated in Figure 7). We considered this when developing the functional form of Equation (6).

It is most convenient to provide a functional form that takes stellar mass and redshift as independent parameters and returns an SFR. Next, we will fit our data with functional forms adopted in the literature that allow this, including the new parameterization proposed in Equation (6).

A simple functional form adopted in the literature is that of a linear relationship between $\log(\text{SFR})$ and $\log(M_*)$. Speagle et al. (2014) compiled 25 studies from the literature and fitted the following linear form to the MS that allows for evolution of both the slope and normalization³³:

$$\log(\text{SFR}) = (a_1 - a_2 t) \log(M_*) - (a_3 - a_4 t), \quad (\text{C5})$$

where t is the age of the universe in Gyr. We have fit this functional form to our data and report the best-fitting parameters $\Theta = (a_1, a_2, a_3, a_4)$ in Table C2. This form performs poorly for our low-redshift ($z < 1$) data, but matches our high- z data well.

The following functional forms allow for a flattening at high masses in the MS. We have investigated fitting the functional form used by Schreiber et al. (2015), namely

$$\log(\text{SFR}) = m - m_0 + a_0 r - a_1 [\max(0, m - m_1 - a_2 r)]^2 \quad (\text{C6})$$

where $r = \log(1 + z)$ and $m = \log(M_*/10^9)$. This relation constrains the low-mass slope by assuming a constant sSFR (i.e., a low-mass slope of 1). The posterior distribution of these parameters is not smoothly distributed. To produce reasonable constraints on our parameters, we added the following bounds:

³³ However, most studies agree that the slope remains relatively constant over time, e.g., Wuyts et al. (2011).

$a_0 > 0$, $a_1 > 0$, and $a_2 > 0$ and $-3 < m_1 < 12$. For this case, the ‘‘Trust Region Reflective’’ algorithm was used for optimization in SCIPY.OPTIMIZE.

Tomczak et al. (2016) fit the Lee et al. (2015) function with a quadratic evolution of parameters with redshift:

$$\begin{aligned} \log(\text{SFR}) &= S'_0 - \log\left(1 + \left(\frac{M}{10M'_0}\right)^{-\gamma}\right), \\ S'_0 &= s_0 + a_1 z - a_2 z^2 \\ M'_0 &= m_0 + a_3 z - a_4 z^2 \\ \gamma &= 1.091. \end{aligned} \quad (\text{C7})$$

Again, all best fits are reported in Table C2.

Appendix D Comparison with Literature

The diversity of sSFRs from different studies as a function of stellar mass and redshift, normalized by the relation given in Equation (6), is shown in Figure D1. All literature relations were converted to the same Chabrier IMF used in this study when necessary (as mentioned below). We do not correct for the small effect that different cosmologies introduce into the relations. The mass range shown in Figure D1 illustrates where the literature studies are complete. There is a spread of >0.2 dex between different MS relations. Below we discuss the pertinent details on how MS relations shown in Figure D1 were derived.

1. Bisigello et al. (2018) fitted linear $\text{SFR}-M_*$ relations for three populations of galaxies in the CANDELS/GOODS-S field, a starburst, main-sequence, and quiescent population, assuming each population follows a log-normal sSFR distribution. They fit galaxies in three bins in the range $0.5 < z < 3$ and stellar masses down to $\log(M_*/M_\odot) > 7.5$. Bisigello et al. (2018) adopted a $(\Omega_M, \Omega_\Lambda, H_0) = (0.27, 0.73, 70)$ cosmology and Salpeter IMF. In Figure D1 we include

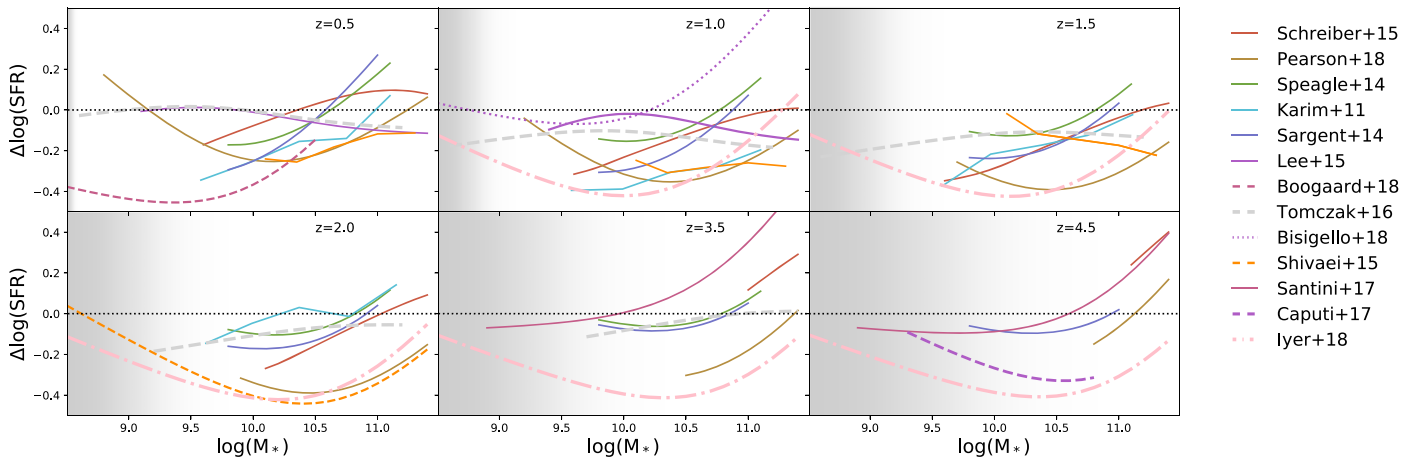


Figure D1. Difference between SFRs resulting from the literature MS relations and the MS relation in this work (Equation (6)). The gray shaded area illustrates where this work is incomplete in stellar mass. We note that our SFRs lie above the literature at $M_* = 10^{10} M_\odot$, which is the mass that contributes the most to the cosmic SFRD. This offset might lead to the discrepancies seen in Figure 8 between our result and the Madau & Dickinson (2014) compilation curve.

the $1 < z < 2$ relation, whose SFRs were calculated from UV plus IR luminosities (where IR luminosity is from Chary & Elbaz 2001 template fitting).

2. Boogaard et al. (2018) selected star-forming galaxies at $0.11 < z < 0.91$, with two hydrogen Balmer emission lines detected with $S/N > 3$ from which they calculated SFR. Star-forming galaxies were further required to have $D_n(4000) < 1.5$, $EW_{H\alpha} > 2 \text{ \AA}$, and $EW_{H\beta} > 2 \text{ \AA}$. Boogaard et al. (2018) found a linear relation between $\log(\text{SFR})$ and $\log(M_*/M_\odot)$ over the mass range probed ($7 < \log(M_*/M_\odot) < 10.5$).
3. Caputi et al. (2017) obtained $H\alpha$ -derived SFRs from $H\alpha + [N \text{ II}] + [S \text{ II}]$ equivalent-width measurements of galaxies in the Spitzer Matching Survey of the UltraVISTA Ultra-Deep Stripes over the range $3.9 < z < 4.9$. They report a bimodal distribution in sSFR, interpreted as a main-sequence and starburst population. For the main-sequence population, they report a linear relation, constrained across a mass range $9.2 < \log(M_*/M_\odot) < 10.8$. Above this stellar mass, they postulate that AGN contamination influences the SFR measurements.
4. Iyer et al. (2018) used the UVJ colors to select $\sim 18,000$ galaxies in the CANDELS GOODS-S field at $0.5 < z < 6$. The galaxy SED fits provide stellar mass and SFR measurements. In addition, the SFHs were reconstructed, allowing for more data points on the MS relation at high redshift down to a representative mass of $\log(M_*/M_\odot) \sim 7$ (90% representative at $z \sim 7.5$).
5. Karim et al. (2011) used 1.4 GHz data and the Bell (2003) SFR calibration (assuming $\alpha = -0.8$) to calculate SFRs for COSMOS galaxies across $0.2 < z < 3$. SF galaxies were selected using $NUV-r$ rest-frame color cuts. We show individual stacked mass-complete data points (rather than the fit function) in Figure D1.
6. Lee et al. (2015) studied star-forming galaxies selected by an $NUVrJ$ color-color cut (Ilbert et al. 2013). The SFRs were calculated from IR and UV data assuming a Hinshaw et al. (2013) cosmology ($\Omega_M, \Omega_\Lambda, H_0$) = (0.28, 0.72, $70.4 \text{ km s}^{-1} \text{ Mpc}^{-2}$). The mass limit used for fitting was given in their Table 1. Lee et al. (2015) fit the MS for galaxies at $0.25 < z < 1.3$ with the functional form (C4).
7. Pearson et al. (2018) fit a linear MS relation over a redshift range $0.2 < z < 6$ in the COSMOS field,

calculating SFRs and stellar masses via SED fitting. SF galaxies were selected using a redshift-dependent UVJ color-color cut, and a slightly different cosmology (Larson et al. 2011) was assumed of ($\Omega_M, \Omega_\Lambda, H_0$) = (0.273, 0.727, $70.4 \text{ km s}^{-1} \text{ Mpc}^{-2}$). Figure D1 compares our result to the Pearson et al. (2018) MS, showing the 90% mass-completeness limits calculated for the COSMOS UDeep field K_s -band magnitude limit.

8. Popesso et al. (2015) constrained the shape of the MS to a local value (MS_0 ; Popesso et al. 2019a) and fit an evolution of the overall normalization out to $z < 2.5$, $\text{SFR}(z, M_*) = MS_0 \times 1.01(1+z)^{3.21}$, for galaxies more massive than $\log(M_*/M_\odot) > 10$. Data in the GOODS +CANDELS and COSMOS-PEP (with the latter being limited to $z < 0.7$ or $\log(M_*/M_\odot) > 10.8$) fields containing Herschel and Spitzer coverage were used to calculate SFRs by combining FIR and UV luminosities. The location of the MS in their work is defined as the location of the peak of the log-normal SFR distribution, as in Renzini & Peng (2015), which is the median SFR of the distribution.
9. Santini et al. (2017) studied the MS in the HST frontier fields at $1.3 < z < 6$. They were able to probe $\log(M_*/M_\odot) > 7.5$ at $z < 4$ and $\log(M_*/M_\odot) > 8$ at $z > 4$. They fit the MS separately for different redshift bins with a linear relation, selecting main-sequence galaxies by a sigma clipping. Figure D1 only shows their fits for $3 < z < 4$ and $4 < z < 5$ because these match the z slices at which we are demonstrating. Santini et al. (2017) adopted a Salpeter IMF and calculate SFRs using rest-frame UV data (Castellano et al. 2012).
10. Sargent et al. (2014) compiled data from 16 different studies spanning $0 < z < 7$ and fit a power-law fit to the sSFR- z relation. Two mass scales were considered: $M_* \sim 5 \times 10^9 M_\odot$ and $M_* \sim 5 \times 10^{10} M_\odot$. The samples used by Sargent et al. (2014) include a mix of selection methods and SFR tracers, but all were converted to the WMAP-7 cosmology (Larson et al. 2011).
11. Schreiber et al. (2015) stacked Herschel data in the extragalactic GOODS-N, GOODS-S, UDS, and COSMOS fields to derive SFRs (they also added unobscured UV SFRs). A Salpeter IMF was used. In Figure D1 we show their function (of form (C6)) only over a mass range where a stacked signal was detected.

12. Shivaei et al. (2015) used H α and H β spectroscopy to derive dust-corrected instantaneous SFRs for 261 galaxies spanning $9.5 < \log(M_*/M_\odot) < 11.5$ and $1.37 < z < 2.61$ in the MOSFIRE Deep Evolution Field (MOSDEF) survey.
13. Speagle et al. (2014) compiled literature data from 25 studies, and we show their best fit for studies that have a “mixed” SF selection. Speagle et al. (2014) report a 1σ intersample scatter of < 0.1 dex. They fit a linear form (of form Equation (C5)) over a stellar mass range $9.7 < \log(M_*/M_\odot) < 11.1$ and a redshift range of $0.16 < z < 3.15$ (data from the first and last 2 Gyr were removed). They adopted a Kroupa (2001) IMF.
14. Tomczak et al. (2016) report an MS with a turnover (of the form C7) over a redshift range $0.5 < z < 4$ and mass

range $8.5 < \log(M) < 11.0$. SF galaxies were selected using a *UVJ* selection. Their SFRs come from UV+IR data from the FourStar Galaxy Evolution Survey (ZFOURGE) in combination with far-IR imaging from the Spitzer and Herschel observatories.

Appendix E Extra Figures

Binning schemes for our galaxy morphology analysis (Section 4.4) and local environment analysis (Section 4.5) are shown in Figures E1 and E2, respectively. Figure E3 shows the halo mass–redshift distribution of X-ray groups in the COSMOS field.

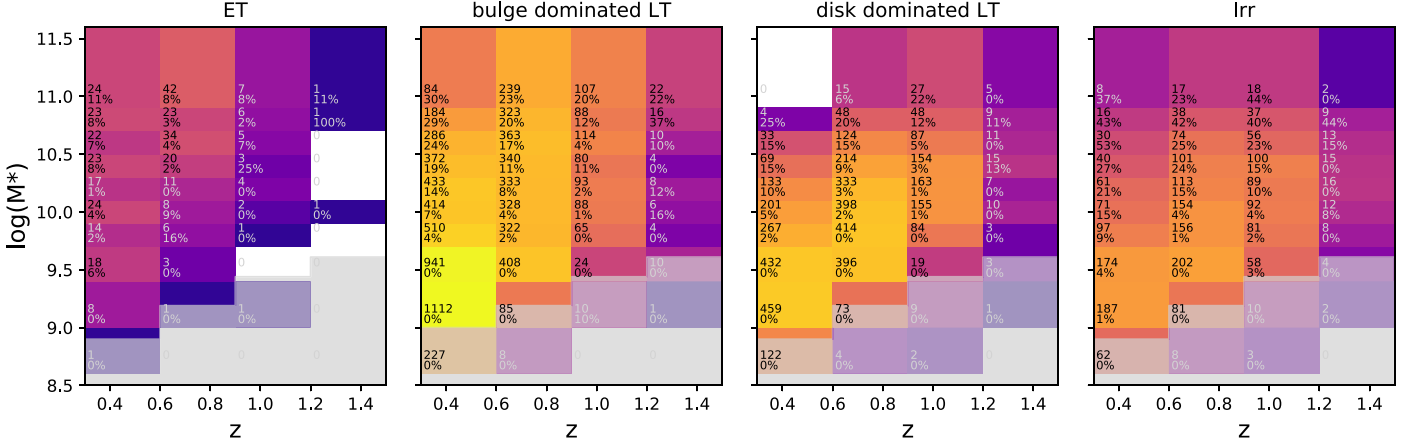


Figure E1. Binning scheme for our morphology analysis using morphological classes based on the Zurich Structure and Morphology Catalog (Scarlata et al. 2007). Star-forming galaxies are selected using the *NUVrJ* color–color cut. Numbers for each bin are provided analogous to Figure 2.

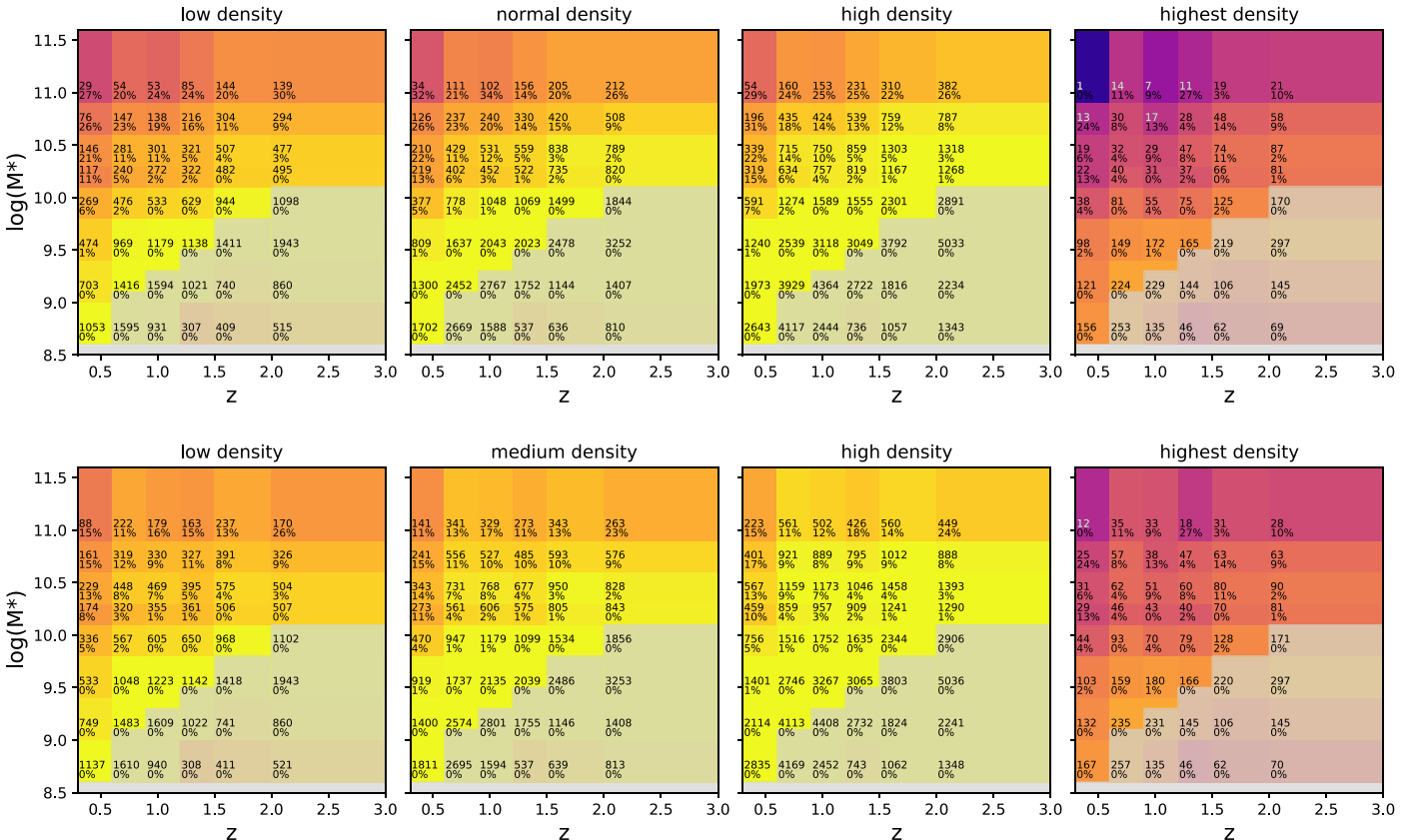


Figure E2. Binning scheme for our environment analysis using local density estimates from Scoville et al. (2013). Star-forming galaxies (top panels) are selected using the *NUVrJ* color–color cut. Numbers for each bin are provided analogous to Figure 2.

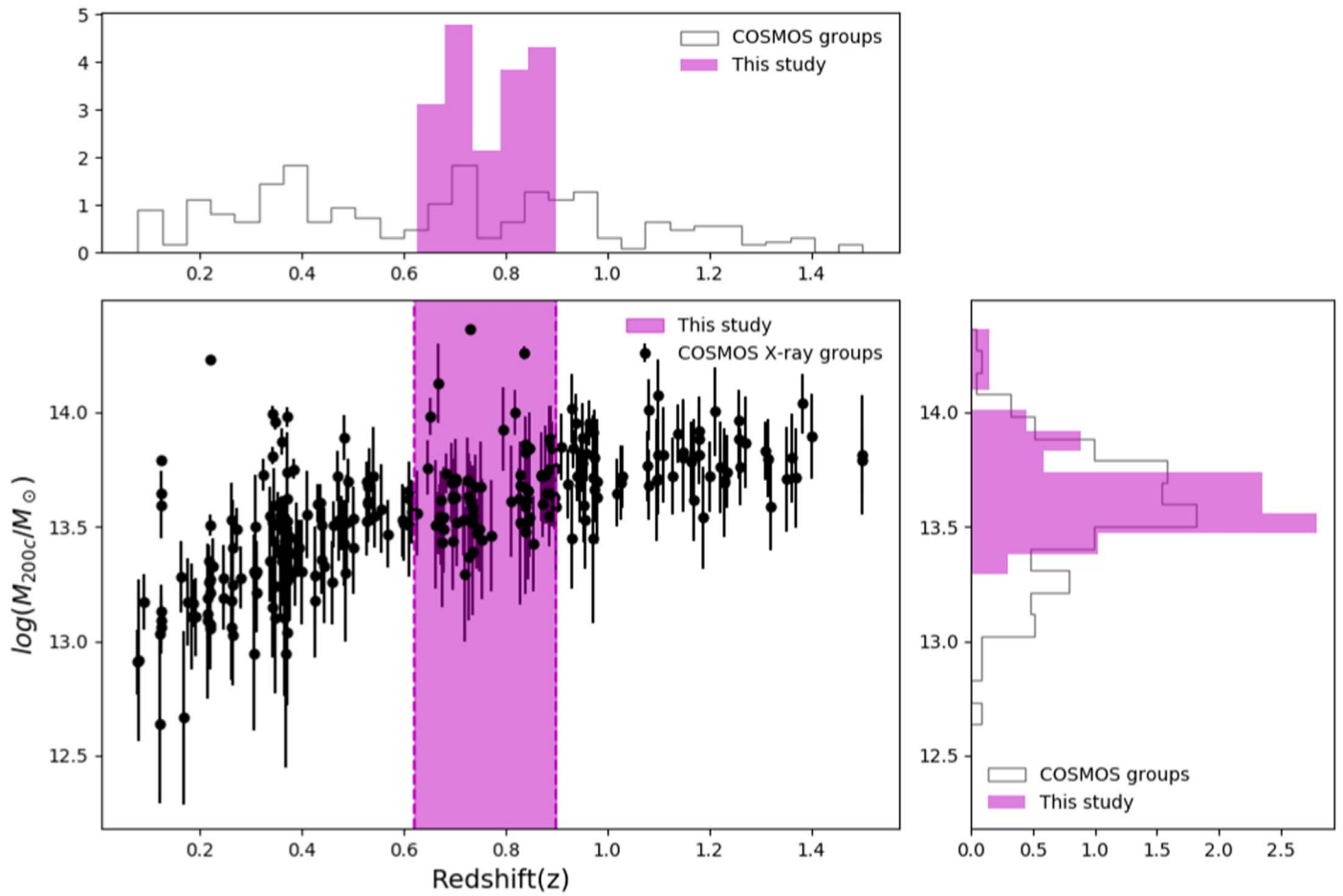


Figure E3. Halo mass of X-ray-selected groups (M_{200c}) in the COSMOS field as a function of their redshift (filled black circles; Gozaliasl et al. 2019). The highlighted magenta region represents 73 groups within a redshift range of $0.62 < z < 0.88$ used in this study. The redshift and halo mass distributions of all X-ray groups and those used in this study are presented in the upper left and lower right panels.

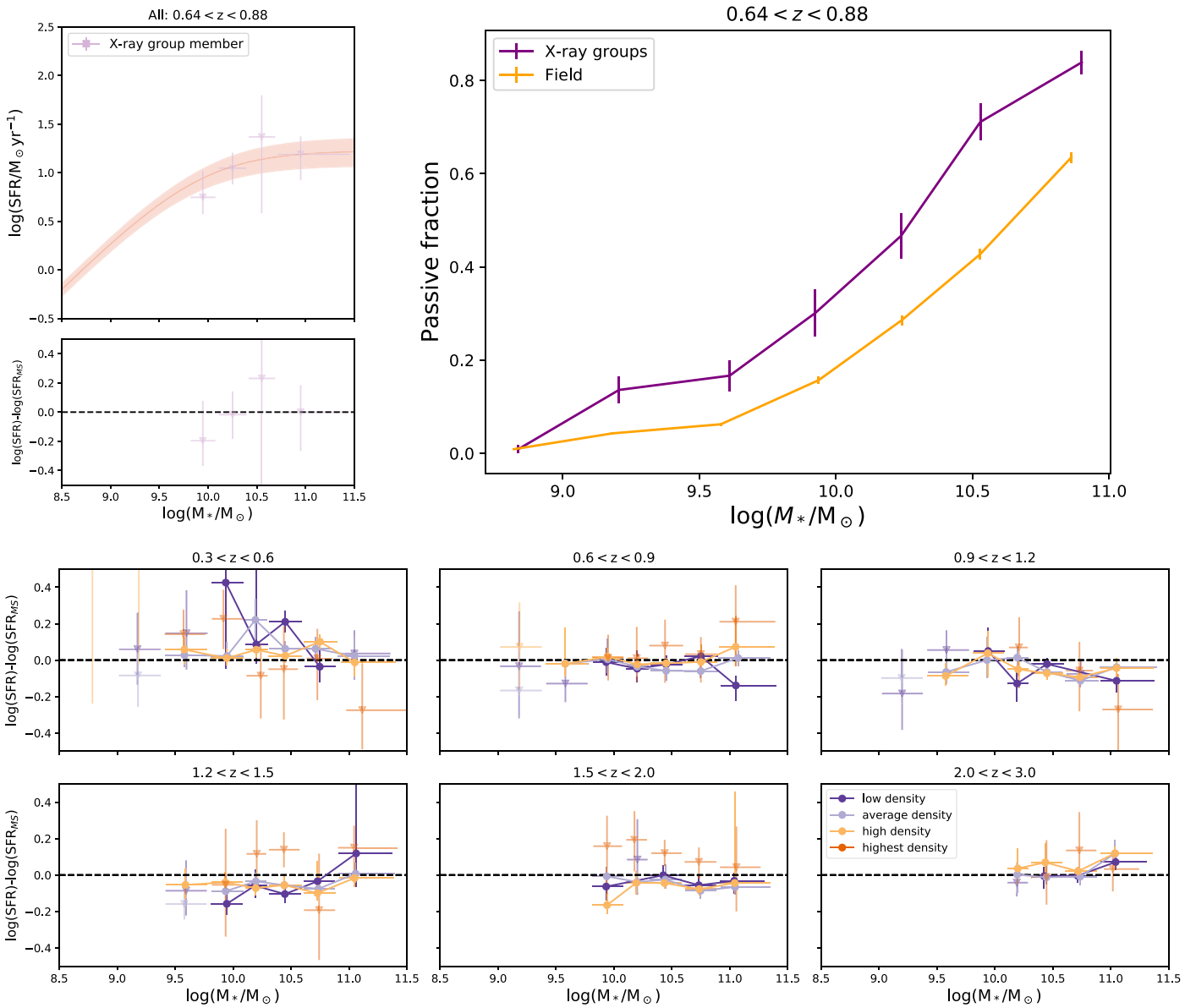


Figure E4. Environmental trends for all galaxies (including passive). Top left: MS relation of galaxies in X-ray groups compared to all galaxies regardless of environment. Top right: fraction of *NUVrJ*-selected passive galaxies as a function of stellar mass for X-ray groups, compared to galaxies regardless of environment. The bottom panels show the difference between the SFR from the MS (calculated for all galaxies) and the SFR of galaxies in different groups. In all cases there is no clear difference between the different environments, as traced by the density fields of Scoville et al. (2013).

We show in Figure E4 that the MS-derived relation for all galaxies shows no statistically significant difference between low- and high-density local environments, nor in X-ray groups at $z \sim 0.76$.

Appendix F Tables with Radio Stacking Results

Tables F1 and F2 show the measured fluxes from the analysis presented in Section 4.1.

Table F1
3 GHz Stacking Results for Star-forming Mass-selected Galaxies Where Our Sample Is Mass-complete

Δz_p	$\langle z_p \rangle$	$\Delta \log(M_*)$ $\log(M_\odot)$	$\langle \log(M_*) \rangle$ $\log(M_\odot)$	N_{obj}	S_p ($\mu\text{Jy}/\text{beam}$)	S_t (μJy)	rms ($\mu\text{Jy}/\text{beam}$)	$\log(\text{SFR})$ $\log(M_\odot \text{ yr}^{-1})$	
0.3–0.5	0.40	8.6–9.0	8.79	3484	$0.26^{+0.05}_{-0.07}$	$2.23^{+4.32}_{-1.66}$	$0.050^{+0.001}_{-0.001}$	$0.08^{+0.40}_{-0.50}$	
	0.39	9.0–9.4	9.18	2566	$0.51^{+0.07}_{-0.08}$	$2.70^{+1128.23}_{-0.80}$	$0.058^{+0.000}_{-0.000}$	$0.13^{+2.22}_{-0.13}$	
	0.38	9.4–9.7	9.53	1322	$1.24^{+0.09}_{-0.04}$	$5.89^{+1.05}_{-0.93}$	$0.082^{+0.002}_{-0.001}$	$0.41^{+0.06}_{-0.06}$	
	0.38	9.7–9.9	9.79	653	$1.93^{+0.17}_{-0.17}$	$7.98^{+1.38}_{-0.84}$	$0.118^{+0.002}_{-0.000}$	$0.50^{+0.06}_{-0.04}$	
	0.39	9.9–10.1	10.00	512	$2.58^{+0.29}_{-0.24}$	$10.19^{+1.00}_{-1.16}$	$0.129^{+0.002}_{-0.005}$	$0.62^{+0.03}_{-0.04}$	
	0.38	10.1–10.3	10.20	430	$3.99^{+0.28}_{-0.22}$	$15.54^{+3.77}_{-1.85}$	$0.143^{+0.002}_{-0.002}$	$0.76^{+0.08}_{-0.05}$	
	0.38	10.3–10.5	10.40	340	$4.37^{+0.43}_{-0.55}$	$18.15^{+2.09}_{-2.20}$	$0.164^{+0.001}_{-0.002}$	$0.81^{+0.04}_{-0.05}$	
	0.39	10.5–10.7	10.60	227	$5.58^{+0.62}_{-0.90}$	$21.13^{+2.22}_{-1.72}$	$0.197^{+0.002}_{-0.002}$	$0.89^{+0.04}_{-0.03}$	
	0.38	10.7–10.9	10.79	139	$5.12^{+1.68}_{-0.84}$	$25.88^{+3.05}_{-3.52}$	$0.250^{+0.005}_{-0.002}$	$0.94^{+0.04}_{-0.05}$	
	0.39	10.9–11.6	11.00	80	$4.40^{+1.31}_{-1.13}$	$25.31^{+6.39}_{-4.39}$	$0.322^{+0.004}_{-0.008}$	$0.95^{+0.08}_{-0.07}$	
0.5–0.8	0.68	9.0–9.4	9.18	6623	$0.46^{+0.05}_{-0.03}$	$1.80^{+1.42}_{-0.70}$	$0.036^{+0.001}_{-0.001}$	$0.45^{+0.21}_{-0.18}$	
	0.67	9.4–9.7	9.54	3371	$0.89^{+0.04}_{-0.04}$	$3.29^{+0.71}_{-0.50}$	$0.050^{+0.000}_{-0.000}$	$0.66^{+0.07}_{-0.06}$	
	0.67	9.7–9.9	9.80	1633	$1.56^{+0.10}_{-0.13}$	$5.55^{+0.77}_{-0.66}$	$0.073^{+0.002}_{-0.002}$	$0.85^{+0.05}_{-0.05}$	
	0.67	9.9–10.1	9.99	1277	$2.24^{+0.10}_{-0.10}$	$7.44^{+0.62}_{-0.63}$	$0.083^{+0.003}_{-0.001}$	$0.96^{+0.03}_{-0.03}$	
	0.67	10.1–10.3	10.20	1031	$3.32^{+0.12}_{-0.17}$	$10.09^{+0.83}_{-0.50}$	$0.093^{+0.002}_{-0.003}$	$1.07^{+0.03}_{-0.02}$	
	0.67	10.3–10.5	10.40	782	$3.64^{+0.18}_{-0.18}$	$11.92^{+0.83}_{-0.77}$	$0.106^{+0.002}_{-0.002}$	$1.14^{+0.02}_{-0.02}$	
	0.67	10.5–10.7	10.59	602	$4.50^{+0.14}_{-0.21}$	$15.81^{+1.17}_{-1.23}$	$0.118^{+0.001}_{-0.001}$	$1.24^{+0.03}_{-0.03}$	
	0.67	10.7–10.9	10.80	368	$5.11^{+0.27}_{-0.24}$	$17.24^{+1.52}_{-1.40}$	$0.161^{+0.006}_{-0.008}$	$1.27^{+0.03}_{-0.03}$	
	0.68	10.9–11.6	11.03	233	$4.91^{+0.29}_{-0.40}$	$18.81^{+2.02}_{-1.71}$	$0.187^{+0.002}_{-0.001}$	$1.31^{+0.04}_{-0.04}$	
	0.8–1.1	0.95	9.0–9.4	9.19	8935	$0.38^{+0.05}_{-0.03}$...	$0.032^{+0.001}_{-0.001}$...
0.95		9.4–9.7	9.54	4916	$0.79^{+0.05}_{-0.05}$	$2.97^{+48.38}_{-1.19}$	$0.042^{+0.001}_{-0.001}$	$0.92^{+1.05}_{-0.19}$	
0.94		9.7–9.9	9.80	2495	$1.31^{+0.04}_{-0.06}$	$3.30^{+0.55}_{-0.37}$	$0.060^{+0.001}_{-0.002}$	$0.95^{+0.06}_{-0.04}$	
0.94		9.9–10.1	9.99	1978	$1.97^{+0.07}_{-0.07}$	$5.06^{+0.57}_{-0.54}$	$0.065^{+0.001}_{-0.001}$	$1.11^{+0.04}_{-0.04}$	
0.93		10.1–10.3	10.20	1526	$2.62^{+0.11}_{-0.11}$	$7.50^{+0.54}_{-0.45}$	$0.075^{+0.001}_{-0.002}$	$1.25^{+0.03}_{-0.02}$	
0.93		10.3–10.5	10.40	1176	$3.65^{+0.14}_{-0.13}$	$10.19^{+0.67}_{-0.59}$	$0.086^{+0.002}_{-0.002}$	$1.36^{+0.02}_{-0.02}$	
0.93		10.5–10.7	10.60	878	$4.28^{+0.23}_{-0.13}$	$11.85^{+0.68}_{-0.63}$	$0.100^{+0.001}_{-0.002}$	$1.42^{+0.02}_{-0.02}$	
0.92		10.7–10.9	10.79	509	$4.84^{+0.50}_{-0.37}$	$14.89^{+1.31}_{-1.17}$	$0.132^{+0.002}_{-0.004}$	$1.49^{+0.03}_{-0.03}$	
0.93		10.9–11.6	11.01	331	$5.99^{+0.47}_{-0.33}$	$18.76^{+1.65}_{-1.25}$	$0.161^{+0.001}_{-0.001}$	$1.58^{+0.03}_{-0.03}$	
1.1–1.5		1.29	9.4–9.7	9.54	6850	$0.62^{+0.04}_{-0.04}$	$1.25^{+0.24}_{-0.17}$	$0.036^{+0.000}_{-0.000}$	$0.86^{+0.06}_{-0.05}$
	1.29	9.7–9.9	9.79	3480	$1.02^{+0.03}_{-0.05}$	$2.20^{+0.30}_{-0.25}$	$0.050^{+0.000}_{-0.000}$	$1.07^{+0.05}_{-0.04}$	
	1.28	9.9–10.1	9.99	2748	$1.56^{+0.06}_{-0.06}$	$3.83^{+1.12}_{-0.53}$	$0.057^{+0.000}_{-0.001}$	$1.27^{+0.09}_{-0.05}$	
	1.31	10.1–10.3	10.19	2218	$2.02^{+0.08}_{-0.07}$	$5.21^{+0.39}_{-0.33}$	$0.062^{+0.000}_{-0.000}$	$1.40^{+0.03}_{-0.03}$	
	1.32	10.3–10.5	10.39	1641	$2.66^{+0.10}_{-0.07}$	$7.02^{+0.52}_{-0.49}$	$0.074^{+0.001}_{-0.001}$	$1.52^{+0.03}_{-0.03}$	
	1.30	10.5–10.7	10.59	1284	$3.35^{+0.16}_{-0.15}$	$9.09^{+0.53}_{-0.57}$	$0.083^{+0.002}_{-0.000}$	$1.60^{+0.02}_{-0.02}$	
	1.31	10.7–10.9	10.80	813	$4.55^{+0.24}_{-0.27}$	$11.72^{+0.71}_{-0.64}$	$0.102^{+0.003}_{-0.003}$	$1.70^{+0.02}_{-0.02}$	
	1.32	10.9–11.6	11.03	611	$4.74^{+0.40}_{-0.39}$	$15.88^{+3.42}_{-1.52}$	$0.118^{+0.003}_{-0.002}$	$1.82^{+0.07}_{-0.04}$	
	1.5–2.0	1.75	9.9–10.1	9.99	3050	$1.17^{+0.07}_{-0.05}$	$2.56^{+0.26}_{-0.30}$	$0.053^{+0.000}_{-0.000}$	$1.39^{+0.03}_{-0.05}$
		1.76	10.1–10.3	10.19	2449	$1.65^{+0.08}_{-0.08}$	$4.19^{+0.60}_{-0.51}$	$0.060^{+0.001}_{-0.001}$	$1.57^{+0.05}_{-0.05}$
1.75		10.3–10.5	10.39	1940	$2.31^{+0.07}_{-0.10}$	$6.00^{+0.57}_{-0.48}$	$0.067^{+0.001}_{-0.000}$	$1.70^{+0.03}_{-0.03}$	
1.76		10.5–10.7	10.59	1398	$3.06^{+0.10}_{-0.13}$	$7.28^{+0.41}_{-0.43}$	$0.079^{+0.003}_{-0.001}$	$1.77^{+0.02}_{-0.02}$	
1.77		10.7–10.9	10.79	913	$3.71^{+0.19}_{-0.15}$	$9.74^{+0.83}_{-0.66}$	$0.097^{+0.002}_{-0.002}$	$1.88^{+0.03}_{-0.03}$	
1.78		10.9–11.6	11.03	677	$4.56^{+0.18}_{-0.35}$	$13.41^{+95.65}_{-1.11}$	$0.112^{+0.002}_{-0.007}$	$2.01^{+0.77}_{-0.03}$	
2.0–2.5		2.19	10.1–10.3	10.19	1310	$1.39^{+0.06}_{-0.06}$	$2.72^{+0.40}_{-0.42}$	$0.081^{+0.001}_{-0.002}$	$1.59^{+0.05}_{-0.06}$
	2.18	10.3–10.5	10.40	969	$1.93^{+0.15}_{-0.20}$	$4.05^{+0.55}_{-0.51}$	$0.096^{+0.004}_{-0.000}$	$1.74^{+0.05}_{-0.05}$	
	2.18	10.5–10.7	10.59	824	$2.83^{+0.15}_{-0.19}$	$6.97^{+0.39}_{-0.62}$	$0.105^{+0.003}_{-0.003}$	$1.94^{+0.03}_{-0.03}$	
	2.20	10.7–10.9	10.79	590	$3.30^{+0.26}_{-0.23}$	$7.40^{+0.62}_{-0.61}$	$0.122^{+0.002}_{-0.002}$	$1.96^{+0.03}_{-0.03}$	
	2.19	10.9–11.6	11.02	478	$5.94^{+0.41}_{-0.25}$	$14.17^{+1.36}_{-1.16}$	$0.135^{+0.004}_{-0.003}$	$2.20^{+0.03}_{-0.03}$	
2.5–3.0	2.66	10.1–10.3	10.19	1332	$1.27^{+0.07}_{-0.09}$	$3.80^{+1.05}_{-0.87}$	$0.080^{+0.002}_{-0.001}$	$1.88^{+0.09}_{-0.10}$	
	2.66	10.3–10.5	10.40	925	$1.62^{+0.07}_{-0.10}$	$6.41^{+2.02}_{-1.76}$	$0.098^{+0.001}_{-0.001}$	$2.07^{+0.10}_{-0.12}$	
	2.67	10.5–10.7	10.60	646	$2.33^{+0.19}_{-0.20}$	$6.79^{+1.01}_{-0.81}$	$0.115^{+0.002}_{-0.002}$	$2.09^{+0.05}_{-0.05}$	
	2.68	10.7–10.9	10.80	363	$3.80^{+0.30}_{-0.38}$	$9.09^{+5.77}_{-1.11}$	$0.158^{+0.002}_{-0.002}$	$2.20^{+0.18}_{-0.05}$	
	2.67	10.9–11.6	11.05	280	$6.92^{+0.35}_{-0.29}$	$14.08^{+1.19}_{-1.31}$	$0.174^{+0.002}_{-0.002}$	$2.36^{+0.03}_{-0.04}$	
3.0–4.0	3.37	10.3–10.5	10.39	659	$1.49^{+0.13}_{-0.10}$	$3.30^{+0.69}_{-0.57}$	$0.113^{+0.001}_{-0.002}$	$2.01^{+0.07}_{-0.07}$	

Table F1
(Continued)

Δz_p	$\langle z_p \rangle$	$\Delta \log(M_*)$ $\log(M_\odot)$	$\langle \log(M_*) \rangle$ $\log(M_\odot)$	N_{obj}	S_p ($\mu\text{Jy}/\text{beam}$)	S_r (μJy)	rms ($\mu\text{Jy}/\text{beam}$)	$\log(\text{SFR})$ $\log(M_\odot \text{ yr}^{-1})$
	3.36	10.5–10.7	10.58	399	$1.80^{+0.34}_{-0.14}$	$5.20^{+0.91}_{-0.95}$	$0.148^{+0.003}_{-0.005}$	$2.18^{+0.06}_{-0.07}$
	3.31	10.7–10.9	10.78	161	$2.58^{+0.35}_{-0.50}$	$7.53^{+1.42}_{-1.46}$	$0.234^{+0.002}_{-0.003}$	$2.30^{+0.06}_{-0.08}$
	3.28	10.9–11.6	11.05	140	$4.79^{+0.52}_{-0.54}$	$9.45^{+2.29}_{-1.31}$	$0.252^{+0.003}_{-0.003}$	$2.38^{+0.08}_{-0.05}$
4.0–6.0	4.52	10.3–10.5	10.39	126	$0.96^{+0.42}_{-0.13}$	$3.26^{+7.63}_{-2.14}$	$0.258^{+0.003}_{-0.000}$	$2.24^{+0.44}_{-0.39}$
	4.56	10.5–10.7	10.57	65	$0.83^{+0.39}_{-0.80}$	$7.57^{+8.47}_{-3.73}$	$0.357^{+0.001}_{-0.002}$	$2.55^{+0.28}_{-0.25}$
	4.59	10.7–10.9	10.80	38	$2.54^{+0.79}_{-0.40}$	$3.93^{+1.83}_{-2.15}$	$0.466^{+0.007}_{-0.005}$	$2.32^{+0.14}_{-0.29}$
	4.57	10.9–11.6	11.23	60	$4.15^{+1.37}_{-0.92}$	$9.25^{+2.30}_{-2.65}$	$0.371^{+0.005}_{-0.004}$	$2.63^{+0.08}_{-0.12}$

Note. S_p is peak flux and S_r is integrated flux from our mean stacked images, and their errors are from bootstrapping. In some of the low-mass stack, a good fit for the integrated flux could not be obtained, so these values were removed.

Table F2
3 GHz Stacking Results for All Mass-selected Galaxies Where Our Sample Is Mass-complete









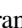





Δz_p	$\langle z_p \rangle$	$\Delta \log(M_*)$ $\log(M_\odot)$	$\langle \log(M_*) \rangle$ $\log(M_\odot)$	N_{obj}	S_p ($\mu\text{Jy}/\text{beam}$)	S_r (μJy)	rms ($\mu\text{Jy}/\text{beam}$)	$\log(\text{SFR})$ $\log(M_\odot \text{ yr}^{-1})$
0.3–0.5	0.39	8.6–9.0	8.79	3786	$0.24^{+0.05}_{-0.06}$	$2.80^{+5.10}_{-2.11}$	$0.048^{+0.000}_{-0.000}$	$0.15^{+0.38}_{-0.52}$
	0.39	9.0–9.4	9.18	2794	$0.47^{+0.08}_{-0.06}$	$3.00^{+4.66}_{-1.27}$	$0.055^{+0.001}_{-0.001}$	$0.16^{+1.85}_{-0.20}$
	0.38	9.4–9.7	9.54	1507	$1.09^{+0.05}_{-0.08}$	$5.31^{+1.13}_{-0.84}$	$0.077^{+0.002}_{-0.002}$	$0.36^{+0.07}_{-0.06}$
	0.38	9.7–9.9	9.80	806	$1.53^{+0.14}_{-0.18}$	$7.88^{+1.25}_{-1.25}$	$0.107^{+0.000}_{-0.001}$	$0.50^{+0.05}_{-0.06}$
	0.38	9.9–10.1	10.00	677	$2.01^{+0.13}_{-0.16}$	$15.36^{+22.21}_{-7.25}$	$0.112^{+0.000}_{-0.002}$	$0.75^{+0.33}_{-0.23}$
	0.38	10.1–10.3	10.20	616	$2.57^{+0.29}_{-0.27}$	$13.25^{+4.24}_{-1.51}$	$0.120^{+0.002}_{-0.002}$	$0.70^{+0.10}_{-0.04}$
	0.38	10.3–10.5	10.40	549	$2.54^{+0.16}_{-0.20}$	$13.47^{+1.58}_{-1.56}$	$0.131^{+0.002}_{-0.004}$	$0.70^{+0.04}_{-0.05}$
	0.38	10.5–10.7	10.60	446	$2.35^{+0.15}_{-0.14}$	$12.91^{+1.87}_{-1.42}$	$0.141^{+0.002}_{-0.001}$	$0.69^{+0.05}_{-0.04}$
	0.39	10.7–10.9	10.80	322	$2.92^{+0.36}_{-0.20}$	$14.97^{+2.08}_{-2.18}$	$0.166^{+0.001}_{-0.001}$	$0.76^{+0.05}_{-0.06}$
	0.39	10.9–11.6	11.05	310	$2.97^{+0.24}_{-0.24}$	$12.19^{+2.18}_{-1.72}$	$0.170^{+0.001}_{-0.001}$	$0.69^{+0.06}_{-0.06}$
0.5–0.8	0.68	9.0–9.4	9.18	6965	$0.44^{+0.03}_{-0.03}$	$2.03^{+1.53}_{-0.71}$	$0.035^{+0.001}_{-0.000}$	$0.49^{+0.21}_{-0.16}$
	0.67	9.4–9.7	9.54	3612	$0.84^{+0.09}_{-0.06}$	$3.54^{+0.88}_{-0.41}$	$0.049^{+0.000}_{-0.000}$	$0.69^{+0.08}_{-0.05}$
	0.67	9.7–9.9	9.80	1833	$1.31^{+0.07}_{-0.13}$	$5.67^{+0.77}_{-0.74}$	$0.070^{+0.001}_{-0.002}$	$0.86^{+0.05}_{-0.05}$
	0.67	9.9–10.1	10.00	1545	$1.85^{+0.07}_{-0.09}$	$7.37^{+0.92}_{-0.62}$	$0.076^{+0.002}_{-0.000}$	$0.96^{+0.04}_{-0.03}$
	0.67	10.1–10.3	10.20	1371	$2.59^{+0.17}_{-0.12}$	$8.59^{+0.65}_{-0.72}$	$0.081^{+0.001}_{-0.001}$	$1.01^{+0.03}_{-0.03}$
	0.67	10.3–10.5	10.40	1204	$2.13^{+0.16}_{-0.11}$	$9.17^{+0.68}_{-0.80}$	$0.086^{+0.001}_{-0.000}$	$1.04^{+0.03}_{-0.03}$
	0.67	10.5–10.7	10.60	1031	$2.64^{+0.16}_{-0.20}$	$11.27^{+1.17}_{-0.94}$	$0.092^{+0.001}_{-0.002}$	$1.12^{+0.04}_{-0.03}$
	0.68	10.7–10.9	10.80	810	$2.44^{+0.23}_{-0.14}$	$9.99^{+1.14}_{-1.01}$	$0.109^{+0.003}_{-0.001}$	$1.08^{+0.04}_{-0.04}$
	0.68	10.9–11.6	11.05	758	$2.38^{+0.18}_{-0.25}$	$10.54^{+3.43}_{-1.54}$	$0.109^{+0.002}_{-0.000}$	$1.10^{+0.10}_{-0.06}$
0.8–1.1	0.94	9.0–9.4	9.19	9127	$0.38^{+0.03}_{-0.03}$...	$0.031^{+0.001}_{-0.001}$...
	0.94	9.4–9.7	9.54	5188	$0.76^{+0.05}_{-0.05}$	$11.53^{+112.05}_{-9.46}$	$0.041^{+0.001}_{-0.001}$	$1.42^{+0.87}_{-0.63}$
	0.94	9.7–9.9	9.80	2751	$1.22^{+0.08}_{-0.05}$	$3.50^{+0.70}_{-0.44}$	$0.057^{+0.002}_{-0.003}$	$0.97^{+0.07}_{-0.05}$
	0.94	9.9–10.1	9.99	2335	$1.65^{+0.04}_{-0.08}$	$4.91^{+0.63}_{-0.56}$	$0.060^{+0.000}_{-0.001}$	$1.10^{+0.04}_{-0.04}$
	0.93	10.1–10.3	10.20	2053	$1.93^{+0.05}_{-0.11}$	$6.73^{+0.59}_{-0.58}$	$0.065^{+0.001}_{-0.001}$	$1.21^{+0.03}_{-0.03}$
	0.93	10.3–10.5	10.40	1852	$2.27^{+0.13}_{-0.14}$	$7.80^{+0.62}_{-0.40}$	$0.069^{+0.001}_{-0.001}$	$1.26^{+0.03}_{-0.02}$
	0.93	10.5–10.7	10.60	1623	$2.21^{+0.10}_{-0.07}$	$8.16^{+1.17}_{-0.77}$	$0.071^{+0.001}_{-0.002}$	$1.28^{+0.05}_{-0.04}$
	0.92	10.7–10.9	10.80	1230	$2.25^{+0.09}_{-0.09}$	$8.83^{+0.72}_{-0.80}$	$0.084^{+0.001}_{-0.001}$	$1.30^{+0.03}_{-0.03}$
	0.92	10.9–11.6	11.05	1226	$2.45^{+0.15}_{-0.14}$	$10.32^{+1.11}_{-0.94}$	$0.084^{+0.002}_{-0.001}$	$1.36^{+0.04}_{-0.03}$
1.1–1.5	1.29	9.4–9.7	9.54	6912	$0.61^{+0.05}_{-0.03}$	$1.45^{+0.18}_{-0.22}$	$0.036^{+0.000}_{-0.000}$	$0.92^{+0.04}_{-0.06}$
	1.29	9.7–9.9	9.80	3567	$1.02^{+0.03}_{-0.05}$	$2.51^{+0.35}_{-0.27}$	$0.050^{+0.000}_{-0.000}$	$1.12^{+0.05}_{-0.04}$
	1.28	9.9–10.1	9.99	2923	$1.47^{+0.10}_{-0.06}$	$3.97^{+1.01}_{-0.56}$	$0.055^{+0.000}_{-0.000}$	$1.28^{+0.08}_{-0.06}$
	1.29	10.1–10.3	10.19	2527	$1.76^{+0.07}_{-0.05}$	$5.10^{+0.51}_{-0.35}$	$0.058^{+0.001}_{-0.001}$	$1.39^{+0.03}_{-0.03}$
	1.30	10.3–10.5	10.40	2035	$2.10^{+0.09}_{-0.08}$	$6.57^{+0.66}_{-0.46}$	$0.066^{+0.000}_{-0.000}$	$1.48^{+0.04}_{-0.03}$
	1.28	10.5–10.7	10.60	1829	$2.11^{+0.10}_{-0.06}$	$7.54^{+1.26}_{-0.63}$	$0.069^{+0.001}_{-0.001}$	$1.52^{+0.06}_{-0.03}$
	1.28	10.7–10.9	10.80	1396	$2.38^{+0.13}_{-0.13}$	$8.20^{+0.53}_{-0.61}$	$0.079^{+0.001}_{-0.001}$	$1.55^{+0.02}_{-0.03}$
	1.27	10.9–11.6	11.05	1252	$2.91^{+0.29}_{-0.24}$	$11.45^{+1.19}_{-1.19}$	$0.084^{+0.002}_{-0.002}$	$1.67^{+0.04}_{-0.04}$

Table F2
(Continued)

Δz_p	$\langle z_p \rangle$	$\Delta \log(M_*)$ $\log(M_\odot)$	$\langle \log(M_*) \rangle$ $\log(M_\odot)$	N_{obj}	S_p ($\mu\text{Jy}/\text{beam}$)	S_t (μJy)	rms ($\mu\text{Jy}/\text{beam}$)	$\log(\text{SFR})$ $\log(M_\odot \text{ yr}^{-1})$
1.5–2.0	1.75	9.9–10.1	9.99	3136	$1.15^{+0.07}_{-0.05}$	$2.79^{+0.31}_{-0.32}$	$0.052^{+0.000}_{-0.000}$	$1.42^{+0.04}_{-0.05}$
	1.75	10.1–10.3	10.19	2621	$1.55^{+0.04}_{-0.09}$	$4.52^{+0.64}_{-0.49}$	$0.058^{+0.001}_{-0.000}$	$1.59^{+0.05}_{-0.04}$
	1.75	10.3–10.5	10.39	2142	$2.13^{+0.09}_{-0.10}$	$6.33^{+0.60}_{-0.39}$	$0.065^{+0.001}_{-0.001}$	$1.72^{+0.03}_{-0.02}$
	1.74	10.5–10.7	10.59	1692	$2.56^{+0.10}_{-0.11}$	$7.11^{+0.51}_{-0.46}$	$0.071^{+0.001}_{-0.001}$	$1.76^{+0.03}_{-0.02}$
	1.73	10.7–10.9	10.79	1286	$2.62^{+0.14}_{-0.12}$	$7.97^{+0.56}_{-0.60}$	$0.083^{+0.000}_{-0.001}$	$1.79^{+0.02}_{-0.03}$
	1.73	10.9–11.6	11.04	1169	$2.85^{+0.19}_{-0.21}$	$10.01^{+25.11}_{-0.70}$	$0.088^{+0.001}_{-0.000}$	$1.88^{+0.46}_{-0.03}$
2.0–2.5	2.19	10.1–10.3	10.19	1353	$1.37^{+0.06}_{-0.08}$	$3.08^{+0.61}_{-0.52}$	$0.080^{+0.001}_{-0.002}$	$1.64^{+0.07}_{-0.07}$
	2.18	10.3–10.5	10.40	1024	$1.81^{+0.12}_{-0.12}$	$4.31^{+0.64}_{-0.51}$	$0.093^{+0.004}_{-0.001}$	$1.76^{+0.05}_{-0.05}$
	2.19	10.5–10.7	10.60	902	$2.65^{+0.21}_{-0.15}$	$7.35^{+0.84}_{-0.68}$	$0.101^{+0.002}_{-0.001}$	$1.96^{+0.04}_{-0.04}$
	2.21	10.7–10.9	10.79	663	$2.91^{+0.20}_{-0.19}$	$7.62^{+0.66}_{-0.71}$	$0.116^{+0.002}_{-0.002}$	$1.98^{+0.03}_{-0.04}$
	2.20	10.9–11.6	11.03	582	$4.68^{+0.23}_{-0.36}$	$13.92^{+1.52}_{-1.24}$	$0.121^{+0.002}_{-0.001}$	$2.20^{+0.04}_{-0.03}$
2.5–3.0	2.66	10.1–10.3	10.19	1353	$1.26^{+0.07}_{-0.08}$	$4.29^{+1.10}_{-0.92}$	$0.080^{+0.002}_{-0.000}$	$1.92^{+0.08}_{-0.09}$
	2.66	10.3–10.5	10.40	963	$1.59^{+0.08}_{-0.10}$	$6.94^{+1.93}_{-1.89}$	$0.095^{+0.001}_{-0.001}$	$2.10^{+0.09}_{-0.12}$
	2.67	10.5–10.7	10.60	701	$2.17^{+0.25}_{-0.22}$	$6.89^{+0.99}_{-0.87}$	$0.111^{+0.003}_{-0.003}$	$2.09^{+0.05}_{-0.05}$
	2.68	10.7–10.9	10.80	409	$3.53^{+0.61}_{-0.20}$	$9.40^{+1.65}_{-0.88}$	$0.150^{+0.003}_{-0.001}$	$2.21^{+0.06}_{-0.04}$
	2.67	10.9–11.6	11.05	326	$5.75^{+0.39}_{-0.38}$	$14.04^{+1.21}_{-1.18}$	$0.163^{+0.004}_{-0.002}$	$2.36^{+0.03}_{-0.03}$
3.0–4.0	3.37	10.3–10.5	10.39	664	$1.49^{+0.12}_{-0.09}$	$3.84^{+0.58}_{-0.60}$	$0.113^{+0.001}_{-0.002}$	$2.07^{+0.05}_{-0.06}$
	3.36	10.5–10.7	10.58	412	$1.76^{+0.37}_{-0.13}$	$5.64^{+1.15}_{-0.95}$	$0.145^{+0.003}_{-0.004}$	$2.21^{+0.07}_{-0.07}$
	3.32	10.7–10.9	10.78	186	$2.40^{+0.22}_{-0.28}$	$8.43^{+1.21}_{-1.76}$	$0.218^{+0.003}_{-0.003}$	$2.34^{+0.05}_{-0.09}$
	3.31	10.9–11.6	11.06	159	$4.52^{+0.52}_{-0.29}$	$10.45^{+1.66}_{-1.88}$	$0.237^{+0.002}_{-0.003}$	$2.42^{+0.05}_{-0.07}$
4.0–6.0	4.51	10.3–10.5	10.39	129	$0.95^{+0.51}_{-0.17}$	$3.23^{+13.29}_{-2.04}$	$0.254^{+0.001}_{-0.001}$	$2.23^{+0.60}_{-0.37}$
	4.56	10.5–10.7	10.57	69	$0.76^{+0.29}_{-0.74}$	$9.21^{+14.79}_{-3.83}$	$0.348^{+0.003}_{-0.002}$	$2.63^{+0.35}_{-0.20}$
	4.62	10.7–10.9	10.80	39	$2.39^{+0.99}_{-0.72}$	$4.39^{+3.36}_{-2.57}$	$0.465^{+0.007}_{-0.005}$	$2.36^{+0.21}_{-0.32}$
	4.53	10.9–11.6	11.20	71	$3.11^{+0.79}_{-1.04}$	$9.19^{+3.34}_{-2.12}$	$0.345^{+0.007}_{-0.008}$	$2.62^{+0.11}_{-0.10}$

Note. See Table F1 for more details.

ORCID iDs

Sarah K. Leslie  <https://orcid.org/0000-0002-4826-8642>
 Eva Schinnerer  <https://orcid.org/0000-0002-3933-7677>
 Daizhong Liu  <https://orcid.org/0000-0001-9773-7479>
 Benjamin Magnelli  <https://orcid.org/0000-0002-6777-6490>
 Alexander Karim  <https://orcid.org/0000-0002-8414-9579>
 Iary Davidzon  <https://orcid.org/0000-0002-2951-7519>
 Philipp Lang  <https://orcid.org/0000-0002-5681-3575>
 Mark T. Sargent  <https://orcid.org/0000-0003-1033-9684>
 Mladen Novak  <https://orcid.org/0000-0001-8695-825X>
 Brent Groves  <https://orcid.org/0000-0002-9768-0246>
 Vernesa Smolčić  <https://orcid.org/0000-0002-3893-8614>
 Giovanni Zamorani  <https://orcid.org/0000-0002-2318-301X>
 Mattia Vaccari  <https://orcid.org/0000-0002-6748-0577>
 Andrew Battisti  <https://orcid.org/0000-0003-4569-2285>
 Jeyhan Kartaltepe  <https://orcid.org/0000-0001-9187-3605>

References

- Abramson, L. E., Kelson, D. D., Dressler, A., et al. 2014, *ApJL*, 785, L36
 Amblard, A., Cooray, A., Serra, P., et al. 2011, *Natur*, 470, 510
 Appleton, P. N., Fadda, D. T., Marleau, F. R., et al. 2004, *ApJS*, 154, 147
 Arnouts, S., Cristiani, S., Moscardini, L., et al. 1999, *MNRAS*, 310, 540
 Arnouts, S., Cristiani, S., Moscardini, L., et al. 2007, *A&A*, 476, 137
 Assef, R. J., Stern, D., Kochanek, C. S., et al. 2013, *ApJ*, 772, 26
 Astropy Collaboration, Robitaille, T. P., Tollerud, E. J., et al. 2013, *A&A*, 558, A33
 Auremma, C., Perola, G. C., Ekers, R. D., et al. 1977, *A&A*, 57, 41
 Baldry, I. K., Balogh, M. L., Bower, R. G., et al. 2006, *MNRAS*, 373, 469
 Baldry, I. K., Glazebrook, K., Brinkmann, J., et al. 2004, *ApJ*, 600, 681
 Balogh, M. L., Schade, D., Morris, S. L., et al. 1998, *ApJL*, 504, L75
 Balogh, M. L., Schade, D., Morris, S. L., et al. 2002, *ApJ*, 566, 123
 Barazza, F. D., Jogee, S., & Marinova, I. 2008, *ApJ*, 675, 1194
 Barnes, J. E., & Hernquist, L. 1996, *ApJ*, 471, 115
 Basu, A., Wadadekar, Y., Beelen, A., et al. 2015, *ApJ*, 803, 51
 Bell, E. F. 2003, *ApJ*, 586, 794
 Bell, E. F., Wolf, C., Meisenheimer, K., et al. 2004, *ApJ*, 608, 752
 Bell, E. F., van der Wel, A., Papovich, C., et al. 2012, *ApJ*, 753, 167
 Bendo, G. J., Baes, M., & Bianchi, S. 2015, *MNRAS*, 448, 13
 Béthermin, M., Wang, L., Doré, O., et al. 2013, *A&A*, 557, A66
 Birnboim, Y., Dekel, A., & Neistein, E. 2007, *MNRAS*, 380, 339
 Bisigello, L., Caputi, K. I., Grogin, N., & Koekemoer, A. 2018, *A&A*, 609, A82
 Blain, A. W., Smail, I., Ivison, R. J., & Kneib, J. P. 1999, *MNRAS*, 302, 632
 Bluck, A. F. L., Mendel, J. T., Ellison, S. L., et al. 2014, *MNRAS*, 441, 599
 Bondi, M., Zamorani, G., Ciliegi, P., et al. 2018, *A&A*, 618, L8
 Boogaard, L. A., Brinchmann, J., Bouche, N., et al. 2018, *A&A*, 619, A27
 Boselli, A., Fossati, M., Gavazzi, G., et al. 2015, *A&A*, 579, A102
 Bouwens, R. J., Aravena, M., Decarli, R., et al. 2016, *ApJ*, 833, 72
 Bouwens, R. J., Bradley, L., Zitrin, A., et al. 2014, *ApJ*, 795, 126
 Bouwens, R. J., Illingworth, G. D., Oesch, P. A., et al. 2015, *ApJ*, 803, 34
 Bowler, R. A. A., Bourne, N., Dunlop, J. S., McLure, R. J., & McLeod, D. J. 2018, *MNRAS*, 481, 1631
 Brammer, G. B., Whitaker, K. E., van Dokkum, P. G., et al. 2011, *ApJ*, 739, 24
 Brinchmann, J., Charlot, S., White, S. D. M., et al. 2004, *MNRAS*, 351, 1151
 Brown, M. J. I., Dey, A., Jannuzi, B. T., et al. 2007, *ApJ*, 654, 858
 Brown, M. J. I., Jannuzi, B. T., Floyd, D. J. E., & Mould, J. R. 2011, *ApJL*, 731, L41
 Brown, M. J. I., Moustakas, J., Kennicutt, R. C., et al. 2017, *ApJ*, 847, 136
 Brown, M. J. I., Webster, R. L., & Boyle, B. J. 2001, *AJ*, 121, 2381

- Bruzual, G., & Charlot, S. 2003, *MNRAS*, 344, 1000
- Buisson, D. J. K., Lohfink, A. M., Alston, W. N., & Fabian, A. C. 2017, *MNRAS*, 464, 3194
- Bundy, K., Ellis, R. S., Conselice, C. J., et al. 2006, *ApJ*, 651, 120
- Burgarella, D., Buat, V., & Iglesias-Páramo, J. 2005, *MNRAS*, 360, 1413
- Calistro Rivera, G., Williams, W. L., Hardcastle, M. J., et al. 2017, *MNRAS*, 469, 3468
- Camps, P., Trčka, A., Trayford, J., et al. 2018, *ApJS*, 234, 20
- Capak, P., Aussel, H., Ajiki, M., et al. 2007, *ApJS*, 172, 99
- Caplar, N., & Tacchella, S. 2019, arXiv:1901.07556
- Caputi, K. I., Deshmukh, S., Ashby, M. L. N., et al. 2017, *ApJ*, 849, 45
- Casey, C. M., Zavala, J. A., Spilker, J., et al. 2018, *ApJ*, 862, 77
- Castellano, M., Fontana, A., Grazian, A., et al. 2012, *A&A*, 540, A39
- Cattaneo, A., Dekel, A., Devriendt, J., Guiderdoni, B., & Blaizot, J. 2006, *MNRAS*, 370, 1651
- Cavanaugh, J. E., & Shumway, R. H. 1997, *Statistica Sinica*, 7, 473
- Chabrier, G. 2003, *PASP*, 115, 763
- Chary, R., & Elbaz, D. 2001, *ApJ*, 556, 562
- Cibinel, A., Daddi, E., Sargent, M. T., et al. 2019, *MNRAS*, 485, 5631
- Condon, J. J. 1992, *ARA&A*, 30, 575
- Condon, J. J., Cotton, W. D., & Broderick, J. J. 2002, *AJ*, 124, 675
- Connolly, A. J., Szalay, A. S., Dickinson, M., SubbaRao, M. U., & Brunner, R. J. 1997, *ApJL*, 486, L11
- Cooper, M. C., Newman, J. A., Croton, D. J., et al. 2006, *MNRAS*, 370, 198
- Coaray, A., Amblard, A., Wang, L., et al. 2010, *A&A*, 518, L22
- Couch, W. J., Balogh, M. L., Bower, R. G., et al. 2001, *ApJ*, 549, 820
- Cowie, L. L., Songaila, A., & Barger, A. J. 1999, *AJ*, 118, 603
- Cowie, L. L., Songaila, A., Hu, E. M., & Cohen, J. G. 1996, *AJ*, 112, 839
- Daddi, E., Dickinson, M., Morrison, G., et al. 2007, *ApJ*, 670, 156
- Darvish, B., Mobasher, B., Sobral, D., Scoville, N., & Aragon-Calvo, M. 2015, *ApJ*, 805, 121
- Darvish, B., Mobasher, B., Sobral, D., et al. 2016, *ApJ*, 825, 113
- Darvish, B., Sobral, D., Mobasher, B., et al. 2014, *ApJ*, 796, 51
- Davé, R., Thompson, R., & Hopkins, P. F. 2016, *MNRAS*, 462, 3265
- Davidzon, I., Ilbert, O., Faisst, A. L., Sparre, M., & Capak, P. L. 2018, *ApJ*, 852, 107
- Davidzon, I., Ilbert, O., Laigle, C., et al. 2017, *A&A*, 605, A70
- Davies, L. J. M., Driver, S. P., Robotham, A. S. G., et al. 2016, *MNRAS*, 461, 458
- Davies, L. J. M., Huynh, M. T., Hopkins, A. M., et al. 2017, *MNRAS*, 466, 2312
- Davies, L. J. M., Lagos, C. d. P., Katsianis, A., et al. 2019, *MNRAS*, 483, 1881
- Dekel, A., & Birnboim, Y. 2006, *MNRAS*, 368, 2
- Dekel, A., & Birnboim, Y. 2008, *MNRAS*, 383, 119
- Delhaize, J., Smolcic, V., Delvecchio, I., et al. 2017, *A&A*, 602, A4
- Delvecchio, I., Smolcic, V., Zamorani, G., et al. 2017, *A&A*, 602, A3
- Donley, J. L., Koekemoer, A. M., Brusa, M., et al. 2012, *ApJ*, 748, 142
- Donnari, M., Pillepich, A., Nelson, D., et al. 2019, *MNRAS*, 485, 4817
- Dressler, A. 1980, *ApJ*, 236, 351
- Driver, S. P., Andrews, S. K., da Cunha, E., et al. 2018, *MNRAS*, 475, 2891
- Duivendoorn, S., Oliver, S., Buat, V., et al. 2016, *MNRAS*, 462, 277
- Eales, S., Smith, D., Bourne, N., et al. 2018a, *MNRAS*, 473, 3507
- Eales, S. A., Baes, M., Bourne, N., et al. 2018b, *MNRAS*, 481, 1183
- Elbaz, D., Daddi, E., Le Borgne, D., et al. 2007, *A&A*, 468, 33
- Elitzur, M., Ho, L. C., & Trump, J. R. 2014, *MNRAS*, 438, 3340
- Erfanianfar, G., Popesso, P., Finoguenov, A., et al. 2016, *MNRAS*, 455, 2839
- Fabbiano, G., Gioia, I. M., & Trinchieri, G. 1989, *ApJ*, 347, 127
- Faber, S. M., Willmer, C. N. A., Wolf, C., et al. 2007, *ApJ*, 665, 265
- Faucher-Giguère, C.-A., Kereš, D., & Ma, C.-P. 2011, *MNRAS*, 417, 2982
- Filho, M. E., Tabatabaei, F. S., Sánchez Almeida, J., Muñoz-Tuñón, C., & Elmegreen, B. G. 2019, *MNRAS*, 484, 543
- Finoguenov, A., Guzzo, L., Hasinger, G., et al. 2007, *ApJS*, 172, 182
- Flores, H., Hammer, F., Thuan, T. X., et al. 1999, *ApJ*, 517, 148
- Foreman-Mackey, D. 2016, *JOSS*, 1, 24
- Fragkoudi, F., Athanassoula, E., & Bosma, A. 2016, *MNRAS*, 462, L41
- Franx, M., van Dokkum, P. G., Förster Schreiber, N. M., et al. 2008, *ApJ*, 688, 770
- Fudamoto, Y., Oesch, P. A., Schinnerer, E., et al. 2017, *MNRAS*, 472, 483
- Gallego, J., Zamorano, J., Aragon-Salamanca, A., & Rego, M. 1995, *ApJL*, 455, L1
- Garrett, M. A. 2002, *A&A*, 384, L19
- Gavazzi, G., Consolandi, G., Dotti, M., et al. 2015, *A&A*, 580, A116
- Gensior, J., Kruijssen, J. M. D., & Keller, B. W. 2020, arXiv:2002.01484
- George, M. R., Leauthaud, A., Bundy, K., et al. 2011, *ApJ*, 742, 125
- Gómez, P. L., Nichol, R. C., Miller, C. J., et al. 2003, *ApJ*, 584, 210
- Gozalias, G., Finoguenov, A., Tanaka, M., et al. 2019, *MNRAS*, 483, 3545
- Grazian, A., Fontana, A., Santini, P., et al. 2015, *A&A*, 575, A96
- Grossi, M., Fernandes, C. A. C., Sobral, D., et al. 2018, *MNRAS*, 475, 735
- Gu, Y., Fang, G., Yuan, Q., Cai, Z., & Wang, T. 2018, *ApJ*, 855, 10
- Guo, K., Zheng, X. Z., & Fu, H. 2013, *ApJ*, 778, 23
- Gürkan, G., Hardcastle, M. J., Smith, D. J. B., et al. 2018, *MNRAS*, 475, 3010
- Haarsma, D. B., Partridge, R. B., Windhorst, R. A., & Richards, E. A. 2000, *ApJ*, 544, 641
- Haggard, D., Green, P. J., Anderson, S. F., et al. 2010, *ApJ*, 723, 1447
- Hahn, C., Starkeburg, T. K., Choi, E., et al. 2019, *ApJ*, 872, 160
- Haines, C. P., Pereira, M. J., Smith, G. P., et al. 2013, *ApJ*, 775, 126
- Hales, C. A., Murphy, T., Curran, J. R., et al. 2012, *MNRAS*, 425, 979
- Hashimoto, Y., Oemler Augustus, J., Lin, H., & Tucker, D. L. 1998, *ApJ*, 499, 589
- Heckman, T. M., & Best, P. N. 2014, *ARA&A*, 52, 589
- Helou, G., Lu, N. Y., Werner, M. W., Malhotra, S., & Silvermann, N. 2000, *ApJL*, 532, L21
- Helou, G., Soifer, B. T., & Rowan-Robinson, M. 1985, *ApJL*, 298, L7
- Herrera Ruiz, N., Middleberg, E., Deller, A., et al. 2018, *A&A*, 616, A128
- Hindson, L., Kitchener, G., Brinks, E., et al. 2018, *ApJS*, 234, 29
- Hinshaw, G., Larson, D., Komatsu, E., et al. 2013, *ApJS*, 208, 19
- Hogg, D. W., Blanton, M. R., Brinchmann, J., et al. 2004, *ApJL*, 601, L29
- Hopkins, A. M., Miller, C. J., Nichol, R. C., et al. 2003, *ApJ*, 599, 971
- Hunter, J. D. 2007, *CSE*, 9, 90
- Hurvich, C., & Tsai, C.-L. 1989, *Biometrika*, 76, 297
- Ilbert, O., Arnouts, S., Le Floch, E., et al. 2015, *A&A*, 579, A2
- Ilbert, O., Capak, P., Salvato, M., et al. 2009, *ApJ*, 690, 1236
- Ilbert, O., McCracken, H. J., Le Fevre, O., et al. 2013, *A&A*, 556, A55
- Ilbert, O., Salvato, M., Le Floch, E., et al. 2010, *ApJ*, 709, 644
- Iverson, R. J., Alexander, D. M., Biggs, A. D., et al. 2010a, *MNRAS*, 402, 245
- Iverson, R. J., Magnelli, B., Ibar, E., et al. 2010b, *A&A*, 518, L31
- Iyer, K., Gawiser, E., Dave, R., et al. 2018, *ApJ*, 866, 120
- Jarrett, T. H., Cohen, M., Masci, F., et al. 2011, *ApJ*, 735, 112
- Jiménez-Andrade, E. F., et al. 2019, *A&A*, 625, A114
- Johnston, R., Vaccari, M., Jarvis, M., et al. 2015, *MNRAS*, 453, 2540
- Karim, A., Schinnerer, E., Martnez-Sansigre, A., et al. 2011, *ApJ*, 730, 61
- Kartaltepe, J. S., Sanders, D. B., Le Floch, E., et al. 2010a, *ApJ*, 709, 572
- Kartaltepe, J. S., Sanders, D. B., Le Floch, E., et al. 2010b, *ApJ*, 721, 98
- Katsianis, A., Gonzalez, V., Barrientos, D., et al. 2020, *MNRAS*, 492, 5592
- Kauffmann, G., Heckman, T. M., White, S. D. M., et al. 2003a, *MNRAS*, 341, 33
- Kauffmann, G., Heckman, T. M., White, S. D. M., et al. 2003b, *MNRAS*, 341, 54
- Kennicutt, R. C., & Evans, N. J. 2012, *ARA&A*, 50, 531
- Koekemoer, A. M., Aussel, H., Calzetti, D., et al. 2007, *ApJS*, 172, 196
- Koyama, Y., Kodama, T., Tadaki, K.-i., et al. 2013, *MNRAS*, 434, 423
- Koyama, Y., Kodama, T., Tadaki, K.-i., et al. 2014, *ApJ*, 789, 18
- Kroupa, P. 2001, *MNRAS*, 322, 231
- Lacki, B. C., Thompson, T. A., & Quataert, E. 2010, *ApJ*, 717, 1
- Laigle, C., McCracken, H. J., Ilbert, O., et al. 2016, *ApJS*, 224, 24
- Lang, P., Wuyts, S., Somerville, R. S., et al. 2014, *ApJ*, 788, 11
- Larson, D., Dunkley, J., Hinshaw, G., et al. 2011, *ApJS*, 192, 16
- Leauthaud, A., Finoguenov, A., Kneib, J.-P., et al. 2010, *ApJ*, 709, 97
- Leauthaud, A., Tinker, J., Bundy, K., et al. 2012, *ApJ*, 744, 159
- Lee, B., Giavalisco, M., Whitaker, K., et al. 2018, *ApJ*, 853, 131
- Lee, N., Sanders, D. B., Casey, C. M., et al. 2015, *ApJ*, 801, 80
- Legrand, L., McCracken, H. J., Davidzon, I., et al. 2018, arXiv:1810.10557
- Leroy, A., Bolatto, A. D., Simon, J. D., & Blitz, L. 2005, *ApJ*, 625, 763
- Lilly, S. J., Le Fevre, O., Hammer, F., & Crampton, D. 1996, *ApJL*, 460, L1
- Liu, D., Daddi, E., Dickinson, M., et al. 2018, *ApJ*, 853, 172
- Liu, D., Lang, P., Magnelli, B., et al. 2019a, *ApJS*, 244, 40
- Liu, D., Schinnerer, E., Groves, B., et al. 2019b, *ApJ*, 887, 235
- Livermore, R. C., Finkelstein, S. L., & Lotz, J. M. 2017, *ApJ*, 835, 113
- Madau, P., & Dickinson, M. 2014, *ARA&A*, 52, 415
- Madau, P., Pozzetti, L., & Dickinson, M. 1998, *ApJ*, 498, 106
- Madgwick, D. S. 2003, *MNRAS*, 338, 197
- Magdis, G. E., Rigopoulou, D., Huang, J.-S., & Fazio, G. G. 2010, *MNRAS*, 401, 1521
- Magnelli, B., Iverson, R. J., Lutz, D., et al. 2015, *A&A*, 573, A45
- Magnelli, B., Lutz, D., Saintonge, A., et al. 2014, *A&A*, 561, A86
- Maier, C., Ziegler, B. L., Haines, C. P., & Smith, G. P. 2019, *A&A*, 621, A131
- Mao, M. Y., Huynh, M. T., Norris, R. P., et al. 2011, *ApJ*, 731, 79
- Mateos, S., Alonso-Herrero, A., Carrera, F. J., et al. 2012, *MNRAS*, 426, 3271
- Matthee, J., & Schaye, J. 2019, *MNRAS*, 484, 915
- McCracken, H. J., Capak, P., Salvato, M., et al. 2010, *ApJ*, 708, 202
- McCracken, H. J., Milvang-Jensen, B., Dunlop, J., et al. 2012, *A&A*, 544, A156

- McGee, S. L., Balogh, M. L., Wilman, D. J., et al. 2011, *MNRAS*, **413**, 996
- McPartland, C., Sanders, D. B., Kewley, L. J., & Leslie, S. K. 2019, *MNRAS*, **482**, L129
- Meidt, S. E., Leroy, A. K., Rosolowsky, E., et al. 2018, *ApJ*, **854**, 100
- Mishra, H. D., & Dai, X. 2020, *AJ*, **159**, 69
- Molnár, D. C., Sargent, M. T., & Leslie, S. 2018, *MNRAS*, **475**, 827
- Molnár, D. C., Sargent, M. T., & Leslie, S. 2020, *MNRAS*, in press
- Morić, I., Smolčić, V., Kimball, A., et al. 2010, *ApJ*, **724**, 779
- Moster, B. P., Somerville, R. S., Maulbetsch, C., et al. 2010, *ApJ*, **710**, 903
- Moster, B. P., Somerville, R. S., Newman, J. A., & Rix, H.-W. 2011, *ApJ*, **731**, 113
- Moustakas, J., Coil, A. L., Aird, J., et al. 2013, *ApJ*, **767**, 50
- Mowla, L., van der Wel, A., van Dokkum, P., & Miller, T. B. 2019, *ApJL*, **872**, L13
- Murphy, E. J., Condon, J. J., Schinnerer, E., et al. 2011, *ApJ*, **737**, 67
- Muzzin, A., Machesini, D., Stefanon, M., et al. 2013, *ApJ*, **777**, 18
- Noda, H., & Done, C. 2018, *MNRAS*, **480**, 3898
- Noeske, K. G., Weiner, B. J., Faber, S. M., et al. 2007, *ApJL*, **660**, L43
- Novak, M., Smolčić, V., Schinnerer, E., et al. 2017, *A&A*, **602**, A5
- Novak, M., Smolčić, V., Schinnerer, E., et al. 2018, *A&A*, **614**, A47
- Ocran, E. F., Taylor, A. R., Vaccari, M., et al. 2020, *MNRAS*, **491**, 5911
- Oesch, P. A., Bouwens, R. J., Illingworth, G. D., et al. 2013, *ApJ*, **773**, 75
- Oesch, P. A., Bouwens, R. J., Illingworth, G. D., Labbé, I., & Stefanon, M. 2018, *ApJ*, **855**, 105
- Ogle, P. M., Lanz, L., Nader, C., & Helou, G. 2016, *ApJ*, **817**, 109
- Old, L. J., Balogh, M. L., van der Burg, R. F. J., et al. 2020, *MNRAS*, **493**, 5987
- Paccagnella, A., Vulcani, B., Poggianti, B. M., et al. 2016, *ApJL*, **816**, L25
- Padoan, P., & Nordlund, A. 2002, *ApJ*, **576**, 870
- Paladino, R., Murgia, M., Helfer, T. T., et al. 2006, *A&A*, **456**, 847
- Pannella, M., Carilli, C. L., Daddi, E., et al. 2009a, *ApJL*, **698**, L116
- Pannella, M., Carilli, C. L., Daddi, E., et al. 2009b, *ApJ*, **701**, 787
- Pannella, M., Gabasch, A., Goranova, Y., et al. 2015, *ApJ*, **807**, 141
- Parkash, V., Brown, M. J. I., Jarrett, T. H., & Bonne, N. J. 2018, *ApJ*, **864**, 40
- Pascarella, S. M., Lanzetta, K. M., & Fernández-Soto, A. 1998, *ApJL*, **508**, L1
- Paulino-Afonso, A., Sobral, D., Darvish, B., et al. 2019, *A&A*, **630**, A57
- Pearson, W. J., Wang, L., Hurley, P. D., et al. 2018, *A&A*, **615**, A146
- Peng, Y.-j., Lilly, S. J., Renzini, A., & Carollo, M. 2010, *ApJ*, **721**, 193
- Peng, Y.-j., Lilly, S. J., Renzini, A., & Carollo, M. 2012, *ApJ*, **757**, 4
- Pharo, J., Malhotra, S., Rhoads, J. E., et al. 2020, *ApJ*, **888**, 79
- Popesso, P., Biviano, A., Finoguenov, A., et al. 2015, *ApA*, **579**, A132
- Popesso, P., Concas, A., Morselli, L., et al. 2019a, *MNRAS*, **483**, 3213
- Popesso, P., Morselli, L., Concas, A., et al. 2019b, *MNRAS*, **490**, 5285
- Pozzetti, L., Bolzonella, M., Zucca, E., et al. 2010, *A&A*, **523**, A13
- Renzini, A. 2016, *MNRAS*, **460**, L45
- Renzini, A., & Peng, Y.-j. 2015, *ApJL*, **801**, L29
- Ricciardelli, E., Cava, A., Varela, J., & Quilis, V. 2014, *MNRAS*, **445**, 4045
- Rodighiero, G., Cimatti, A., Gruppioni, C., et al. 2010, *A&A*, **518**, L25
- Rodighiero, G., Daddi, E., Baronchelli, I., et al. 2011, *ApJL*, **739**, L40
- Rodighiero, G., Renzini, A., Daddi, E., et al. 2014, *MNRAS*, **443**, 19
- Rodríguez-Muñoz, L., Rodighiero, G., Mancini, C., et al. 2019, *MNRAS*, **485**, 586
- Sabater, J., Best, P. N., Hardcastle, M. J., et al. 2019, *A&A*, **622**, A17
- Sadler, E. M. 1982, *PASAu*, **4**, 454
- Saintonge, A., Catinella, B., Cortese, L., et al. 2016, *MNRAS*, **462**, 1749
- Salim, S., Lee, J. C., Janowiecki, S., et al. 2016, *ApJS*, **227**, 2
- Santini, P., Fontana, A., Castellano, M., et al. 2017, *ApJ*, **847**, 76
- Sargent, M. T., Bethermin, M., Daddi, E., & Elbaz, D. 2007, *ApJS*, **172**, 434
- Sargent, M. T., Bethermin, M., Daddi, E., & Elbaz, D. 2012, *ApJL*, **747**, L31
- Sargent, M. T., Daddi, E., Bethermin, M., et al. 2014, *ApJ*, **793**, 19
- Sargent, M. T., Schinnerer, E., Bethermin, M., et al. 2010, *ApJL*, **714**, L190
- Scarlata, C., Carollo, C. M., Lilly, S., et al. 2007, *ApJS*, **172**, 406
- Schaefer, A. L., Croom, S. M., Scott, N., et al. 2019, *MNRAS*, **483**, 2851
- Schawinski, K., Koss, M., Berney, S., & Sartori, L. F. 2015, *MNRAS*, **451**, 2517
- Schechter, P. 1976, *ApJ*, **203**, 297
- Schinnerer, E., Carilli, C. L., Scoville, N. Z., et al. 2004, *AJ*, **128**, 1974
- Schinnerer, E., Sargent, M. T., Bondi, M., et al. 2010, *ApJS*, **188**, 384
- Schinnerer, E., Smolčić, V., Carilli, C. L., et al. 2007, *ApJS*, **172**, 46
- Schreiber, C., Elbaz, D., Pannella, M., et al. 2015, *A&A*, **575**, A74
- Schreiber, C., Elbaz, D., Pannella, M., et al. 2016, *A&A*, **589**, A35
- Schreiber, C., Pannella, M., Leiton, R., et al. 2017, *A&A*, **599**, A134
- Scoville, N., Abraham, R. G., Aussel, H., et al. 2007, *ApJS*, **172**, 38
- Scoville, N., Arnouts, S., Aussel, H., et al. 2013, *ApJS*, **206**, 3
- Seymour, N., Huynh, M., Dwelly, T., et al. 2009, *MNRAS*, **398**, 1573
- Shivaei, I., Reddy, N. A., Shapley, A. E., et al. 2015, *ApJ*, **815**, 98
- Siudek, M., Malek, K., Scodreggio, M., et al. 2017, *A&A*, **597**, A107
- Smolčić, V. 2009, *ApJL*, **699**, L43
- Smolčić, V., Delvecchio, E., Zamorani, G., et al. 2017a, *A&A*, **602**, A1
- Smolčić, V., Novak, M., Bondi, M., et al. 2017b, *A&A*, **602**, A2
- Sobral, D., Best, P. N., Smail, I., et al. 2014, *MNRAS*, **437**, 3516
- Speagle, J. S., Steinhardt, C. L., Capak, P. L., & Silverman, J. D. 2014, *ApJS*, **214**, 15
- Steidel, C. C., Adelberger, K. L., Giavalisco, M., Dickinson, M., & Pettini, M. 1999, *ApJ*, **519**, 1
- Strateva, I., Invezic, Z., Knapp, G. R., et al. 2001, *AJ*, **122**, 1861
- Su, K.-Y., Hopkins, P. F., Hayward, C. C., et al. 2018, arXiv:1809.09120
- Tabatabaei, F. S., Schinnerer, E., Krause, M., et al. 2017, *ApJ*, **836**, 185
- Tasca, L. A. M., Le Fevre, O., Hathi, N. P., et al. 2015, *A&A*, **581**, A54
- Taylor, M. B. 2005, in ASP Conf. Ser. 347, *Astronomical Data Analysis Software and Systems XIV*, ed. P. Shopbell, M. Britton, & R. Ebert (San Francisco, CA: ASP), 29
- Thanjavur, K., Simard, L., Bluck, A. F. L., & Mendel, T. 2016, *MNRAS*, **459**, 44
- Thomas, D., Maraston, C., Schawinski, K., Sarzi, M., & Silk, J. 2010, *MNRAS*, **404**, 1775
- Tinsley, B. M. 1968, *ApJ*, **151**, 547
- Tinsley, B. M., & Danly, L. 1980, *ApJ*, **242**, 435
- Tisanić, K., Smolčić, V., Delhaize, J., et al. 2018, arXiv:1812.03392
- Tomczak, A. R., Quadri, R. F., Tran, K.-V. H., et al. 2016, *ApJ*, **817**, 118
- Tomczak, A. R., Lemaux, B. C., Lubin, L. M., et al. 2019, *MNRAS*, **484**, 4695
- Torrey, P., Vogelsberger, M., Hernquist, L., et al. 2018, *MNRAS*, **477**, L16
- Tresse, L., & Maddox, S. J. 1998, *ApJ*, **495**, 691
- Tyler, K. D., Bai, L., & Rieke, G. H. 2014, *ApJ*, **794**, 31
- Tyler, K. D., Rieke, G. H., & Bai, L. 2013, *ApJ*, **773**, 86
- Upjohn, J. E., Brown, M. J. I., Hopkins, A. M., & Bonne, N. J. 2019, *PASA*, **36**, e012
- Van Der Walt, S., Colbert, S. C., & Varoquaux, G. 2011, *CSE*, **13**, 22
- van der Wel, A., Franx, M., van Dokkum, P. G., et al. 2014, *ApJ*, **788**, 28
- Vardoulaki, E., Jimenez Andrade, E. F., Karim, A., et al. 2019, arXiv:1901.10168
- Viero, M. P., Wang, L., Zemcov, M., et al. 2013, *ApJ*, **772**, 77
- Vito, F., Gilli, R., Vignali, C., et al. 2014, *MNRAS*, **445**, 3557
- von der Linden, A., Wild, V., Kauffmann, G., White, S. D. M., & Weinmann, S. 2010, *MNRAS*, **404**, 1231
- Whitaker, K. E., Labbe, I., van Dokkum, P. G., et al. 2015, *ApJL*, **811**, L12
- Whitaker, K. E., Pope, A., Cybulski, R., et al. 2011, *ApJ*, **735**, 86
- Whitaker, K. E., Pope, A., Cybulski, R., et al. 2017, *ApJ*, **850**, 208
- Whitaker, K. E., van Dokkum, P. G., Brammer, G., & Franx, M. 2012, *ApJL*, **754**, L29
- Whitaker, K. E., van Dokkum, P. G., Brammer, G., & Franx, M. 2014, *ApJ*, **795**, 104
- White, R. L., Helfand, D. J., Becker, R. H., Glikman, E., & de Vries, W. 2007, *ApJ*, **654**, 99
- Williams, W. L., Calistro Rivera, G., Best, P. N., et al. 2018, *MNRAS*, **475**, 3429
- Wong, O. I., Koss, M. J., Schawinski, K., et al. 2016, *MNRAS*, **460**, 1588
- Wuyts, S., Forster Schreiber, N. M., van der Wel, A., et al. 2011, *ApJ*, **742**, 96
- Yun, M. S., Reddy, N. A., & Condon, J. J. 2001, *ApJ*, **554**, 803
- Zwart, J. T. L., Jarvis, M. J., Deane, R. P., et al. 2014, *MNRAS*, **439**, 1459